Vilde Vinnes Jacobsen

Effect of Rh on Pd-based Three-Way Catalyst for Promotion of CH_4 Steam Reforming under O_2 Dithering Conditions

September 2021

Master's thesis

2021

Master's thesis

Vilde Vinnes Jacobsen

NTNU
Norwegian University of
Science and Technology

NTNU
Norwegian University of
Science and Technology

NTNU
Norwegian University of Science and Technology

Effect of Rh on Pd-based Three-Way Catalyst for Promotion of CH$_4$ Steam Reforming under O$_2$ Dithering Conditions

Vilde Vinnes Jacobsen

Preface

This master thesis is written in collaboration between the Applied Catalysis and Spectroscopy (ACS) group at Paul Scherrer Institute (PSI) and the Department of Chemical Engineering at the Norwegian University of Science and Technology (NTNU) in relation to the final semester of Chemical Engineering and Biotechnology at NTNU.

Villigen, Switzerland
September 30, 2021

Vilde Vinnes Jacobsen

Abstract

In the past years, interest in natural gas (NG) as an alternative fuel has grown as its combustion leads to lower CO_2 and particulate matter emissions compared to the traditional fuels. Combustion of NG, however, leads to unburnt CH_4 which is a severe greenhouse gas. Catalytic abatement technologies, such as a three-way catalyst (TWC), are therefore necessary to simultaneously abate unburnt CH_4, NO and CO after the NG engine. Over the years, direct CH_4 oxidation by O_2 has been extensively studied over Pd where it is promoted over PdO or mixed Pd-PdO species. However, NO reduction mainly occurs over reduced Pd and it is therefore hard to obtain full conversion of both reactions. Recently, CH_4 steam reforming reaction (CH_4-SR) has gained a lot of attention as it likely occurs over metallic Pd species, allowing both reactions to occur simultaneously which has shown to induce high pollutant removal. Nevertheless, CH_4-SR has been proven as difficult to trigger under static stoichiometric conditions especially at low temperatures. However, major enhancements in activity have been reported under dynamic O_2 dithering conditions where the O_2 dosage in the feed is periodically varied around stoichiometric conditions at a certain amplitude. This makes it possible to modify the state of the active metals, and therefore tune the reaction schemes taking place (i.e. CH_4 oxidation by O_2, CH_4-SR).

In this master thesis Rh and bimetallic Pd-Rh on alumina (Al_2O_3) and ceria-zirconia (CZ) were studied with the aim to promote CH_4-SR reaction as Rh and CZ have demonstrated to be very efficient towards the reaction. A benchmark catalyst, Pd/Al_2O_3, was also synthesized. The CZ support was synthesized through the coprecipitaion method, while the active metals were deposited on the supports (Al_2O_3 or CZ) by the incipient wetness method. The catalysts were characterized by X-ray diffraction (XRD), N_2-physisorption, transmission electron microscopy (TEM), oxygen storage capacity (OSC), temperature programmed reduction (TPR), CO-diffuse reflectance infrared fourier transform spectroscopy (CO-DRIFT), X-ray absorption (XAS) and inductively coupled plasma optical emission spectrometry (ICP-OES). The catalytic activity was evaluated by performing temperature ramps under stoichiometric conditions after either an oxidation or reduction pretreatment. It was further investigated through lambda sweeps where the O_2 concentration in the feed was decreased in a step-wise manner. Finally, tests were carried out in order to deter-

mine the optimal O_2 dithering condition for each catalyst and the best conditions were applied in temperature ramp experiments.

Under stoichiometric conditions a negative hysteresis was found over Pd/Al_2O_3 whereas a positive hysteresis was observed over the bimetallic Pd-Rh. Through in situ XRD it was found that Rh promoted the redox properties of Pd, as Pd in $Pd-Rh/Al_2O_3$ oxidized and reduced more easily than Pd only. Further investigation by ex situ XAS showed that high pollutants abatement rates (high NO reduction and CH_4-SR) on Pd-based catalysts were a result of the metallic oxidation state of Pd, which in the presence of Rh, was maintained up to lower temperatures leading to the positive hysteresis. However, Pd/Al_2O_3 appeared to be the most active catalyst towards CH_4-SR under these conditions, but led to a significant formation of undesired NH_3, due to the reduction of NO by H_2. Though CH_4-SR was triggered at higher temperature over the Rh-based catalysts, the NH_3 formation was drastically decreased.

Through lambda sweeps, it was found that the activity was enhanced when working with less O_2 in the feed (rich conditions), implying that the metals were in their reduced state. Hence, stoichiometric temperature ramps were conducted after a reduction pretreatment to ensure that the metals were reduced prior to the reaction. This resulted in higher conversion over all the alumina-based samples. This improvement, however, was not observed over the CZ-based samples likely due to O_2 back spillover from CZ to the metals, preventing their reduction.

Under dynamic conditions, activity of all catalysts were improved, especially when Rh was present. These working conditions promoted the reduction of Rh, which is highly active for CH_4-SR and NO reduction reactions. The activity appeared to be further enhanced when supported on CZ, which through lambda sweeps, was also found highly active for CH_4-SR under rich conditions likely due to reduced CZ activating the water during CH_4-SR. Rh supported by CZ under dynamic conditions resulted in CH_4-SR and full NO conversion already at 300 °C.

Conclusively, dynamic conditions showed great potential for after treatment of the exhaust gas of NG fueled vehicles, especially on Rh based catalysts.

Sammendrag

I løpet av de siste årene har interessen for naturgass (NG, *sim* 80 % CH_4) som et alternativt drivstoff økt da dens forbrenning fører til lavere CO_2- og partikkelutslipp sammenlignet med de tradisjonelle drivstoffene. Ettersom CH_4 er en alvorlig klimagass, må katalytisk teknologi som en treveis-katalysator (TWC) plasseres etter forbrenningskammeret for å redusere utslipp av ubrent CH_4, NO og CO. I det siste har direkte oksidasjon av CH_4 med O_2 blitt forsket på over en Pd basert katalysator hvor reaksjonen fremmes over oksidert Pd. Reduksjon av NO skjer hovedsakelig over redusert Pd, og det er derfor vanskelig å oppnå full konversjon av begge reaktantene. Nylig har CH_4 dampreformering (CH_4-SR) fått mye oppmerksomhet ettersom den også forekommer over redusert Pd, slik at begge reaksjonene kan forekomme samtidig, noe som har vist å forårsake høy omgjøring. Men CH_4-SR er vanskelig å utløse under statiske støkiometriske forhold, spesielt ved lave temperaturer. Likevel har forbedringer blitt observert under dynamiske «O_2-dithering» forhold der O_2 i reaksjonsmiksen blir periodisk variert rundt støkiometriske forhold ved en viss amplitude. Dette gjør det mulig å justere oksidasjonstilstanden til de aktive metallene, og slik regulere reaksjonene som finner sted over katalysatoren (dvs. CH_4-oksidasjon ved O_2, CH_4-SR). CH_4

I denne masteroppgaven ble Rh og bimetallisk Pd-Rh på aluminumoksid (Al_2O_3) og ceria-zirconia (CZ) studert med sikte på å fremme CH_4-SR ettersom Rh og CZ har vist seg å være svært effektive mot CH_4-SR. En referansekatalysator, Pd/Al_2O_3, ble også syntetisert. CZ-bæreren ble syntetisert via samutfellingsmetoden, mens de aktive metallene ble avsatt på bærerne (Al_2O_3 eller CZ) via tørr impregnering. Katalysatorene ble karakterisert ved hjelp av røntgendiffraksjon (XRD), N2-fysisorpsjon, transmisjonselektronmikroskopi (TEM), oksygen lagrings kapasitet (OSC), temperaturprogrammert reduksjon (TPR), CO diffus refleksjon infrarød fouriertransformasjonspektroskopi (CO-DRIFT), røntgen-absorpsjonsspektroskopi (XAS) og induktivt koblet plasma optisk emisjonsspektrometri (ICP-OES). Den katalytiske aktiviteten ble evaluert ved å utføre temperaturramper under støkiometriske betingelser etter en oksidert eller redusert forbehandling, og ble videre undersøkt via «lambda sweeps» hvor O_2-konsentrasjonen i reaksjonsmiksen senkes på en trinnvis måte. Til slutt ble det utført eksperimenter for å bestemme de optimale O_2-dithering betingelsene

for hver katalysator hvor de beste betingelsene ble undersøkt via temperaturrampeeksperimenter.

Under støkiometriske forhold ble en negativ hysterese funnet over Pd/Al_2O_3 mens en positiv hysterese ble observert over bimetallisk Pd-Rh. Gjennom in situ XRD ble det funnet at Rh fremmer redoksegenskapene til Pd, ettersom Pd i $Pd-Rh/Al_2O_3$ oksiderte og reduserte enklere enn Pd. Ytterligere undersøkelser gjennom ex situ XAS viste at høy omgjøring av reaktantene (høy reduksjon av NO og CH_4-SR) på Pd-baserte katalysatorer var et resultat av redusert Pd, som i nærvær av Rh ble opprettholdt ved lavere temperaturer som fører til den positive hysteresen. Pd/Al_2O_3 viste seg å være den mest aktive katalysatoren for CH_4-SR under støkiometriske forhold, men førte til en betydelig dannelse av uønsket NH_3, på grunn av at NO ble redusert av H_2. Selv om CH_4-SR ble observert ved høyere temperatur over de Rh-baserte katalysatorene, var NH_3-formasjonen drastisk redusert.

Gjennom lambda sweeps ble det funnet at aktiviteten ble forbedret når man jobbet med mindre O_2 i reaksjonsmiksen (rik blanding), noe som antyder at metallene var i redusert tilstand. På grunn av dette ble støkiometriske temperaturramper utført etter redusert forbehandling for å sikre at metallene ble redusert før eksperimentet. Dette resulterte i høyere aktivitet over alle de alumina-baserte katalysatorene. Denne forbedringen ble imidlertid ikke observert over de CZ-baserte katalysatorene sannsynligvis på grunn av O_2 ble overført fra CZ til metallene, som forhindret redusert tilstand.

Under dynamiske forhold ble aktiviteten forbedret for alle katalysatorene, spesielt når Rh var tilstede. Et slikt forhold fremmet redusert Rh, som er svært aktiv for CH_4-SR og reduksjon av NO. Aktiviteten syntes å bli ytterligere forsterket når CZ var brukt som bærer, som gjennom lambda sweeps også ble funnet svært aktiv for CH_4-SR under rike forhold sannsynligvis på grunn av redusert CZ aktiverer H_2O for CH_4-SR. Rh på CZ under dynamiske forhold resulterte i CH_4-SR og full reduksjon av NO allerede ved 300 °C.

Konkluderende viste dynamiske forhold et stort potensial for etterbehandling av eksosgassen til NG kjøretøy, spesielt over Rh-baserte katalysatorer.

Contents

List of Abbreviations

Abbreviation	Description
BET	Brunauer-Emmet-Teller
BJH	Barrett-Joyner-Halenda
BTU	British Thermal Unit
CZ	ceria-zirconia
DOSC	Dynamic Oxygen Storage Capacity
DRIFT	Diffuse Reflectance Infrared Fourier Transform Spectroscopy
EDX	Electron Dispersive X-Ray Microanalysis
EI	Electron Ionization
ESI	Electrospray Ionization
EXAFS	Extended X-Ray Absorption Fine Structure
FT	Fourier Transform
FTIR	Fourier Transform Infrared Spectroscopy
HAADF	High-Angle Annular Dark Field
ICP-OES	Inductively Coupled Plasma Optical Emission Spectrometry
IR	Infrared
IWI	Incipient Wetness Imgregnation
MALDI	Matrix-Assisted Laser Desorption/Ionization
MOC	Methane Oxidation Catalyst
MS	Mass Spectrometry
NG	Natural Gas
NGV	Natural Gas Vehicles
OECD	Organisation for Economic Co-operation and Development
OSC	Oxygen Storage Capacity
OSCC	Oxygen Storage Capacity Complete
PGM	Platinum Group Metals
PM	Particle Matter
ppm	Parts Per Million
SA	Surface Area
SCR	Selective Catalytic Reduction
SEM	Scanning Electron Microscopy

SR	Steam Reforming
SSA	Specific Surface Area
STEM	Scanning Transmission Electron Microscopy
TEM	Transmission Electron Microscopy
TPR	Temperature Programmed Reduction
TWC	Three-Way Catalyst
WGS	Water-gas-shift
XANES	X-Ray Absorption Near Edge Structure
XAS	X-Ray Absorption
XRD	X-Ray Diffraction

List of Symbols

Symbol	Description	Unit
□	Empty oxygen vacancy	-
β	Peak width at half width	Rad
λ	Air-fuel ratio	-
λ	Wavelength	cm^{-1}
$\mu(E)$	Absorption coefficient	-
θ	Angle between the incoming X-ray and the normal	°
C	BET constant	
d	Distance between to lattice planes	Å
d	Thickness of the material	nm
E	Voltage	$Kgm^2A^{-1}s^{-3}$
E_0	Standard voltage	$Kgm^2A^{-1}s^{-3}$
E_0	Energy of the treshold	eV
E_b	Binding energy of an electron	eV
E_K	Kinetic energy of a photoelectron	eV
F	Faraday's constant	$Cmol^{-1}$
$F_{i,in}$	Flow rate of i	$mols^{-1}$
F_{tot}	Total flow ratet	$mols^{-1}$
(g)	Gas phase	-
hv	Energy of incident X-ray	eV
I_x	Intensity of X-ray through a material	a.u
I_0	Intensity of the incident X-ray	a.u
K	Constant in the Scherrer equation	-
K_i	Constant	-
L	Crystallite diameter	nm
MS_i	MS signal of i	a.u
m_i	Mass of i	Kg
n	Order of diffractation	-
n	Number of electrons tranferred	-
P_i	Partial pressure of i	Bar
$P0$	Equlibrium pressure of the condensed gas	Bar

R	Ideal gas constant	$\mathrm{JK^{-1}mol^{-1}}$
(s)	Solid phase	-
T	Temperature	K
V	Volume adsorbed	$\mathrm{cm^3}$
Vm	Volume adsorbed at monolayer	$\mathrm{cm^3}$
$wt\%Pd$	Weigth percent of Pd	%
$WHSV$	Weight hourly space velocity	$\mathrm{h^{-1}g_{cat}^{-1}}$
X_i	Conversion of i	%
y_i	Molecular fraction of i	-

List of Figures

List of Tables

Chapter 1

Introduction

1.1   Global Challenges

One of today's major concerns within environment and health is air pollution which plays a critical role in climate change [1]. In 1992, increasing international concern about climate change led to the creation of the United Nations Framework Convention on Climate Change (UNFCCC) [2]. Their main goal was to stabilize and reduce greenhouse gas concentrations in the atmosphere. In the last 30 years, they have worked and put in place important agreements between countries such as the Kyoto Protocol and the Paris Agreement which annual assesses the progress against climate change [3]. Climate change issues have become more critical through the years, due, among others, to the increase of carbon dioxide concentrations in the atmosphere, which acts as a greenhouse gas, and thus contributes to the increase of temperatures globally [4]. Today, one of the main contributors to greenhouse gas emissions and air pollution is the transport sector due to the combustion of fossil fuels such as oil [5][6]. As a consequence, the automobile manufacturers are under pressure to move away from traditional fuels, which combustion leads to hazardous exhaust gas and particulate matter emissions, and seek for greener alternatives.

1.2   Natural Gas as Fuel

Natural gas (NG) is a combustive mix of hydrocarbons, consisting of 70-90 % of methane with a variable content of other hydrocarbons such as ethane, propane and butane and other gases [7]. Even though it is considered a fossil fuel, NG is one of the cleanest and most effective of the traditional fuels [6], due to its low sulfur content and reduced emission of NO_x and particle matter (PM) [8]. As methane has the highest hydrogen to carbon ratio of the hydrocarbons (4:1), it also releases less CO_2 compared to the traditional gasoline and diesel fuels [9][10]. A study conducted by the Organisation for Economic Co-operation and Development (OECD) states that the use of natural gas engines emits 30 % less CO_2 per British thermal unit (BTU) than oil based fuel and

1

reduces the PM emissions by 90 % [11]. A possible way to further reduce the environmental impact of the transportation sector would be to use biomethane as the fuel, as it is formed from a renewable origin [10]. Biomethane is an upgraded form of biogas which can be produced anaerobically by the digestion of organic substances such as dead animals, sewage and plant matter.

However, though NG vehicles (NGV) result in lower hazardous emissions, unburnt CH_4, CO and NO_x can still be found in the exhaust of NG combustion engines, and therefore require the need of efficient catalytic post-combustion system to convert them to harmless compounds (i.e. CO2, N2). This is especially important as CH_4 is a powerful greenhouse gas which has a global warming potential 70 times larger than CO_2 when looking at a 20 year time period [12].

Both lean and stoichiometric combustion systems can be used for natural gas vehicles (NGV) depending on the size and purpose of the vehicle [13][14]. Lean-burn NG engines have higher engine efficiency in comparison to stoichiometric engines but complex after-treatment systems, usually composed of a methane oxidation catalyst (MOC) followed by a urea injection system and a selective catalytic reduction (SCR) catalyst. On the other hand, stoichiometric NG engines only require a three-way catalyst (TWC), which simultaneously abate unburnt hydrocarbons, CO, and NO_x.

1.3 Three-Way Catalyst for Natural Gas

The Three-Way Catalyst (TWC) has been used for vehicle emission control since 1981 [15]. It is a catalyst placed downstream from a gasoline/NG engine to control the harmful emissions by reducing NO_x and oxidizing CO and hydrocarbons into harmless components such as N_2, CO_2 and H_2O as illustrated in Figure 1.1 [16].
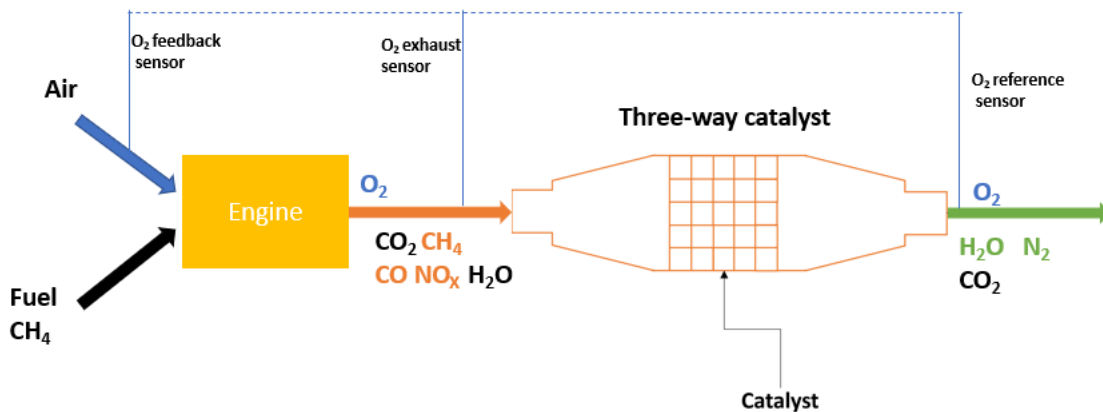
Figure 1.1: The TWC placed downstream from the NG engine to convert the hazardous emissions.

Today, the modern commercial TWC usually consists of a bimetallic Pd/Rh system which also

incorporates Al_2O_3, $Ce_xZr_{1-x}O_2$ and other oxide materials [17] distributed on a honeycomb ceramic monolith [18]. As the exhaust originates from a stoichiometric engine, an O_2 sensor is placed in the exhaust right before the catalyst and a second one placed after the catalyst in air as a reference [18]. A voltage, E, is generated across the sensors which is dependent on the O_2 concentration and represented by Nernst equation (Equation 1.1).

$$E = E_0 + RT/nF \cdot ln(P_{O_2})_{reference}/ln(P_{O_2})_{exhaust} \tag{1.1}$$

where E_0 is the standard state voltage, R is the ideal gas constant, T is temperature, n is the number of electrons transferred, F is Faraday's constant and P_{O_2} is the partial pressure of O_2. The generated signal of the voltage is fed back to the O_2 sensor infront of the engine to adjust the air-to-fuel ratio.

As an aftertreatment for a NG engine, the main hydrocarbon present in the exhaust gas is methane (over 90 vol%), which is harder to oxidize than the conventional hydrocarbons used in gasoline due, among others, to strong C-H bonds, molecular symmetry, weak adsorption strength [19]. The optimal catalyst composition and working conditions are therefore different than a TWC for gasoline engines.

Over the TWC, CH_4 abatement through direct oxidation of CH_4 by O_2 has been widely studied [20][21][22]. However, recently an additional reaction pathway of CH_4 steam reforming (SR) has gained a lot of attention [8][23][24][25]. The importance of CH_4-SR over the TWC has been demonstrated to be significant in order to achieve full pollutant removal, as it has been reported that NO reduction is greatly correlated to CH_4 conversion under rich conditions [26][24]. High maximum NO reduction has been detected due to the production of H_2 from CH_4-SR, creating a net reducing atmosphere, which is valuable for a maximum NO reduction [27].

1.3.1 Reaction Pool

The main reactions taking place over the TWC are the oxidation of CH_4 (Reaction 1.2), the oxidation of CO (Reaction 1.3) and the reduction of NO to N_2 (Reaction 1.4) [19].

$$CH_4 + 2O_2 \longrightarrow CO_2 + 2H_2O \tag{1.2}$$

$$CO + \frac{1}{2}O_2 \longrightarrow CO_2 \tag{1.3}$$

$$2NO \longrightarrow N_2 + O_2 \tag{1.4}$$
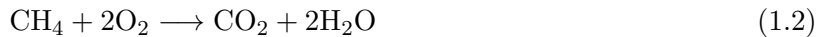
In oxidizing conditions and low temperatures there is also a possibility of the formation of N_2O as an intermediate product by Reaction 1.5 [28][29][30].

$$2NO \longrightarrow N_2O + \frac{1}{2}O_2 \tag{1.5}$$

3

However, several studies have reported a production of H_2 over the TWC for NG when no H_2 has been present in the simulated exhaust [8][31]. The production of H_2 can therefore be explained by steam reforming (SR) of methane and the water-gas shift (WGS) reaction which are described in Reaction 1.6 and 1.7 .

$$CH_4 + H_2O \longrightarrow CO + 3H_2 \tag{1.6}$$

$$CO + H_2O \longrightarrow CO_2 + H_2 \tag{1.7}$$

The H_2 production from the CH_4 SR and WGS has proven to play an important role in the TWC as it can act as a reducing agent for NO by Reaction 1.10 [8]. However, it also results in the production of the unwanted by-product NH_3 (Reaction 1.8 and 1.9) [8][26].

$$2NO + 5H_2 \longrightarrow NH_3 + H_2O \tag{1.8}$$

$$NO + 2CO + \frac{1}{2}H_2 + H_2O \longrightarrow NH_3 + 2CO_2 \tag{1.9}$$

$$2NO + 2H_2 \longrightarrow N_2 + 2H_2O \tag{1.10}$$
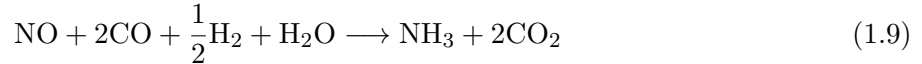
1.3.2   Operating Window

For gasoline applications, TWC operate at a stoichiometric air-to-fuel ratio ($\lambda = 1$) in order to remove CO, NO and the hydrocarbons simultaneously [32]. This was observed to be the point where the conversion of the three pollutants is the highest and it is defined as the CO-NO crossover point [33]. However, due to the low reactivity of CH_4, the CO-NO crossover point was observed to be shifted away from stoichiometry and towards rich conditions (excess fuel) [27][26][33]. This was demonstrated by Ferri et al. who performed activity tests over a commercial TWC when varying the O_2 dosage from lean to rich with simulated exhaust gas from both NG and gasoline engines [27]. They observed the CO-NO crossover point at $\lambda = 0.61$ for the NG simulation compared to $\lambda = 1$ for the gasoline.

Under the real operating conditions, though the catalyst is operated near stoichiometry, the actual applied air-to-fuel ratio oscillates around an average value [34]. Several studies have shown that varying the O_2 dosage at different amplitudes and frequencies around an average value has had a positive effect on the conversion of CH_4 compared to a static O_2 feed [27][8][26][35]. Bouncheda et al. studied the effect of periodic lean/rich operations around stoichiometry over a ceria-zirconia (CZ) promoted Pd-Rh/Alumina catalyst [8]. They observed that an amplitude of 0.02 ($\lambda = 1 \pm 0.02$) gave a higher and more stable conversion of CH_4 than static operation at $\lambda = 1$ most likely due to a more active Pd^0/PdO state.

1.3.3   Active Metals

1.3.3.1   Palladium

Currently, commercial TWCs use Platinum Group Metals (PGMs; mainly palladium, platinum, and rhodium) as their active phase, where palladium (Pd) is most efficient for total oxidation of methane and has also an impressive oxidation ability towards CO [36][37][38][39][19]. Since CH_4 is the most challenging pollutant to remove from NGV exhaust gas, palladium is always present in higher quantities compared to the other PGMs [40][41].

However, the performance of the palladium is influenced by the interaction with the support, particle size and the precursor utilized in the preparation of the catalyst [42]. Lin et al. reported that Pd supported on CZ prepared by $Pd(NO_3)_2$ as precursor exhibited a better catalytic activity for CO and HC oxidation, smaller Pd_n clusters and a stronger metal-support interaction than the catalysts prepared with $Pd(NH_3)_4(NO_3)_2$ or H_2PdCl_4 [43]. This was also reported by Roth et al. who studied the catalytic behaviour of Pd supported on alumina for methane oxidation [44]. They concluded that the use of $Pd(NO_3)_2$ as a precursor resulted in better activity and dispersion than the utilization of H_2PdCl_4.

Furthermore, the catalytic activity of Pd is also dependent on its oxidation state [45]. Several studies have reported that metallic Pd, oxidized PdO, and mixed Pd^0/PdO (PdO_x) species are active for CH_4 oxidation [46] [47][48]. However, it is clear that not all Pd species induce the same chemistry and hold similar efficiency. Franken and al. have proposed an optimal working window of reduced Pd content for wet lean CH_4 oxidation that was placed between 25 and 65 %, while a Pd0 content between 65 and 75 % was reported to inhibit CH_4 oxidation [20]. Additionally, Chin. et al. have found that the lowest activation energy necessary for the C-H cleavage is over PdO_x species, evidencing that PdO_x species are the most active for direct CH_4 oxidation by O_2 though the catalytic efficiency can vary depending on the Pd/PdO ratio [49]. As for promoting CH_4-SR, Salun et al. concluded that the presence of metallic Pd^0 in PdO_x form is essential [23]. This was also confirmed by Bounechada et al, however this was achieved at higher temperatures [8].

1.3.3.2   Rhodium

Rh is widely used in the TWC due to its ability to reduce NO [50][51][52]. Compared to Pd, Rh has better resistance against sintering and helps to suppress NH_3 formation in rich conditions and enhancing the selectivity towards N_2 [53][51][54][55]. However, at low temperatures and in a net oxidizing atmosphere, it is reported to promote the formation of N_2O as an intermediate [29][28]. NH_3, being poisonous and corrosive, and N_2O, a greenhouse gas 300 times greater than CO_2, are both undesirable secondary products from the reduction of NO that need to be taken into consideration [31]. Furthermore, Rh is also recognized as an active metal for CH_4-SR which is an useful ability in the aftertreatment of a NG engine [56][53][57]. As Rh is remarkably more

expensive than the other metals [51], it is usually incorporated with Pd or Pt in smaller amounts to improve the thermal stability and the reduction properties of the catalyst [58][28][59][60]. The ratio of the incorporation of Rh to the other metals however, may influence the performance of the catalyst. Vedyagin et al., who studied different metal ratios of Pd-Rh supported on alumina and its effect on the activity in TWC, suggested that the optimum ratio of the Pd-Rh catalyst was 3:2 due to a strong Pd-Rh interaction [61]. The same group also suggested this ratio to possess high-temperature stability during CO oxidation [62].

Unlike Pd, Rh is mostly active while in the reduced metallic state of Rh^0 [63][17] [64]. The oxidized states of Rh however, Rh_2O_3 and RhO_2, is considered less active [65][66], and was reported to interact with the support when it is in its oxidized form, making it unavailable for catalytic reactions, which is especially discussed considering alumina in several studies [67][63][68][69][64].

1.3.4 Active Support

1.3.4.1 Alumina

Alumina is the most used support in catalysis due to its thermal and mechanical stability [70]. It exists in different structures giving alumina a wide range off applications. One of these structures is γ-Alumina (γ-Al_2O_3), which is usually the main material of the TWC due to its high specific surface area (SSA) (50 - 300 m^2g^{-1}) [19][70]. Increasing the SSA is the main purpose of the support in order to disperse the active noble metals and enhance the catalytic activity [71]. γ-Alumina also offers mesopores between 5 and 15 nm, a pore volume of approximately 0.6 cm^3g^{-1} and high thermal stability preventing the noble metals from sintering [70]. However, at very high temperatures (> 1 000 C), which is a possibility during TWC operation, γ-alumina can transform to α-alumina which has a considerably lower SSA of 10 m^2g^{-1} [71].

1.3.4.2 Ceria

Ceria (CeO_2) is usually added to the TWC due to its ability to store, release and exchange oxygen by changing the oxidation state between Ce^{4+} and Ce^{3+} [72][57][73]. As mentioned the optimum conversion over the TWC is found at a certain operating window. However, in real driving conditions the exhaust gas may vary drastically away from this window. In order to maintain the optimal conversion ceria makes it possible to store oxygen under lean conditions and release oxygen under rich conditions as illustrated in Figure 1.2 [16]. This has proven to enhance the activity over the TWC immensely [72], as well as promoting CH_4-SR [57][74]. Ceria can be used in the TWC either as dopant or as a support [74][75][76]. However, ceria possesses poor hydrothermal stability, but it can be improved by introducing zirconia (Zr^{4+}) into the ceria lattice [77][78]. Furthermore, several studies have reported that another advantage of adding Zirconia into the Ceria lattice is that it considerably improves the oxygen storage capacity (OSC) compared to CeO_2 [79][80][81]. According to Baducci et al.the incorporation of Zr into the ceria lattice will lower the energy for

the reduction of Ce^{4+} [82]. As a result bulk oxygen will diffuse more easily to the surface and promote the ceria redox properties. Nevertheless, studies have reported that different Ce/Zr ratios can affect the ceria redox properties. Silva et al. analyzed the effect of the Ce/Zr ratios for partial methane oxidation over $Pt/Ce_xZr_{x-1}O_2/Al_2O_3$ (x = 0.25, 0.5, 0.75) catalysts and reported that $Pt/Ce_0 \cdot 5\,Zr_{0.5}O_2/Al_2O_3$ had the highest activity and stability [73]. This was also confirmed by Noronha et al. who found $Pt/Ce_0 \cdot 5\,Zr_{0.5}O_2$ to give the highest OSC and activity when performing CO_2 reforming of methane [83].Not only the Ce/Zr ratio, but also the preparation method might determine the properties of CZ [79]. In the literature various preparation methods with various results have been reported such as coprecipitation [84][85], hydrothermal methods [86][87] and sol-gel methods [88][89]. Li et al. prepared CZ by different coprecipitaion methods, such as coprecipitation, complexing-coprecipitation and complexing-coprecipitation-solution [90]. Their results concluded that complexing-coprecipitation method produced a thermally stable CZ with high SSA and OSC.
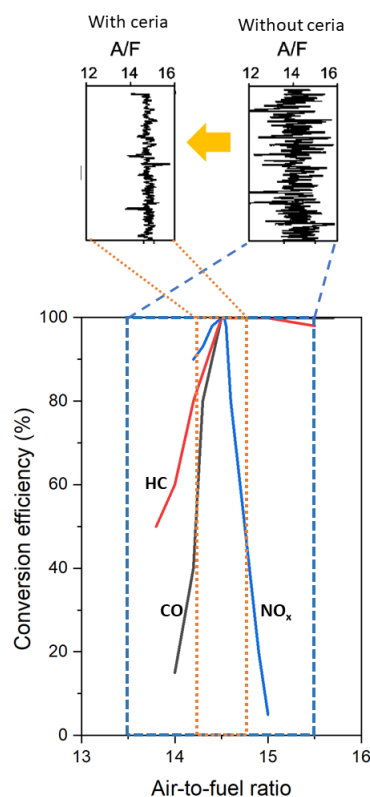
Figure 1.2: The operating window is narrowed down when the catalyst contains ceria. Adepted from [91].

1.4 Aim of the Project

The aim of this project is to verify that CH_4-SR is responsible for the improved activity over Pd and to further promote the reaction by studying the effect of Rh addition to Pd (both structure and activity) and Rh alone. For this purpose Rh and bimetallic Pd-Rh on alumina will be synthesized

by incipient wetness impregnation, where a synthesized Pd/Alumina catalyst is used as benchmark. Furthermore, a ceria-zirconia (CZ) support will be synthesized by coprecipitation, with Rh and Rh-Pd as active metals, as CZ can contribute to the CH_4-SR reaction due to its oxygen storage capacity. The five catalysts are characterized in order to obtain useful information about their structural properties. The catalyst activity will be investigated under simulated NG engine exhaust conditions while applying both static and dynamic (O_2 dithering) operations. The goal is to compare these catalysts to be able to understand the influence of Rh on the observed chemistry as well as to optimize the pulsing conditions (i.e. amplitude and frequency) of the O_2 dithering for each catalyst in order to obtain high pollutant conversions.

Chapter 2

Theory

2.1 Catalyst Synthesis

2.1.1 Incipient Wetness Impregnation

Incipient wetness impregnation (IWI) is one of the most common methods for heterogeneous catalyst preparation [92]. The metal precursor is typically dissolved in an organic or aqueous solution [93] which volume corresponds to 80 % of the total pore volume of the support. The solution is then deposited on the dried support (to ensure full water desorption) [94]. By capillary forces, the solution is drawn into the pores of the support as illustrated in Figure 2.1. If impregnation is executed correctly, no excess solution will be deposited outside the pores, which is why the method is also named dry impregnation.
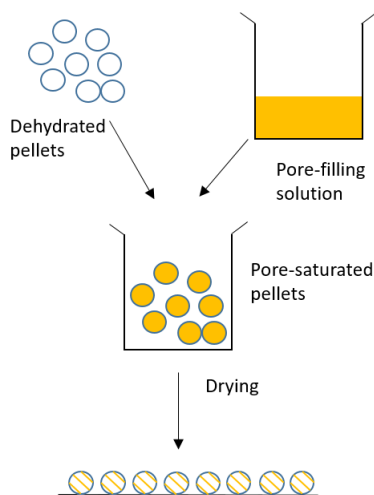
Figure 2.1: A schematic overview of the steps during the incipient wetness impregnation. Adapted from [95]

The impregnated support is then dried in order for the metal precursors particles to deposit and settle in the pores by evaporation of water [94][95]. The drying rate, however, does affect the distribution of the active metal in the pores. The goal is to obtain an uniform distribution and concentration of the metal particles as illustrated in Figure 2.2b. A too slow drying rate will lead to the precursor being deposited at the end of the pore in the center as a so-called egg yolk (Figure 2.2a), whereas a too fast drying will force the precursor to deposit at the entrance of the pores leading to an eggshell deposit (Figure 2.2c). The final stage of the impregnation is the calcination of the catalyst in air at high temperatures The purpose of this high temperature treatment in an oxidising environment is to dispose and volatilize the salts (i.e. chloride, nitrates) bounded to the metal [95]. In this way the crystallized precursors are converted into the metal oxide or metal.
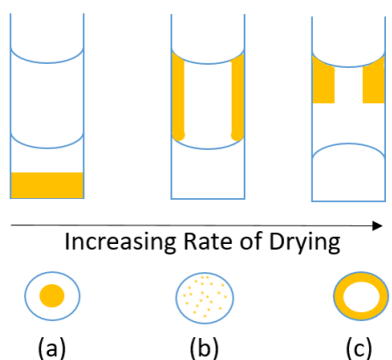
Figure 2.2: The profiles of the pores and particles during the drying rate. Adapted from [95]

2.1.2   Co-precipitation

Co-precipitation is a convenient method for synthesizing oxide materials as it allows several metal precursors to be deposited in a single process [96][97]. Compared to IWI described previously, this method is highly dependent on reaction parameters (pH, temperature, stirring etc.) and requires more control as during this single process chemical phases, surface area, porous structure, particle size and dispersion are created [97][98]. The soluble metal precursors are usually dissolved in an aqueous solution. The solution is supersaturated through an increase of the pH-value by adding an precipitating agent such as ammonium hydroxide or sodium carbonate [90][97]. The two next stages during the synthesis are be the nucleation which occurs at critical supersaturation and followed by crystal growth [97]. In order to obtain a homogeneous precipitation and monodispersed particles a separation of these two stages would be ideal, however they usually progress simultaneously [98][97]. The result of the precipitation is a homogeneous mixture of hydroxides which is filtered off usually through vacuum [70]. The final steps of the co-precipitation is drying and calcination at appropriate temperatures, in order to remove water and any compounds remaining from the precursors (i.e. salts), which yields a porous catalyst.

2.2 Characterization

2.2.1 X-ray Diffraction

X-ray Diffraction (XRD) is a method widely used to identify crystalline solid phases, phase transformations, lattice constants and the mean crystallite size of a crystalline solid [99]. Crystals are made of regular arrays of atoms, which are able to scatter incident X-rays from their interaction with the atom's electron cloud. If the wavelength of the scattered wave is the same as the incident one (X-ray photons did not lose any energy) and that only momentum has been transferred, the process is elastic and is called Thompson scattering. If, on the other hand, the wavelength of the scattered wave is different due to a transfer of energy, the process is inelastic and is called Compton scattering. Since X-rays can be considered as waves of electromagnetic radiation, the diffraction of X-rays by matter is due to the combination of two phenomena, the scattering of X-rays by the different electrons in the individual atoms, and the interference between the scattered outgoing waves from these atoms. The X-rays measured in diffraction experiments therefore carry information about the density and distribution of electrons in materials, hence one can deduce their structure based on the elastic scattering of X-rays. The interference patterns result from a larger ensemble of atoms, so that XRD is used to determine the internal structure of components with long-range order, i.e. crystalline materials. In these materials constructive interference occurs at specific scattering angles, giving rise to a characteristic pattern of XRD peaks. This is formulated in by the Bragg law equation:

$$n\lambda = 2dsin\theta \tag{2.1}$$

where λ is the wavelength, d the distance between two lattice planes, θ the angle between the incoming X-rays and the normal to the reflecting lattice planes and n the order of diffraction. By measuring the angles in which diffraction occurs, the corresponding lattice spacing can be found by Bragg's law which is characteristic for a specific compound.
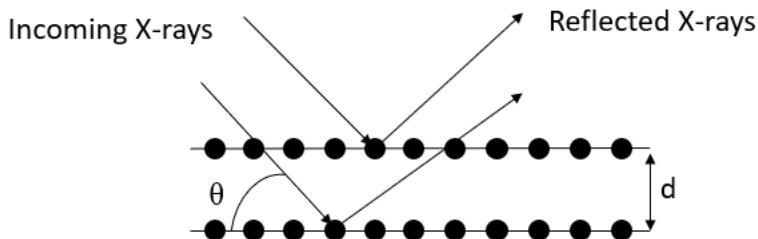
Figure 2.3: An illustration of the incoming X-rays being diffracted by the solid.

From the diffractogram it is possible to relate the line width of the peaks to the diameter of the crystal by the Scherrer formula [70]:

$$L = \frac{K\lambda}{\beta cos\theta} \tag{2.2}$$

where L is the crystallite diameter, K a constant dependent on the shape of the particle, λ the wavelength of the X-ray, β the peak of the width at half width and θ the angle between the incoming X-rays and the normal to the reflecting lattice planes. The peak width, β, can either be measured at its half peak (K is between 0.84 and 0.89 depending on the shape of the particle) or the integrated peak-area is divided by the peak height (K is between 1.0 and 1.16 depending on the shape) [99]. When measuring the crystallite size of a multicomponent system, such as a metal/support catalyst, various disturbances may occur. These disturbances are either due to overlap of the diffraction peaks of the metal and the support or the metal load might be too small to yield a diffraction peak that can be analyzed. The lower limit of the metal load depends on the atomic number of the metal as the intensity of the diffraction peak is proportional to the square root of the atomic number [99]. [100]

2.2.2   N$_2$-physisorption

To determine the internal surface area of a porous material, the N$_2$-physisorption method is widely used. Liquid Nitrogen at 77K is adsorbed into the porous material, where each adsorbed N$_2$-molecule occupies an area of 16.2 Å at this temperature. By measuring how many N$_2$-molecules adsorb at monolayer coverage on the material, one can determine the internal surface area [70]. Dividing this area by the mass of the sample gives the specific surface area (SSA) which is calculated by using the Brunauer-Emmett-Teller equation (BET equation) shown in Equation 2.3.

$$\frac{P}{V(P_0 - P)} = \frac{1}{V_m C} + \frac{(1 - C)}{V_m C}\frac{P}{P_0} \tag{2.3}$$

where P is the partial pressure of the inert gas, V the volume adsorbed at P, P_0 the equilibrium pressure of the condensed gas, V_m the volume adsorbed at monolayer and C the BET constant. The BET is only valid under certain assumptions such as dynamic equilibrium between adsorbate and adsorptive, densely packed layers and no interactions between the monolayer and each adsorption layer [70]. The adsorption of the gas is usually represented in an isotherm plot, which represents the amount of nitrogen adsorbed at 77K as a function of pressure [99]. The isotherms are classified into six different profiles depending on the interactions between the adsorbent and adsorbate. The different types of isotherms are shown in Figure 2.4. [101].
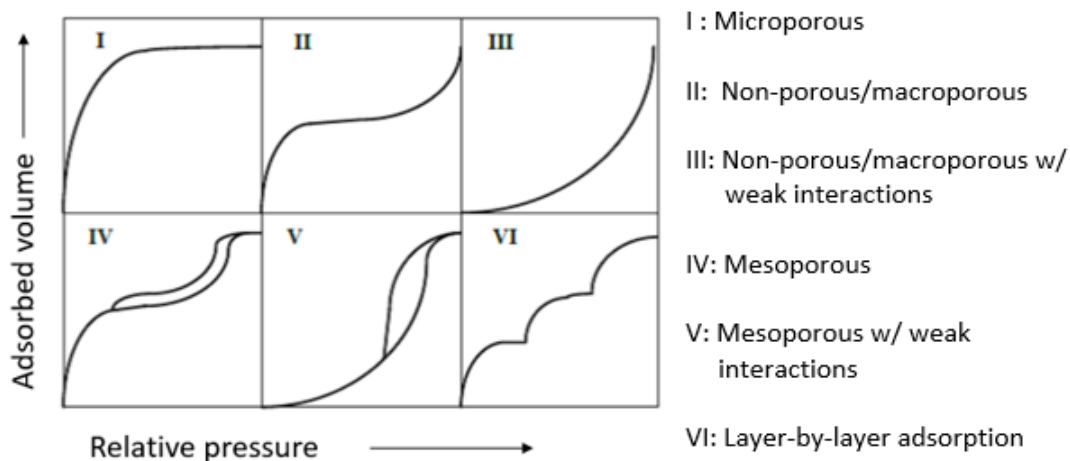
Figure 2.4: The different types of BET isotherms. Adapted from [101]

The hysteresis effect observed in isotherm type IV and V occurs as the desorption of N_2 must overcome capillary forces before evaporation of the gas. By applying the Barrett-Joyner-Halenda method (BJH), the hysteresis can provide information about the pore volume distribution of the sample [102].

2.2.3   Electron Microscopy

Electron microscopy is a technique to determine the structure of the sample by exposing it to a beam of electrons [103]. As electrons have characteristic wavelength of less than an Ångstrøm, it is possible to study the sample in atomic detail. Figure 2.5 illustrates the different types of signals that can be detected when a sample is exposed to a primary electron beam with energy between 100 and 400 keV.
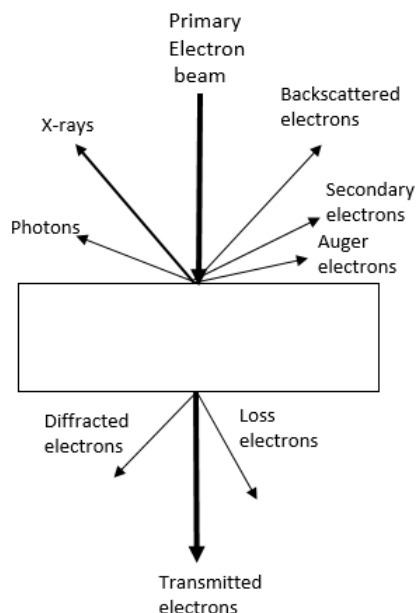
Figure 2.5: An incoming primary electron beam on a sample results in a number of detectable signals. Adapted from [70].

Transmission Electron Microscopy

In transmission electron microscopy (TEM), a primary beam of electrons of high energy and intensity is converted to two parallel rays before impinging the sample [70]. The transmitted electrons are detected and create a two-dimensional project ion of the sample producing a bright field image. By detecting the diffracted electrons, which are off-angle from the transmitted electrons as seen in Figure 2.5, a dark field image is obtained. Therefore in the TEM image of a material composed of a supported metal, contrast between the metal and the support depends on diffraction, interference and attenuation of the electrons due to density and variation of thickness [103]. Scanning TEM (STEM) is the combination between TEM and scanning electron microscopy (SEM). In (SEM), the surface of the sample is scanned by the electron beam, and the backscattered and secondary electrons are detected as a function of the position of the primary beam [99]. The contrast is caused by orientation where part of the surface facing the detector develop brighter images than the ones facing away from the detector [70]. The secondary electrons, which are the result of inelastic scattering, are low in energy and originate from the surface of the sample. The backscattered ones, which are a result of elastic scattering, originate from deeper within the sample and gives information of the composition of the sample. STEM creates the opportunity to study a small area of the sample which can be investigated separately [103]. An arrangement of ring-shaped detectors allows for high-angle annular dark field (HAADF) imaging which greatly improves the contrast of

the metal and the support.

2.2.4 Electron Dispersive X-ray Microanalasys

Electron Dispersive X-ray Microanalasys (EDX) is a method to determine the chemical composition of a sample as well as which elements that are present including the distribution and concentration [104]. The sample is exposed to an electron beam where an electron from the inner shell of the atom is emitted. Electrons from higher orbital energy shells replace the vacancy, releasing energy in the form of X-rays as illustrated in Figure 2.6. The energy of the X-rays released is unique for each atom. The intensity of the emitted X-rays are proportional to the concentration of the element, which makes it also possible to determine the percentage of each element's concentration within the sample.
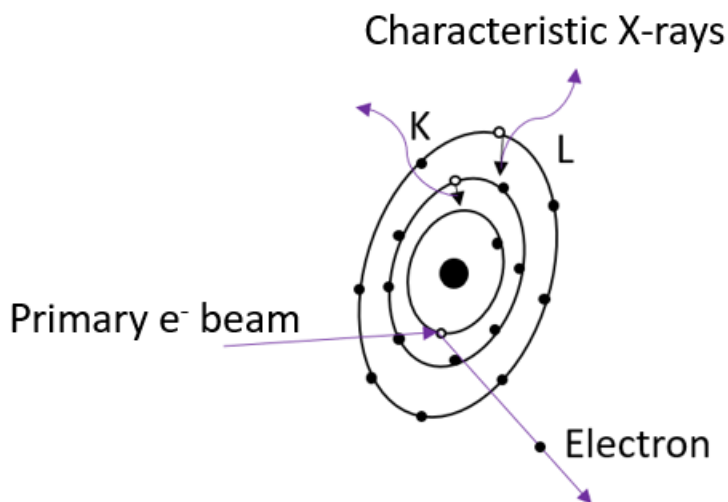
Figure 2.6: An illustration of the production of X-rays by irradiation of a primary electron beam.

The EDX detector is often coupled with SEM or STEM. SEM alone detects backscattered and secondary electrons to obtain different information, but with SEM-EDX, X-rays can also be used as a signal to produce chemical information.

2.2.5 Temperature-Programmed Reduction

Temperature-programmed reduction (TPR) is an analytical method that investigates the surface chemistry of metal oxides under varying thermal conditions [105] and also measures the temperature at which the complete reduction of a material occurs [70]. During the TPR experiment, the temperature of the sample is increased linearly while a reducing gas, such as diluted hydrogen, flows over the solid [99]. The amount of hydrogen consumed is determined by a thermal conductivity

detector which measures the difference in thermal conductivity of the gas before and after flowing over the sample. The resulting TPR profile has qualitative information of the oxidation state of the sample which can work as a fingerprint [106]. In a bi-metallic system TPR can indicates if the two metals are in contact [103]. The TPR of supported bimetallic catalysts often reveals whether the two metals

2.2.6 Oxygen Storage Capacity

Oxygen storage capacity (OSC) is a measure of the amount of oxygen that can be stored and exchanged by a reducible oxide with the active metal or the gas phase [107]. The OSC is measured by determining the amount of reducing gas (H_2 or CO) that is oxidized after passing through a catalyst which has been presaturated with oxygen [16]. The OSC can be measured by either total OSC or dynamic OSC (DOSC) [108]. The total OSC or oxygen storage capacity complete (OSCC) measures the total amount of transferable oxygen which includes both the surface and the bulk oxygen. The OSC under dynamic conditions considers the most reactive and available oxygen species which are mostly located at the surface of the catalyst or in the oxygen vacancies [16].

There are many different ways to measure the OSC depending on the operating conditions [16]. The most common method is to alternately inject pulses of the reducing (CO or H_2) and the oxidizing (O_2) gas [108]. For OSCC this can be achieved by treating the sample in an O_2 atmosphere before flowing Ar or He to sweep away the excess O_2 at the surface [90]. The sample is then exposed to a series of CO pulses until the CO is no longer consumed. The total amount of CO converted or O_2 released in these pulses represents the OSCC. The CO consumption can be described by Reaction 2.4 [109].

$$CO_{(g)} + \frac{1}{2}O_{2(s)} \longrightarrow CO_{2(g)} + \square_{(s)} \tag{2.4}$$
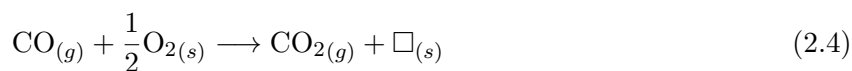
Where (g) represents the gas phase, (s) the solid phase and $\square$ is an empty oxygen vacancy. The dynamic OSC can be measured similar to the OSCC, but the sample is re-oxidized in between each CO pulse by alternately injecting CO and O_2; simulating oscillating conditions [108]. In this way only the most available and reactive O_2-species are reached [90]. By following Reaction 2.4, the total CO_2 produced during one CO injection represent the dynamic OSC.

As the OSCC is measured under thermodynamic equilibrium and the dynamic OSC relates to the rate of O_2 released from the sample there is no direct correlation between the two properties [108]. It has been stated that since the dynamic OSC is measured under oscillating conditions, similar to the ones naturally occurring in the exhaust from the engines, it is more relevant for characterization and evaluation of the activity of the TWC in real operation [16][110].

2.2.7 Diffuse Reflectance Infrared Fourier Transform Spectroscopy

Diffuse Reflectance Infrared Fourier Transform Spectroscopy (DRIFT) is used to analyse the morphology and surface properties of powders and rough surface solids placed inside a DRIFT cell [111][112]. The sample is exposed to an IR beam which migrates inside the sample and interacts with the particles storing up the absorbance [113]. The beam is then reflected by the surfaces of the particles causing it to diffuse. The diffusely reflected light is then collected by a mirror outside of the cell and sends the light to the detector [114].

Typically the DRIFT is used for insitu experiments, where it is possible to study the gas-surface interaction when a certain gas is flowing through the sample [112]. By using CO as the gas, the insitu DRIFT can provide information about the adsorption strength and the geometry of the interaction - whether or not the CO is adsorbed linearly and/or bridged on the surface of the particle [115][116].

2.2.8 X-ray Absorption Spectroscopy

X-ray absorption spectroscopy (XAS) is a characterization method which provides detailed information about the composition, local structure and electronic state of the sample such as the oxidation state [117]. The sample can be measured in gas, liquid or crystalline or non-crystalline solid phase and can be carried out in situ, ex situ or operando.

When measuring XAS, the material is exposed to an incident x-ray with an energy of hv, where the intensity of the x-ray passing through the material, I_x, can be described by Lambert-Beer's law [118]:

$$I_x = I_0 e^{-\mu(E)d} \tag{2.5}$$

where I_0 is the intensity of the incident X-ray, d is the thickness of the material and $\mu(E)$ is the absorption coefficient of the material which is dependent on the energy of the photons. Following Equation 2.5 the absorption of the material decreases with increasing photon energy. Nevertheless, at a certain energy threshold, E_0, a core electron with binding energy of E_b is exited and $\mu(E)$ increases sharply. This is described as the absorption edge of the atom/element under consideration. The energy of the edge varies according to the oxidation state of the element. It increases with the valency of the absorbing atom due to an increase in difficulty to remove an electron from an atom with a higher positive charge. The absorption region around the edge is referred to X-ray Absorption Near Edge Structure (XANES) [70]. Above this energy threshold, when $hv \geq E_b$, the atom absorbs the energy and the electron is expelled to the continuum as a photoelectron with kinetic energy of $E_K = hv - E_b$ [70]. As a photoelectron has both particle and wave character, the waves of the outgoing photoelectron can be scattered by other electrons on the same atom and by a neighbouring atom as seen in Figure 2.7. The interference of the outgoing and scattering waves gives rise to the Extended X-ray Absorption Fine Structure (EXAFS) part of the XAS spectra.

The EXAFS gives information about the number, distance and type of neighbours of the absorbing atom [70].
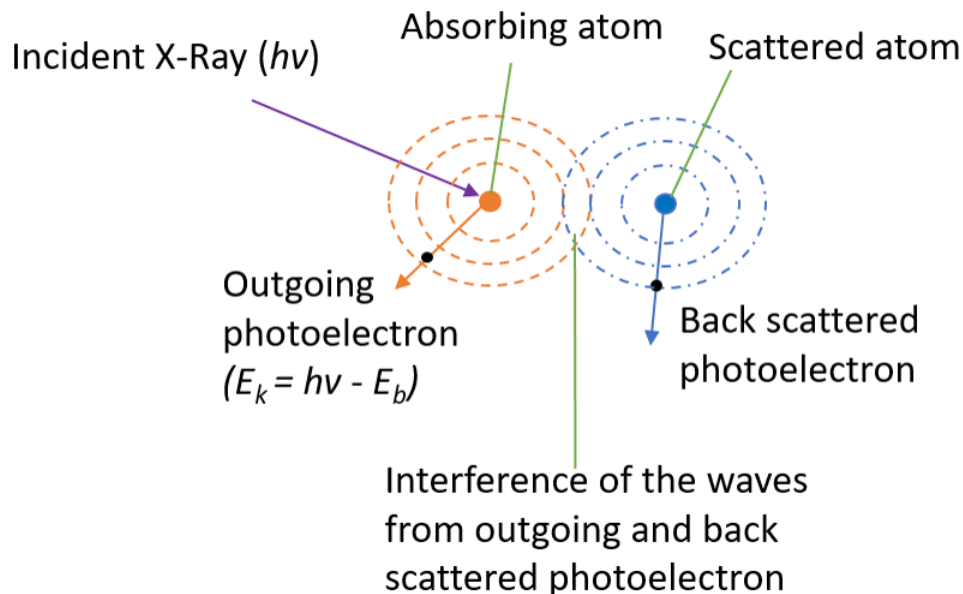
Figure 2.7: Absorption of the energy of an incident X-ray by an atom above the absorption edge E_0 leads to an outgoing photoelectron whos waves are back scattered by neighbouring atoms The interference of the waves is related to the EXAFS signal. Adapted from [119].

2.2.9   Inductively Coupled Plasma Optical Emission Spectrometry

Inductively Coupled Plasma Optical Emission Spectrometry (ICP-OES) is a technique to determine the concentration of an element in a sample [120]. The concentration is determined by exposing a sample to energy in the form of heat from an argon plasma that operates at a temperature of 10 000 K. The atoms absorb this energy which leads to an exciting of an electron to higher energy levels. When the electron returns to its ground state it emits electromagnetic radiation of a specific wavelength of this element. The amount of radiation released is proportional to the concentration of the element that creates the emission.

2.3   Catalytic Activity

In a catalytic reaction the catalyst lowers the activation energy, the energy needed for the reaction to occur, which accelerate the reaction compared to an uncatalyzed reaction as illustarted in Figure 2.8 [70]. For an automobile converter this means that the reactions can take place at much lower temperatures [18].

In automobile emission control the catalytic performance is usually evaluated based on light-off

temperatures, product selectivity and conversion efficiency [121]. The light-off temperature is defined as the minimum temperature where the catalytic reactions are initiated and where the reaction rate increases with an increasing temperature [18].
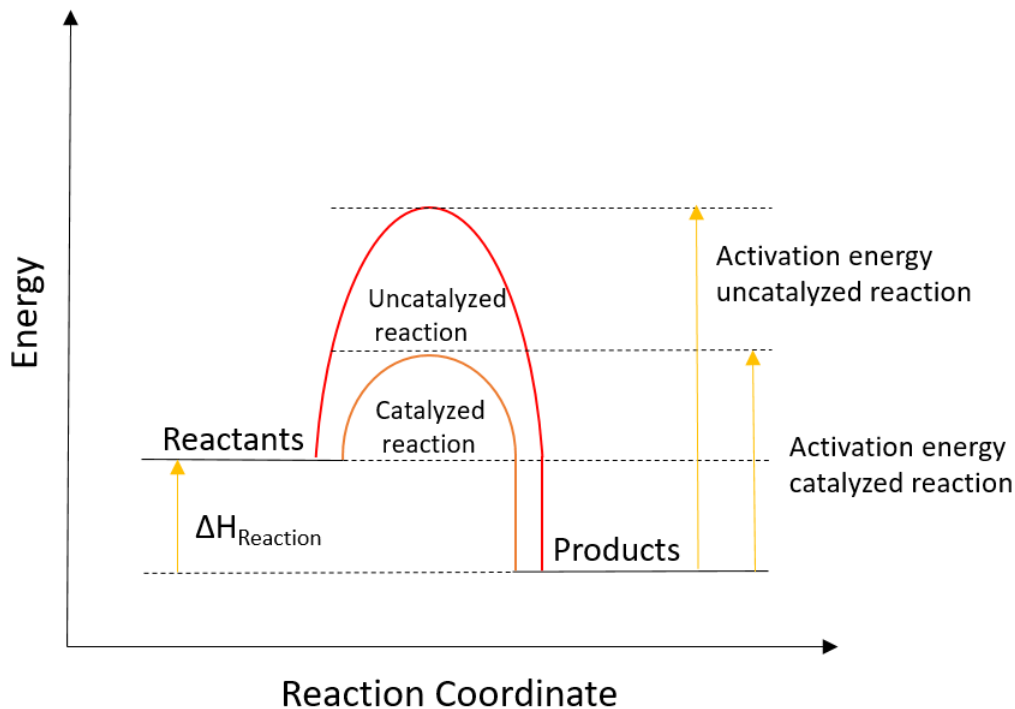
Figure 2.8: Diagram of the activation energy need for a catalyzed reaction compared to an uncatalyzed reaction. Adapted from [18].

The product selectivity is an important factor as many reactions with multiple products can take place in parallel over the catalyst. Even though full conversion is achieved over the TWC unwanted by-products such as NH_3 and N_2O might enter the atmosphere [24]. However, different conditions and catalysts can promote the rate towards the desired products, even if it is less thermodynamically favorable [18]

2.4   Fourier Transform Infrared Spectroscopy

Fourier transform infrared spectroscopy (FT-IR) is a method to identify and quantify IR-active functional groups either in solid, liquid or gas phase [122][123]. During infrared spectroscopy the sample is exposed to IR radiation where the photon energies are not high enough to excite the electrons but instead induce vibrational excitation of the convalent bonds between the different atoms of a molecule. Therefore, all (x) molecules can absorb infrared radiation which can be reconverted into bond vibrations with specific frequency (usually converted to wavenumber) [123].However, a vibration needs to induce a change in the dipole moment to be able to absorb infrared energy.

Hence, not all molecules are infrared visible (i.e. N2, H2, Ar). This is the reason why FTIR are usually used in addition to MS when performing catalytic tests which involve infrared invisible compounds.

These wavelengths are characteristic for the vibration and rotation of the chemical bonds in the specific molecule, and does therefore function as a "fingerprint" of the molecules in the sample [124]. A frequency spectrum over the IR-range (4000-400 cm^{-1}) is required to analyze all possible molecules in the sample which is obtained by a Fourier transformation (FT) which "decodes" each individual frequency detected.

2.5 Mass Spectrometry

Mass spectrometry (MS) is an analytical method to calculate exact molecular weight of a sample or, as in this case, identify and quantify compounds by measuring the mass-to-charge ratio (m/z) [125]. In order to measure the m/z ratio, the molecules are converted to gas-phase ions through different methods such as electrospray ionization (ESI), matrix-assisted laser desorption/ionization (MALDI) or electron ionization (EI) [126].

Through ionization by EI a small fraction of the molecules in the gas phase are bombarded with low energy electrons which results in multiple positive charged ions [127]. The ions are then separated and organized according to their mass-to-charge ratio through an electric field in the mass analyzer. There are many different types of mass analyzers on the market, where one of them is the Quadrupole mass analyzer [125]. The quadrupole mass analyzer consists of four rods where an electrical voltage is created between two pairs of rods [128]. When the ions enters the rods, only ions with a specific mass-to-charge ratio will reach the detector due to its certain voltage [129]. This allows the user to specify a range of mass-to-charge ratios by changing the applied voltage between the rods. The ions are then detected and a mass spectrum is generated where the m/z ratio of the ions is plotted against its intensity, which is linear to the concentration of the detected molecule [125].

Chapter 3

Experimental methods

3.1 Material Preparation

In this project, 2 wt% Pd/Al_2O_3, 0.8 wt% Rh/Al_2O_3 and bimetallic Pd-Rh/Al_2O_3 (3:2 ratio) were prepared by incipient wetness impregnation of aluminum oxide (γ-Al_2O_3) using Pd nitrate solution and Rh nitrate solution.

The ceria-zirconia (CZ) support was prepared by a co-precipitation method based on the work of Li et al.[90] aiming for a Ce/Zr molar ratio of $0.7 : 0.3$ ($Ce_{0.7}Zr_{0.3}O_2$). The CZ support was then impregnated with either Pd (2 wt%) or Pd-Rh (3:2).

A summary of the samples prepared and their corresponding sample code can be found in Table 3.1.

Table 3.1: Summary of the samples prepared and their corresponding sample code.

Prepared sample	Sample Code
2 wt% Pd on alumina	Pd/A
0.8 wt% Rh on alumina	Rh/A
1.2 wt%Pd-0.8 wt% Rh on alumina	Pd-Rh/A
0.8 wt% Rh on CZ	Rh/CZ
1.2 wt%Pd-0.8 wt% Rh on CZ	Pd-Rh/CZ
Mechanical mix of Pd/A and Rh/A	PdA_RhA

3.1.1 Synthesis of Ceria-Zirconia

CZ was synthesized by a co-precipitation method where Cerium (III) nitrate hexahydrate (Fluka) and Zirconium (IV) oxynitrate hydrate (Aldrich) were used as precursors. The precursors were dissolved in de-ionized H_2O in the correct molar ratio of Ce:Zr under stirring. As a complexing agent citric acid monohydrate (Labochem international) was dissolved in the solution in a molar ratio of citric acid:(Ce + Zr) = 1.2. Ammonium hydroxide (Merck) was then added drop-wise until the solution reached a pH $\sim$ 3 which was measured with a SevenCompact pH-meter (Mettler Toledo). The solution was then stirred for 3 h before being filtered and washed with de-ionized H_2O until a constant pH was obtained. The white precipitate was dried at 110 °C for 2 h and then calcined in air at 500 °C for 4 h with a ramp of 5 °C/min.

3.1.2 Incipient wetness impregnation

Prior to the synthesis the liquid absorption capacity or IWI point of the supports, commercial aluminum oxide (γ-Al_2O_3, Puralox; Sasol) and CZ, were determined. To do so distilled H_2O was added drop-wise to the support previously dried at 120 °C overnight (to ensure full water desorption from the pores) until it appeared completely saturated.

The precursors used for the synthesis were an aqueous solution of Palladium (II) nitrate (Alfa Aesar, 4-5 wt% solution) and Rhodium (III) nitrate (Alfa Aesar, 32 % Rh assay). The Rh-precursor was diluted in distilled H_2O and stirred at room temperature for 1.5 h to obtain a 5 wt% Rh metal aqueous solution. The calculations can be found in Appendix A.1.1. To prepare the bi-metallic Pd-Rh catalysts, the Pd and Rh solutions were mixed in the appropriate amount required to to obtain a Pd:Rh molar ratio of 3:2 and stirred for 2 h at room temperature.

Prior to the impregnation, the Pd, Rh and Pd-Rh precursors were further diluted with distilled H_2O until reaching approximately 80 % of the IWI point. The prepared precursor solution was then added drop wise to the dry support (dried at 120 °C overnight), while stirring the mixture from time to time. The impregnated support was then calcinated in air at 550 °C for 3 h, with a heating ramp of 5 °C/min.

3.2 Characterization

3.2.1 X-ray Diffraction

The powder samples were flattened on silicon XRD-holders prior to the measurement. The XRD pattern were acquired using a Bruker D8 Advanced with Ni-filtered Cu Kα radiation (40 kV and 40 mA). The XRD data was collected in the 2θ range of 10 °- 100 °using a step size of 0.001 °and a step time of 2 s.

The in situ XRD diffractograms were collected using XRK 900 chamber which was placed in the Bruker D8 Advanced instrument. Sieved samples in the range of 150 - 200 µm were placed on the

sample holder.

In situ XRD was conducted on PdA, PdRhA and PdA_RhA (mix):

-Exposed to 2 vol% H_2 in N_2 and XRD was measured at 60, 170, 300, 450 and 600 °C.

-Exposed to 2 vol% O_2 in N_2 and XRD was measured every 25 °C from 600-300 °C.

3.2.2 N_2-physisorption

The nitrogen adsorption and desorption isotherms were measured at 77 K and obtained using a Quantachrome Autosorb-1 instrument. The specific surface area was estimated by applying the multi-point BET equation to the N_2-physisorption isotherm using 5 points between 0.1 - 0.35 $\frac{P}{P_0}$ corresponding to a linear line. The samples (ca. 200 mg) were degassed under high vacuum prior to physisorption at 350 °C for at least 6 h.

3.2.3   Transmission Electron Microscopy

The Transmission Electron Microscopy (TEM) and STEM-EDX (scanning TEM Elctron Dispersive) analysis was performed by Dr. Ivo Alxneit from the ACS group. Prior to the analysis the samples were first suspended in 2-propanol and then deposited on a copper grid coated with holey carbon film. The electron microscopy was performed on a probe corrected JEOL JEM ARM-200F (NeoARM) equipped with a cold FEG gun operated at 200 keV. The EDX-maps were collected by two SDD detectors together covering 1.7 sr with a swell time of 0.5 ms and 50 sweeps for maps. From the electron micrographs of each sample, the particle size was calculated by measuring at least 200 noble metal particles by using the ImageJ software.

3.2.4   Oxygen Storage Capacity

The (Oxygen Storage Capacity) OSC was measured in a fixed-bed quartz reactor inserted in the set-up illustrated in Figure 3.2. The OSC was estimated by simulating oscillating conditions where 1 vol % CO in Ar and 1 vol % O_2 in Ar were alternately flown on the samples with 5 min (OSC) or 30 s (Dynamic OSC) intervals at 300, 450 and 600 °C. The OSC is expressed as µmol O_2 g_{cat}^{-1} and was calculated based on the amount of CO_2 produced when CO was flown on the samples (therefore consuming the O_2 stored in the material). The CO_2 signal measured by mass spectrometry (MS, InProcess GAM400) was calibrated in order to quantify it.

3.2.5   Temperature Programmed Reduction

Temperature Programmed Reduction (TPR) was performed using a Micromeritics AutoChem HP apparatus. The quartz reactor was loaded with 50 mg sieved sample (150 - 200 µm). The samples were first pretreated in 10 vol% O_2 in He (20 mL/min) from RT to 600 °C (10 °C/min). The system was cooled down to 40 °C (50 °C/min) and purged with He for 10 min. The measurements were conducted under 10 vol% H_2 in Ar (20 mL/min) from 40 to 850 °C (5 °C/min), where the temperature was constant for 5 min before being cooled down. The H_2O formed during the

measurements were prevented from the detector by a cold trap of 2-propanol and liquid N_2. The outlet H_2 concentration was calculated by thermal conductivity method.

3.2.6 CO Diffuse Reflectance Infrared Fourier Transform Spectroscopy

Diffuse Reflectance Infrared Fourier Transform Spectroscopy (DRIFT) measurements were collected using a VERTEX 70 FT-IR spectrometer (Bruker Optics) equipped with a diffuse reflectance accessory (Praying Mantis, Harrick) and a MCT detector which was cooled with liquid nitrogen. Prior to the measurements the samples were reduced under a flow of 3 vol% H_2 in Ar at 50 mL/min at 300 °C for 30 min with a ramp of 10 °C/min. The system was cooled to room temperature and purged with Ar for a few minutes to obtain the background. The experiment was performed under 1 vol% CO in Ar at 50 mL/min at room temperature. The spectra were recorded by co-adding 100 scans at a resolution of 4 cm^1 and 10 Hz.

3.2.7 X-ray Absorption Spectroscopy

Ex situ X-ray Absorption Spectroscopy (XAS) was performed on samples that where "frozen" at certain temperatures during activity testing or pretreatment. The samples were frozen by flowing Ar only over the sample while cooling down to room temperature from the desired temperature in order to gain information about the oxidation state of the metal at this point. Ex situ XAS measured at the Pd K-edge (24 350 eV [130]) and Rh K-edge (23 220 eV [131]) at the SuperXAS beamline of the Swiss Light Source (SLS, Paul Scherrer Institute). Before measurements 50 mg of the powdered samples were pressed into 8 mm diameter pellets. The incident X-ray beam was adjusted using a mirror coated with Pt at 2.9 mrad prior to monochromatization where a channel-cut Si(111) crystal cooled with liquid nitrogen was used. The monochromatic beam was focused by using a Pt-coated toroidal mirror. The monochromator was oscillated at 4 Hz corresponding to a time resolution of 0.25 s per spectrum. The spectra were collected at room temperature in fluorescent mode and a Pd or Rh reference foil was measured simultaneously as a calibration. Linear combination fitting and calibration of the energy were performed with ProXAS software [132]. The fitting of the Extended X-ray Absorption Fine Structure (EXAFS) was conducted with FEFF included in the Artemis software [133].

3.2.8 inductively Coupled Plasma Optical Emission Spectrometry

Inductively Coupled Plasma Optical Emission Spectrometry (ICP-EOS) measurements were performed at PSI. The concentration of the elements in the samples was estimated by a Varian Vista AX spectrometer. Prior to the measurements he samples were dissolved in a hydrofluoric, hydrochloric and nitric acids mixture. Calibration solutions were based on 99.999% pure commercial standards. The concentration of the elements were determined by an average of atomic emission lines of three measurements.

3.3   Activity Testing

The catalytic activity was measured using a quartz glass plug-flow reactor packed with 50 mg of sieved catalyst (150-200 μm) mixed with 150 mg of sieved cordierite (100-150 μm) between to quartz wool plugs (Figure 3.1). The reactor was placed in a heating oven and the temperature was measured by a thermocouple type K placed at the middle of the catalyst bed as illustrated in the schematic set-up in Figure 3.2. The outlet gas was analyzed by mass spectrometry (MS, InProcess GAM400) and FTIR (Bruker ALPHA II).

Figure 3.1: The quartz glass plug-flow reactor loaded with 50 mg of catalyst mixed with 150 mg of cordierite.

3.3.1   oxidation Pretreatment

The catalysts were exposed to an oxidation pretreatment prior to testing under 0.15 vol% CH_4, 0.6 vol% O_2 in Ar at a WHSV of 240 h^{-1} g_{cat}^{-1} while being heated from $200 - 600\,°C$ ($10\,°C$/min) in order to stabilize and ensure that all the catalysts were in the same state before experiments. The temperature was constant at $600\,°C$ for 30 min before being cooled down to desired temperature.

3.3.2   reductive pretreatment

Stoichiometric temperature ramps were also conducted on the catalysts after a reductive pretreatment. Prior to the temperature ramps, the catalyst was exposed to 0.15 vol% CH_4, 0.6 vol% O_2 in Ar at a WHSV of 240 h^{-1} g_{cat}^{-1} while being heated from $200 - 600\,°C$ ($10\,°C$/min). The temperature was constant at $600\,°C$ for 30 min before the feed was changed to 2 vol% H_2 in Ar. The temperature stayed at $600\,°C$ for 5 min, before being cooled down to $300\,°C$ to start the temperature ramps as described in the previous section.

3.3.3   Stoichiometric Temperature Ramps

The stoichiometric temperature ramps were measured under 5 vol% H_2O, 0.15 vol% CH_4, 0.16 vol% NO, 0.7 vol% CO and 0.57 vol% O_2 corresponding to $\lambda = 1$ balanced in Ar. The measurements were performed during three temperature cycles of heating and cooling between 300 - $600\,°C$ with a ramp of $5\,°C$/min with a WHSV of 240 L h^{-1}.

3.3.4   Steady State Lambda Sweeps

Isothermic steady state lambda sweeps were conducted over different λ-values by varying the O_2 concentration and the corresponding Ar balance in the feed. The rest of the feed had a constant concentration of 5 vol% H_2O, 0.15 vol% CH_4, 0.16 vol% NO and 0.7 vol% CO. The experiment started at $\lambda = 1.2$ and step wise decreased to $\lambda = 0$ and was step wise reincreased to $\lambda = 1.2$ again.

The λ-values and the corresponding O_2 concentration are listed in Table 3.2.

Table 3.2: λ-values and the corresponding O_2 concentration used during the steady state lambda sweeps

λ	1.20	1.15	1.10	1.05	1.00	0.95	0.90	0.85	0.80	0.75
O_2	0.68	0.66	0.63	0.60	0.57	0.54	0.51	0.48	0.46	0.43
λ	0.70	0.65	0.60	0.55	0.50	0.40	0.30	0.20	0.10	0.00
O_2	0.40	0.37	0.34	0.31	0.29	0.23	0.17	0.11	0.06	0.00

3.3.5 Cyclic Steady State O_2 Dithering

At a constant temperature, steady state O_2 dithering experiments were performed by pulsing O_2 at different amplitudes, A, around stoichiometric conditions such as $\lambda = 1 \pm A$. Each amplitude was tested under different frequencies of 0.033, 0.05, 0.1 and 0.2 Hz. If an amplitude of 0.15 with a frequency of 0.2 Hz were tested, a full rich/lean cycle would correspond to an O_2 feed of $\lambda = 0.85$ for 5 s and then $\lambda = 1.15$ for 5 s. During the cycles the rest of the feed was held constant as during the steady state lambda sweeps (Section 3.3.4). Each dithering condition was held for 5 min to obtain a cyclic steady state.

3.3.6 Calculations

The CH_4 and NO conversion was calculated based on Equation 3.1.

$$X_i = \frac{F_{i,in} - F_{i,out}}{F_{i,in}} \cdot 100\% \tag{3.1}$$

where X_i is the conversion of i (i = CH_4 or NO), $F_{i,in}$ is the flow entering the reactor whereas $F_{i,out}$ is the flow of CH_4 or NO leaving the reactor. This flow can be described by the total flow in and out of the system, $F_{tot,in}$ and $F_{tot,out}$, and each specie's molecular fraction, y_i, Equation 3.1 can be written as seen in Equation 3.2.

$$X_i = \frac{y_{i,in}F_{tot,in} - y_{i,out}F_{tot,out}}{y_{in}F_{tot,in}} \cdot 100\% \tag{3.2}$$

The MS signal obtained from the mass spectrometer for each species is linear with the concentration or the molecular fraction of the species through Equation 3.3

$$y_i = k_i \cdot MS_i \tag{3.3}$$

where K_i is a constant and MS_i is the MS signal of the corresponding specie. Combining Equation 3.2 and 3.3 and the fact that $F_{tot,in} = F_{i,out}$, the conversion can be simplified to Equation 3.4:

$$X_i = \frac{MS_{i,in} - MS_{i,out}}{MS_{i,in}} \cdot 100\% \tag{3.4}$$

To obtain the concentration of the species through the mass spectrometer a calibration of known concentrations, such as the feed, was conducted prior to any experiments and the concentration

was calculated by Equation 3.5 based on Equation 3.3.

$$y_{i,out} = \frac{MS_{i,in} \cdot MS_{i,out}}{MS_{i,in}} \tag{3.5}$$

The CO, N_2O and NH_3 concentration were estimated from linear regression equations based on a calibration of known concentration of the respective gases in the FTIR. The regression curves can be found in Appendix B.

The concentration of O_2 in the feed was based on λ which in this project was calculated by Equation 3.6.

$$\lambda = \frac{[O_2]_{in}}{\frac{1}{2}[CO]_{in} + 2[CH_4]_{in} - \frac{1}{2}[NO]_{in}} \tag{3.6}$$

where $[i]_{in}$ is the concentration in the feed of component i.
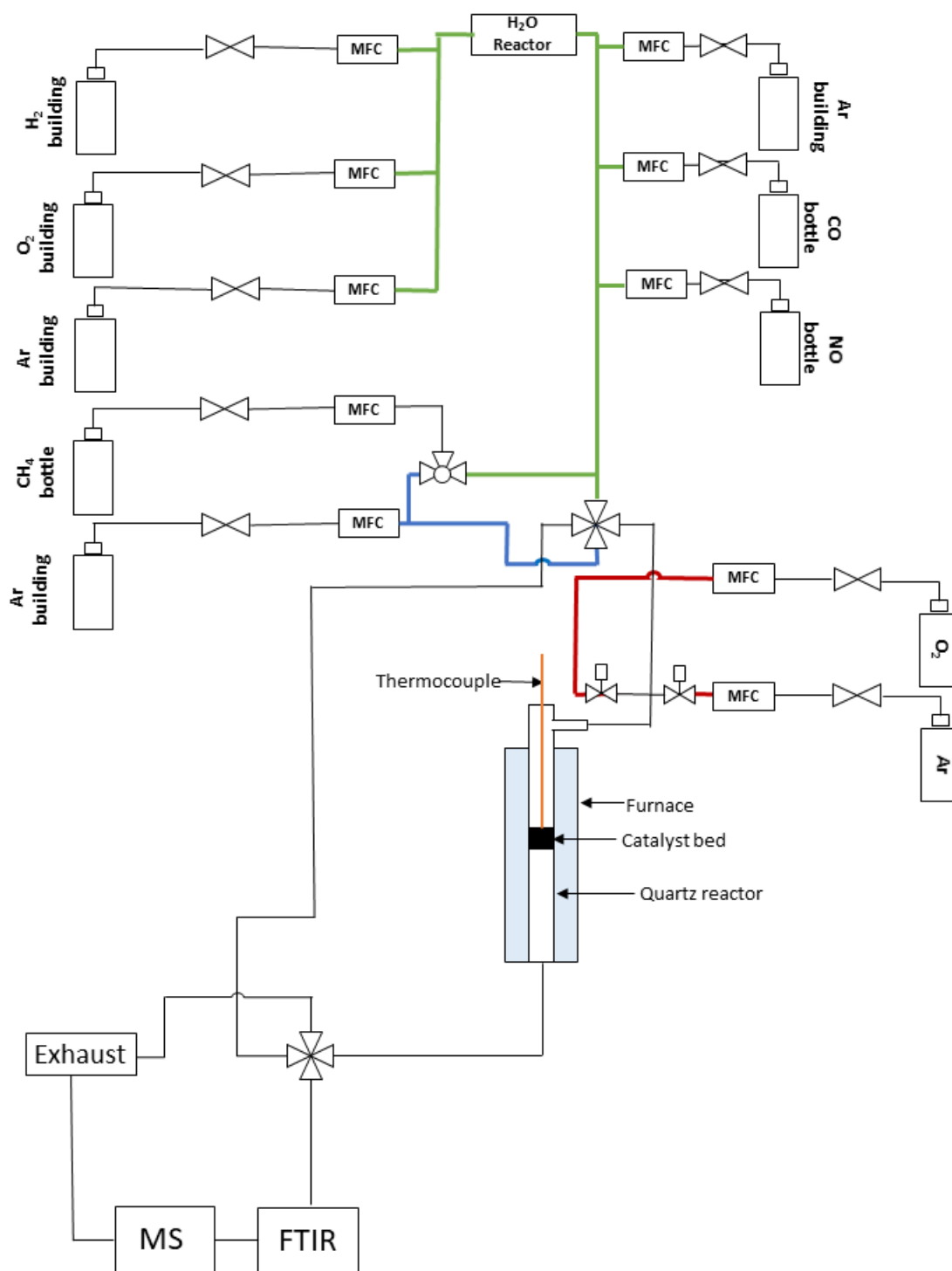
Figure 3.2: Flow sheet of the TWC model gas set up. The green line represents the main line, the blue line is the secondary line and the red line corresponds to the pulsing lines.

Chapter 4

Results and Discussion

4.1 Catalyst Characterization

4.1.1 Inductively Coupled Plasma Optical Emsission Spectrometry

The elemental analysis obtained by ICP-OES allowed to get information on the metal content, as well as the Ce/Zr ratio (Table 4.1). The obtained loading of Pd on Pd/A was 1.64 wt% which matched well with the aim of 2 wt%. For Pd-Rh/A, the metal content was found to be 1.05 wt% and 0.82 wt% for Pd and Rh respectively, which is close to the aimed values (i.e. 1.2 wt% and 0.8 wt%). On Rh/A and Rh/CZ, the Rh content resulted in 0.71 wt% and 0.67 wt% respectively, corresponding to a deviation of 0.09 wt% and 0.13 wt% which is within a respectable error. The Ce/Zr ratio was obtained from Rh/CZ and resulted in a ratio of 0.72 : 0.28, not far from the aimed ratio of 0.70 : 0.30. Unfortunately, the results of the elemental analysis of Pd-Rh/CZ were not ready in time for this thesis. However, as the CZ support is the same as Rh/CZ and the calculations are similar as to Pd-Rh/A, Pd-Rh/CZ was assumed to be comparable to the other samples.

Table 4.1: Elemental analysis of the synthesized samples obtained from ICP-OES.

Sample	Pd/A [wt%]	Pd-Rh/A [wt%]	Rh/A [wt%]	Rh/CZ [wt%]
Al	52.22	50.70	52.20	-
Ce	-	-	-	59.59
Pd	1.64	1.05	-	-
Rh	-	0.82	0.71	0.67
Zr	-	-	-	22.93

4.1.2   X-ray Diffraction

The XRD patterns of the Pd, Rh and Pd-Rh alumina and CZ based samples were collected in order to detect the different crystal phases. γ-Alumina was observed with the most intense peak at 67.1°in all the alumina samples, confirming that the alumina maintained the γ-alumina form through the synthesis (Figure 4.1). The XRD patterns of the Pd-based samples (c.f. Pd-Rh/A, Pd/A, Figure 2.3; Pd-Rh/CZ, Pd/CZ, Figure 4.2), did not display any reflections corresponding to metallic Pd (39.4°and 45.9°). However, PdO was detected with the most intense peak at 33.9°for Pd/A and Pd-Rh/A [42]. For Pd-Rh/CZ, the main PdO reflection overlapped with that of ceria zirconia and was not observed at the higher angles (i.e. 42.2°and 54.8°[134], Figure 4.2)). Rh was not detected on any of the Rh containing samples due to the low amounts of Rh in the catalyst. The main peak for the CZ support (Figure 4.2) was observed at 29.1°which was shifted to higher 2θ compared to pure ceria with the most intense peak at 28.3°[135]. This indicates that Zr^{4+} was incorporated into the CeO_2 lattice [90].
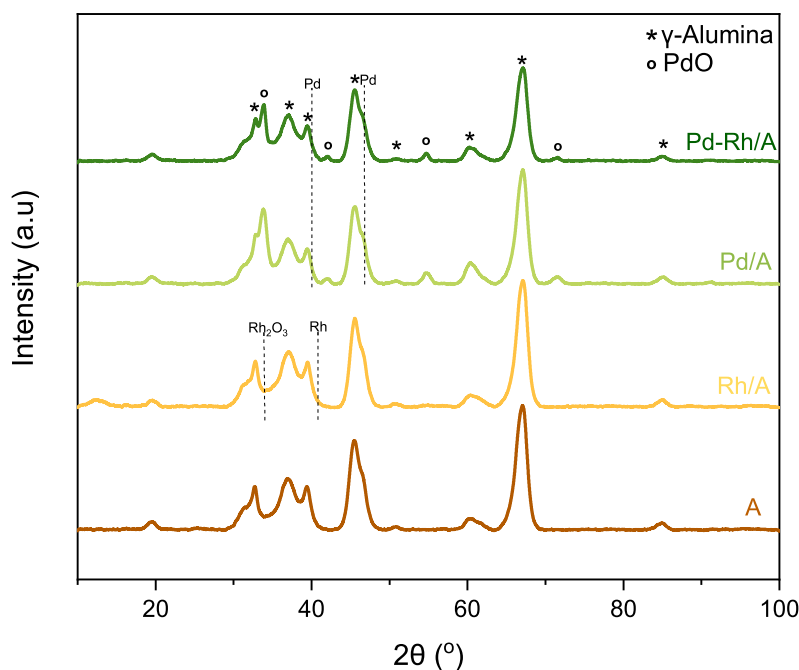
Figure 4.1: Powder XRD patterns of the alumina-based samples.
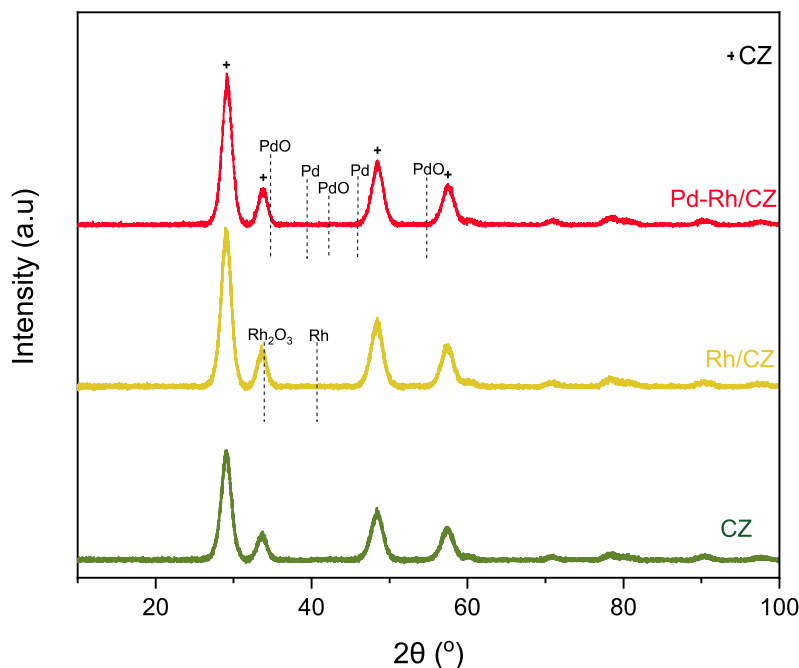
Figure 4.2: Powder XRD patterns of the CZ-based samples.

4.1.3 N$_2$-physisorption

N$_2$-physisorption was performed on the samples to obtain the surface area (SA) as well as the pore volume and the pore size distribution (Table 4.2). Though the loss of SA and pore volume for the metal-alumina samples compared to alumina was not significant, it was possibly due to the deposition of Pd and Rh particles in the alumina pores together with the calcination preformed after impregnation. The difference in SA between the CZ-based samples and alumina-based samples, however, is due to the type of support since γ-alumina is well known for its high specific SA [70]. While the SA of CZ depends on the preparation method and the Ce/Zr ratio [90][136]. The same trend was observed for the CZ-based samples where the SA and pore volume decreased when Pd and Rh were deposited. The average pore diameter of the samples, that were obtained from the pore size distribution (Appendix D), corresponded to mesoporus materials [70]. This was further confirmed by the adsorpion-desorption isotherms where all the isotherms in Figure 4.3 exhibited a well-defined hysteresis loop. This shape corresponds to isotherm type IV, which was assigned to mesoporous materials, a result of the γ-Alumina and CZ support (see Figure 2.4 in Section 2.2.2 for assignment).

Table 4.2: The properties from N_2-physisorption of the prepared samples using the BET equation for the surface area and BJH equation on the desorption isotherm for the pore volume and diameter.

Samples	Surface area [m2/g]	Pore volume [cm3/g]	Ave. Pore diameter [nm]
Alumina	150.8	0.33	9.9
Pd/A	147.2	0.31	9.9
Rh/A	150.6	0.32	9.8
Pd-Rh/A	147.0	0.31	9.9
CZ	35.5	0.21	3.6
Rh/CZ	30.9	0.22	3.6
Pd-Rh/CZ	33.2	0.17	2.8
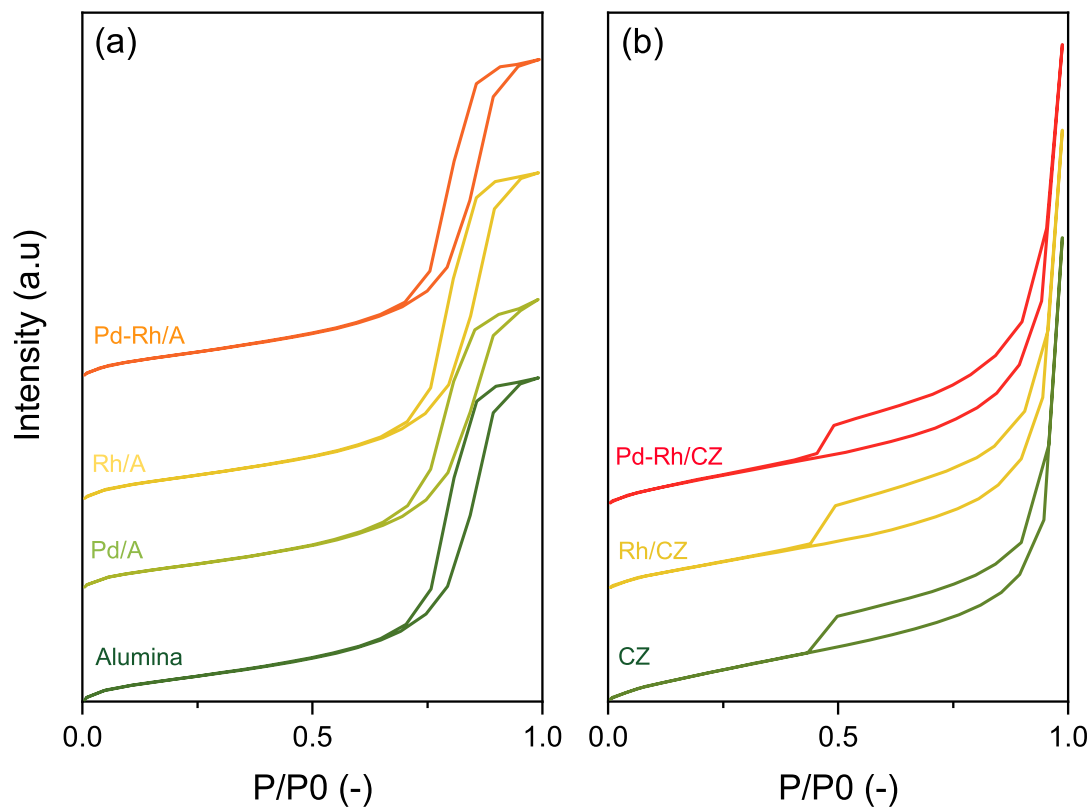
Figure 4.3: Adsorption-desorption isotherms obtained by N_2-physisorption for (a) the alumina-based samples and (b) the CZ-based samples.

4.1.4   H$_2$-Temperature Programmed Reduction

The H$_2$-TPR was measured to examine the redox properties of the samples and the metal-support interactions [137]. As shown in Figure 4.4 a negative peak at 79 °C was observed for Pd/A and Pd-Rh/A which was due to the decomposition of PdH$_x$ species which were formed by interaction of metallic Pd and H$_2$ [138][139]. The higher intensity of the peak for Pd/A was due to a higher concentration of Pd present on the support (2 wt % Pd/A and 1.2 wt % Pd-Rh/A). Since no negative peaks were observed below 79 °C, it suggest that the PdO species had already been reduced at room temperature. On the contrary, a positive peak of 81 °C was observed for Pd-Rh/CZ which can be ascribed to the reduction of PdO species highly dispersed on the surface of the support [136]. The reduction peak was also broader over the CZ support compared to the alumina support, though the metal content was similar, which is most likely due to O$_2$-back spillover from the CZ keeping the Pd oxidized longer.
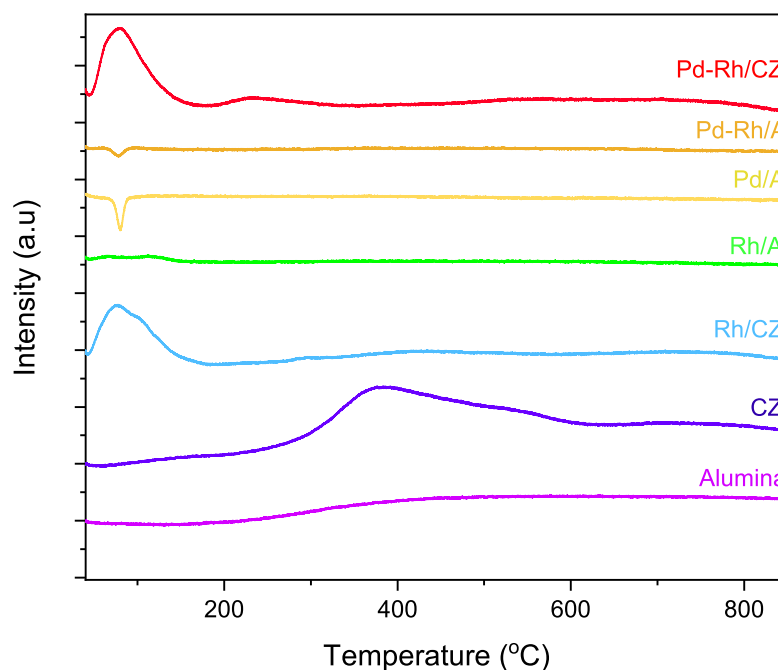
Figure 4.4: H$_2$-TPR profiles of the alumina and the CZ-based samples.

The peaks of 66 °C and 115 °C for Rh/A were ascribed to the reduction of Rh$_2$O$_3$ species of different sizes on the support [140][141][142]. The peaks were more intense and broad on Rh/CZ and were shifted to 75 °C with a shoulder at 106 °C, indicating that the CZ support was maintaining Rh in an oxidized state [143]. The same observation was made for Pd-Rh/CZ. Unlike alumina, CZ is a reducible support with an intense peak at 384 °C which arises from the reduction of surface Ce^{4+}

[90]. The shoulder present at 532 °C was related to the reduction of the bulk Ce^{4+} [144]. These peaks were barely, or not at all, observed on Rh/CZ and Pd-Rh/CZ, which confirms that a back spillover of O_2 from CZ to the metal is taking place [76][141][143].

4.1.5 Transmission Electron Microscopy

(S)TEM images of the samples were obtained to estimate an average particle size for all samples and to get an idea of the shape and structure of the particles. The average particle size (Table 4.3) were based on the respective particle size distribution found in Appendix C. The particle size of the noble metals were found to be larger when deposited on alumina-support compared to CZ-support. The smaller particle sizes were a factor of CZ promoting dispersion of the metal which leads to smaller particles on the metal-CZ interface [143].

Figure 4.5 represents selected (S)TEM images of Pd/A, Rh/A, Pd-Rh/A, Rh/CZ and Pd-Rh/CZ. On the alumina-based samples the metal particles were easily observed due to a high contrast between the metal and the support (due to the low molar mass of Al compared to Pd or Rh). The larger particles (ca. 5 - 10 nm) exhibited edges as indicated by the blue boxes in Figure 4.5 on all the alumina-based samples. From the images it was also clear that the metal particles have agglomerated in bigger clusters especially for Pd/A and Rh/A.

Table 4.3: A summery of the average particle size of all samples with the errors obtained from Origin Software.

Samples	Av. Particle size [nm]
Pd/A	7.0 ± 2.9
Rh/A	7.0 ± 2.7
Pd-Rh/A	6.3 ± 0.2
Rh/CZ	4.3 ± 1.1
Pd-Rh/CZ	3.2 ± 1.2
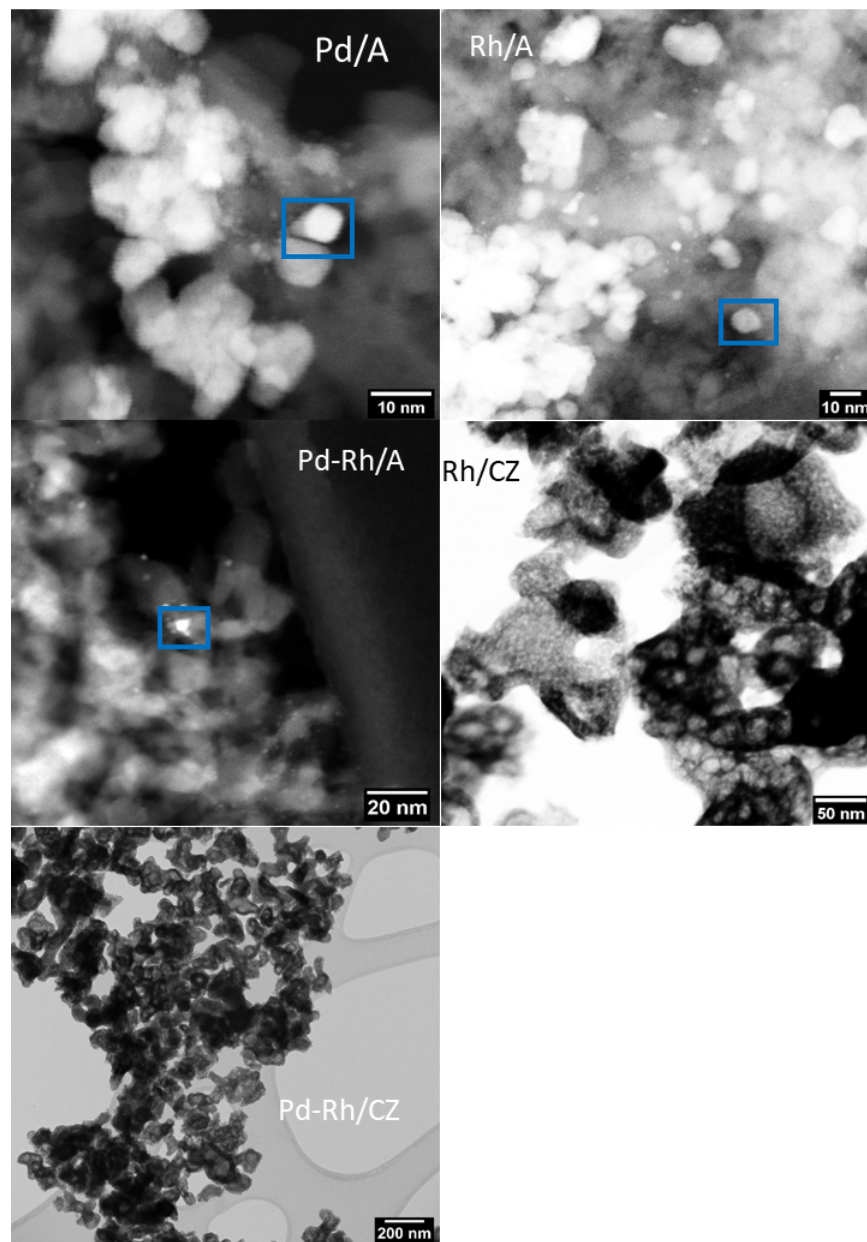
Figure 4.5: (S)TEM images of Pd/A, Rh/A, Pd-Rh/A, Rh/CZ and Pd-Rh/CZ.

On the images of the CZ-based samples it was more complex to distinguish the metal particles from the support. However, the crystallization of CZ was very clear, especially on the image of Pd-Rh/CZ. On Rh/CZ and CZ it seemed like the CZ had formed a foam like structure. This was also visible in the TEM image of CZ in Figure 4.6b at the upper left corner. However, the ratio map obtained from an EDX-mapping performed on the same image did not show the foam structure. Thus the individual agglomerates are chemically homogeneous. Figure 4.6 also displayed the Zr/Ce ratio based on the X-ray intensity where it seemed there were two types of CZ present,

one ceria-rich part evident by the dark red areas, and a more equally distributed part observed from the brighter colors. The very high Zr/Ce around 2 were probably artifacts. They were present in regions where there was mostly noise such as in the vacuum, on the carbon support and at the very fringe of the agglomerates as seen in Figure 4.6b.
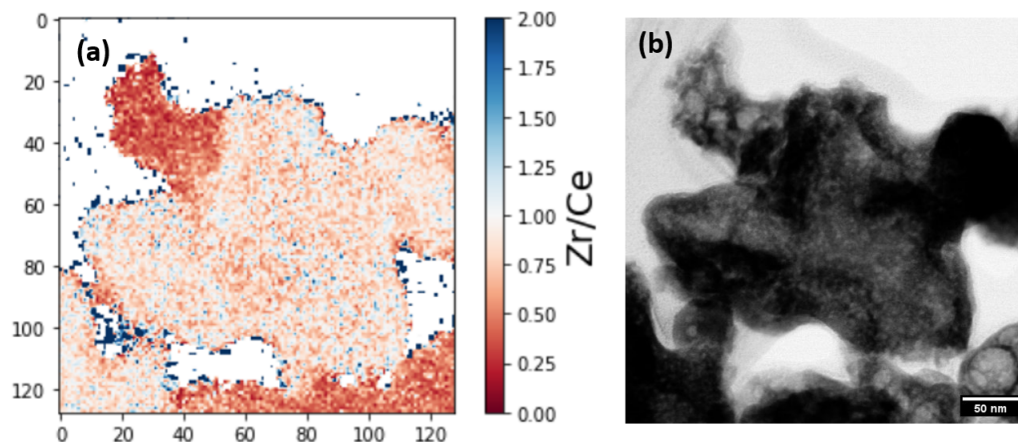
Figure 4.6: (a) Zr/Ce ratio obtained from EDX-mapping on the (b) STEM image of CZ. Here showed as dark field STEM.

4.1.6 Diffuse Reflectance Infared Fourier Transform Spectroscopy

The first peak at 2171 cm^{-1} for all samples corresponds to unreacted CO in the gas phase and works as an alignment for a better comparison of the spectra. For all samples containing Rh there were observed distinct doublets at (2085 ; 2013), (2072 ; 2012), (2087 ; 2014) and (2088 ; 2016) for Rh/A, Rh/CZ, Pd-Rh/A and Pd-Rh/CZ respectively corresponding to symmetric and asymmetric CO-stretches of bicarbonyls adsorbed on Rh (Rh-(CO)$_2$) [145][146]. The higher intensity and the broader peaks for Pd-Rh/A and Pd-Rh/CZ indicate a contribution of Pd on Rh suggesting a synergistic behaviour in the bimetallic samples. Small shoulders at 2050 cm^{-1} were identified on Rh/A, Rh/CZ and Pd-Rh/A and were ascribed to CO adsorbing linearly on Rh [146]. The shoulder was not detected on Pd-Rh/CZ due to the broad peak from the attribution of Pd. A peak of 2123 cm^{-1} was observed for the Pd/A sample, an indication of CO adsorbed on positively charged Pd particles [147]. The peak at 2093 cm^{-1} comes from linearly bonded CO on the Pd surface sites [147]. Additional peaks were observed below 2000 cm^{-1} for Pd containing samples, where the peak at 1985 cm^{-1} for Pd/A was assigned to CO adsorbed as bridged species on metallic Pd edges [148]. Furthermore, a peak at 1941 cm^{-1} also corresponded to bridged bound CO species, on metallic Pd exposed to the surface [149]. The same peaks were detected on Pd-Rh/A and Pd-Rh/CZ, but as a shoulder at 1994 cm^{-1} on Pd-Rh/CZ. The peak at 1941 cm^{-1} for Pd/A was shifted to a lower wavenumber and broader peak for both Pd-Rh/A and Pd-Rh/CZ showing the effect of Rh addition.
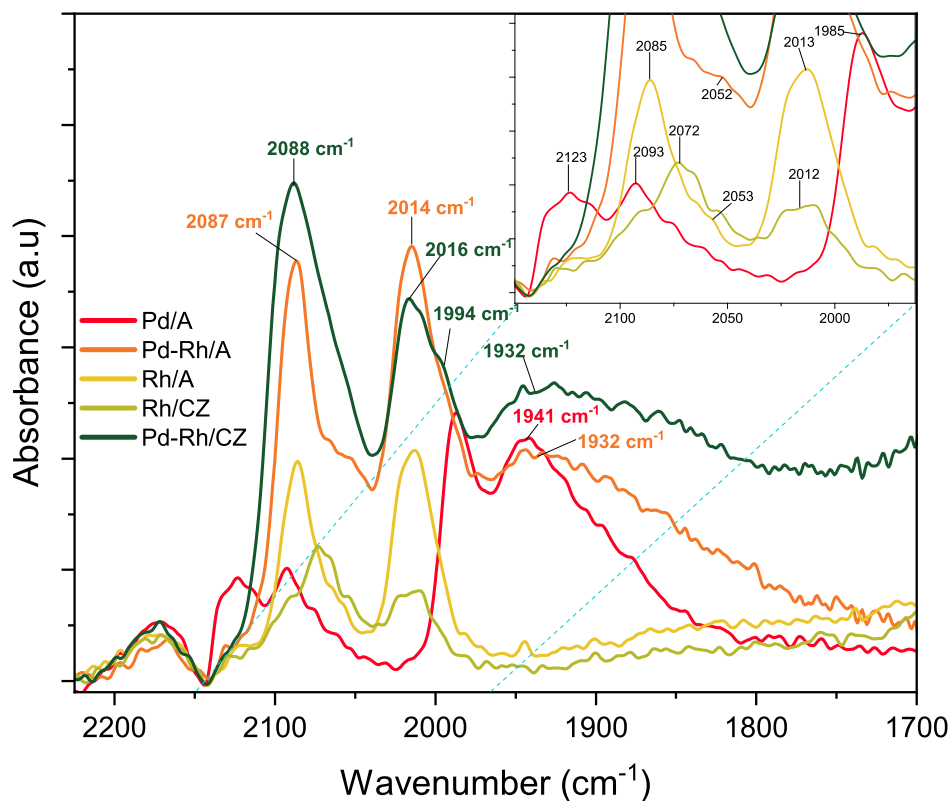
Figure 4.7: DRIFT spectra of adsorbed CO at 25 °C on the alumina and the CZ-based samples. The spectra were collected after an insitu reduction at 300 °C.

4.1.7 Oxygen Storage Capacity

The OSC was measured to obtain the CZ's capability to store and release O_2. Two types of measurements were performed where O_2 and CO were injected alternately with 5 min or 30 s intervals for OSC and dynamic OSC (DOSC) respectively. It was measured for all samples at 300, 450 and 600 °C in order to relate the (D)OSC to the activity testings performed at temperature ramps between 300-600 °C. The estimated (D)OSC values are presented in Table 4.4. An overall trend was observed for all samples where an increase in temperature led to a decrease in both OSC and DOSC which could be due to the fact that the metal is only partially oxidized at higher temperatures. Unlike CZ, alumina is a non-reducible support as observed in the H_2-TPR profiles (Figure 4.4). Therefore the (D)OCS of the alumina-based samples is only related to the metal's redox properties (Pd/PdO and Rh/Rh_2O_3). Whereas the CZ-based samples exhibited higher (D)OSC/OSC values due to the redox properties of ceria. In the literature, the higher values for the CZ-based samples was suggested to be due to the metal-CZ interface consuming more O_2 because of back-spillover

of O_2 from CZ to the metal which was also suggested by the H_2-TPR profiles in Section 4.1.4 [141][143]. It is also worth noticing that the OSC of Pd-Rh/A is much higher than Pd/A, especially at 300 °C which might be due to the presence of Rh affecting the redox properties of Pd.

Table 4.4: The OSC and DOSC values of all the samples obtained from alternated injections of 1 vol% O_2 and 1 vol% CO at 5 min or 30 s intervals at 300, 450 and 600 °C.

Sample	T	OSC	DOSC
	[°C]	[µmol O_2 g_{cat}^{-1}]	[µmol O_2 g_{cat}^{-1}]
Pd/A	300	186	36
	450	223	31
	600	123	23
Rh/A	300	221	37
	450	168	30
	600	141	27
Pd-Rh/A	300	274	46
	450	210	36
	600	166	28
CZ	300	54	4
	450	211	31
	600	190	28
Rh/CZ	300	325	51
	450	280	45
	600	214	29
Pd-Rh/CZ	300	318	45
	450	225	36
	600	220	28

4.2   Catalytic Activity

4.2.1   Alumina Supported Catalysts

4.2.1.1   Stoichiometric Temperature Ramps

The catalytic activity of Pd/A was first measured under static stoichiometric conditions ($\lambda = 1$) where CH_4 conversion started at 355 °C and 329 °C in the first and second cycles, respectively (Figure 4.8). CH_4 was oxidized by O_2 up to approximately 464 °C (cycle 1) and 438 °C (cycle 2) as seen by the simultaneous increase in the CO_2 and H_2O signals (Figure E.1; Reaction 1.2). At this point, a sudden increase of the CH_4 conversion was observed at the same time as the MS signal of H_2O started decreasing indicating a H_2O consumption by CH_4 following Reaction 1.6. A visible production of H_2 followed shortly after, and as there was no H_2 present in the simulated exhaust gas, the production of H_2 can be explained by CH_4 steam reforming (SR) (Reaction 1.6) and the water-gas-shift (WGS) (Reaction 1.7) [8][31]. At low temperatures there was a low NO conversion of 1 % and 5% for cycle 1 and 2 respectively with an approximately 50 % selectivity for N_2O starting at 440 °C and 407 °C for the first and second cycle respectively. N_2O is known to form by Reaction 1.5 in an oxidizing atmosphere, which was apparent from the amount of O_2 present at these temperatures (Figure E.1) [31]. The concentration of N_2O increased to a maximum of 154 ppm at 459 °C for cycle 1 and 141 ppm at 438 °C for cycle 2 before decreasing and dropping to zero when NH_3 formation started, suggesting that the catalyst is selective for one or the other [26]. However, N_2O was barely observed in the cooling ramp, possibly due to the very sharp decrease of NO conversion at approximately 475 °C. The production of NH_3 started at 469 °C and 448 °C for cycle 1 and 2 respectively due to the H_2 production from the steam reforming of methane following Reaction 1.8. NO reached its maximum conversion at 483 °C (cycle 1) and 468 °C (cycle 2). This was the same temperatures as a net production of H_2 was observed, indicating that NO was also reduced by H_2 to form N_2 by Reaction 1.10. From the temperature ramps over Pd/A, it was apparent that when CH_4-SR occurred, full NO reduction took place, which emphasizes the "interdependence" of NO and CH_4. It is only when CH_4-SR pathway takes place that high conversion of both pollutants is observed as mentioned in Section 1.3.

CH_4-SR was maintained up 600 °C and dropped abruptly at 475 °C in the descending ramps. As a result, the H_2 formation decreased which triggered a sharp decrease in the NO conversion (also observed for the MS signal of H_2O) indicating that the NO conversion is dependent on the H_2 produced from CH_4-SR and WGS which is in turn dependent on the Pd oxidation state. Indeed, the occurrence of CH_4-SR is believed to occur on metallic Pd, due to the intrinsic H_2 formation. Comparing the heating and cooling ramps, a negative hysteresis was observed for both the CH_4 and NO conversion. According to McCarty [150], PdO is thermodynamically stable at low temperatures, but decomposes to Pd^0 at higher temperatures under stoichiometric conditions resulting in a phase transition which leads to the hysteresis during methane oxidation. However,

Pd^0 oxidation occurs at higher temperatures than PdO reduction, explaining the nature of the negative hysteresis observed. Indeed, since high pollutant abatement rates were only achieved when CH4-SR reaction was promoted (over metallic Pd), and if PdO formation in the descending ramp occurred at higher temperatures than PdO reduction in the ascending ramp, the system would collapse in an earlier stage in the descending ramp.
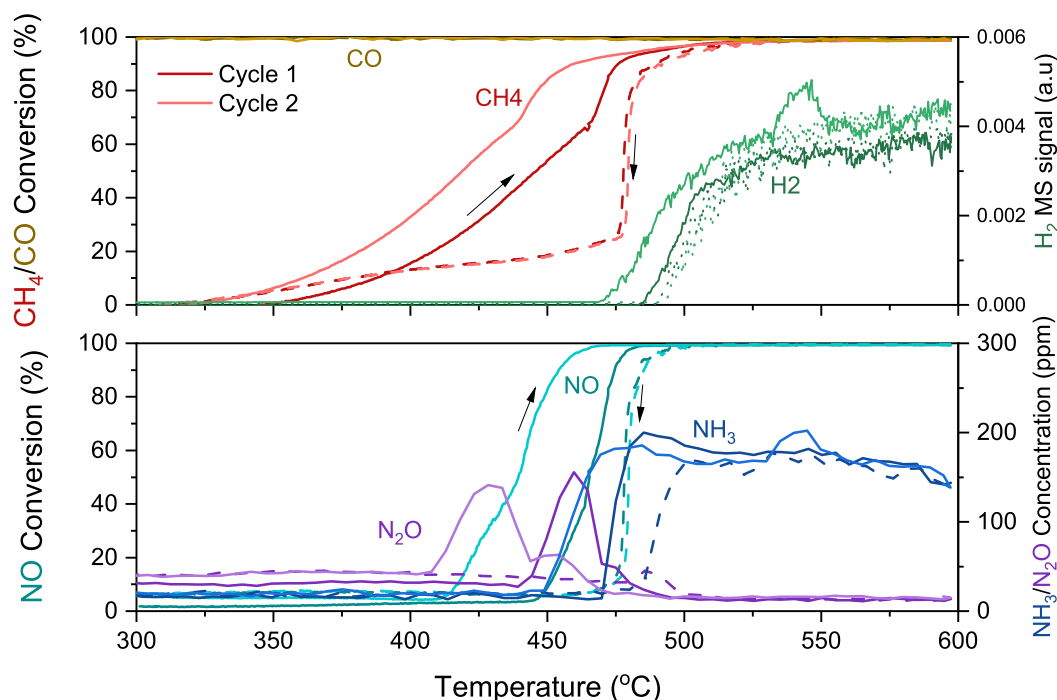
Figure 4.8: CO, CH_4 and NO conversion, H_2 MS signal and NH_3 and N_2O concentrations during two temperature cycles of heating (——) and cooling (- - -) over **Pd/A** under stoichiometric conditions corresponding to 5 vol % H_2O, 0.15 vol% CH_4, 0.16 vol% NO, 0.7 vol% CO and 0.57 vol% O_2 in Ar at a WHSV of 240 L h^{-1} g_{cat}^{-1}. The darker color correspond to the first cycle and the lighter color correspond to the second cycle.

As with Pd/A, temperature ramps under stoichiometric conditions were also measured over Rh/A (Figure 4.9). Light-off temperatures for CH_4 conversion started at approximately 375 °C in first cycle and 400 °C for cycle 2 and 3 which was the same temperature as the increase of H_2O and CO_2 (Figure E.2) suggesting that CH_4 was oxidized by O_2 (Reaction 1.2). The high light-off temperature was possibly due to the stoichiometric conditions and the oxidized pretreatment leaving the Rh particles in the less active oxidized state of Rh_2O_3, which is, according to Twigg et al. [151], formed under hot oxidizing conditions. A maximum CH_4 conversion of 67 % was reached at 600 °C for cycle 1. Since neither a decrease of H_2O signal nor an increase of the H_2 was observed (Figure E.2), it was assumed that CH_4 was only oxidized by O_2 and did not undergo oxidation by

H_2O. As mentioned in Section 1.3.3.2, Rh is known to be highly active for NO reduction which was observed in Figure 4.9, with a 53 % NO conversion at 300 °C in the first cycle over Rh/A. However, this led to a large N_2O production at low temperatures. According to Granger et al. [29], N_2O typically forms at low temperatures on Rh due to adsorption competition between CO, NO and N_2O itself which prevents the re-adsorption of N_2O for further conversion to N_2. At approximately 300 °C the NO reduction reached a selectivity of 33 % for N_2O for the second and third cycles. At the same temperature it was apparent from Figure 4.9 that not all CO had been oxidized and it is possible to suggest a reaction between NO and CO which, according to Na-Ranong et al. [55], provides a higher selectivity for N_2O at low temperatures on Rh. However, the NO reduction seemed to decrease with an increasing temperature. A possible explanation is that the Rh_2O_3 can form interactions with the support as deactivated Rh-alumina species according to Reaction 4.1 [151][67].

$$Rh_2O_3 + Al_2O_3 \longrightarrow Rh_2O_3 \cdot Al_2O_3 \qquad (4.1)$$
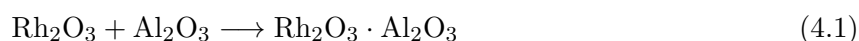
An overall trend is that the conversion decreased for each cycle, where probably more Rh species segregated into the alumina-support during each cycle.
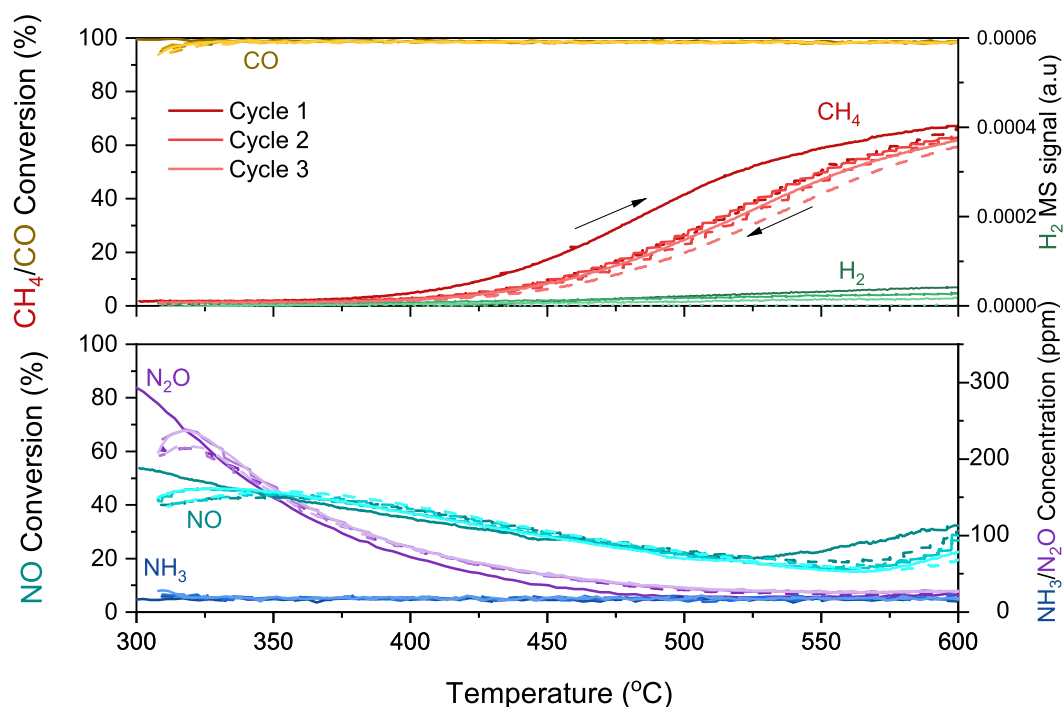
Figure 4.9: CO, CH_4 and NO conversion, H_2 MS signal and NH_3 and N_2O concentration during three temperature cycles of heating (—) and cooling (- - -) cooling over **Rh/A** under stoichiometric conditions corresponding to 5 vol% H_2O, 0.15 vol% CH_4, 0.16 vol% NO, 0.7 vol% CO and 0.57 vol% O_2 in Ar at a WHSV of 240 L h^{-1} g_{cat}^{-1}. The darker color correspond to the first cycle and the lighter colors correspond to the second and third cycle.

The stoichiometric temperature ramps over Pd-Rh/A are presented in Figure 4.10. Similar to Pd/A, CH_4 conversion started at around 350 °C, however the light-off temperature did not change throughout the cycles. The CH_4 conversion increased with temperature through direct CH_4 oxidation by O_2 (Reaction 1.2) proved by the increase of H_2O and CO_2 MS-signal at the same temperatures (Figure E.3). As observed on Rh/A, approximately 15 % NO was already being converted at 300 °C over Pd-Rh/A producing a small amount of N_2O which was probably due to the presence of Rh in the catalyst. However, as seen in Figure 4.10, the NO conversion was negligible at approximately 440 °C and all three cycles had a second light-off temperature at 462 °C, 453 °C and 448 °C for cycle 1,2 and 3 respectively, which were the same temperatures where the increase in CH_4 conversion seemed to stabilize.

Under stoichimetric conditions 100% NO conversion is needed to achieve enough O_2 to oxidize all of the CO and the CH_4, since NO is an O_2 carrier and is therefore taken into account in the λ calculations (Equation 3.6). At 462 °C, the 64.2 % conversion of CH_4 in cycle 1 corresponds to 537 ppm or 1.8 μmol of CH_4 still being present in the system which would need twice the amount of O_2 to fully oxidize. At the same temperature NO conversion was very low and did not give away a lot of O_2, but as mentioned in Section 4.1.7 the Pd-Rh/A can store 36 µmol O_2 g_{cat}^{-1} or 1.8 µmol O_2 at 450 °C which is only related to the Pd/PdO and the Rh/RhO$_2$ system. The stabilized conversion at approximately 460 °C was probably due to CH_4 waiting for NO to release O_2 in order to reach full oxidation, which forces it to use the O_2 stored in the catalyst. This reduced the catalyst to its metallic state, the preferred state for CH_4-SR, which was observed at 544 °C and confirmed by the decrease in the H_2O signal (Figure E.3). This led to a steep increase in both CH_4 and NO conversion (Figure 4.10). Shortly after, the H_2 production was detected at the same temperature as NO reached its maximum conversion at 548, 516 and 512 °C for cycle 1,2 and 3 respectively. Compared to Pd/A, barely any NH_3 was formed when H_2 was produced which is due to ability of Rh to suppress NH_3 formation under rich conditions as mentioned in Section 1.3.3.2.
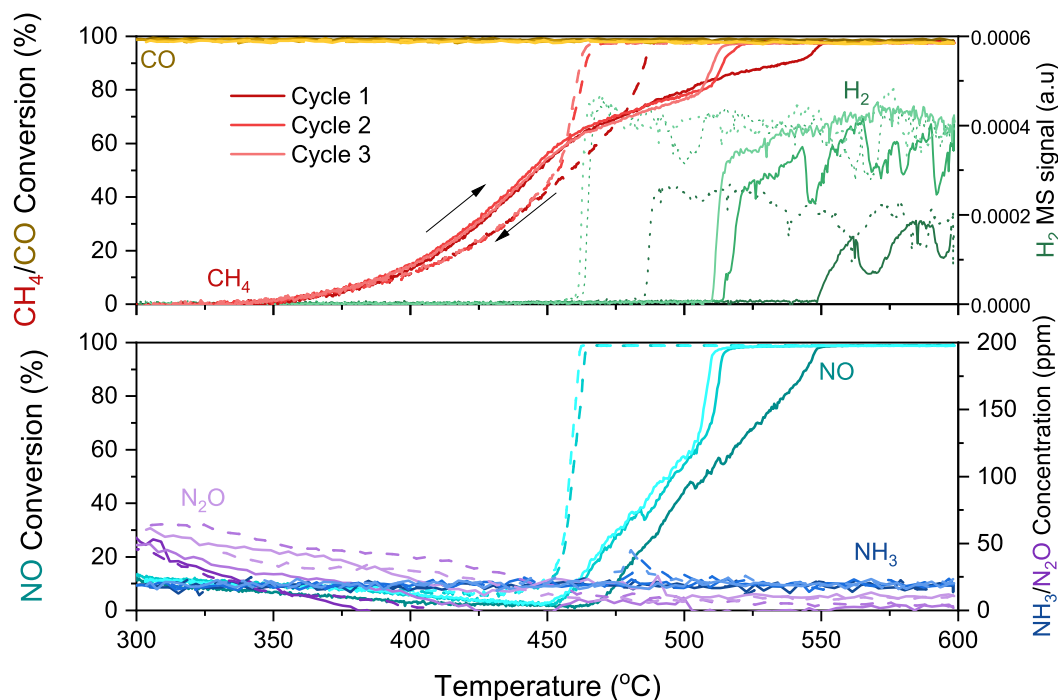
Figure 4.10: CO, CH_4 and NO conversion, H_2 MS signal and NH_3 and N_2O concentration during three temperature cycles of heating (——) and cooling (- - -) over **Pd-Rh/A** under stoichiometric conditions corresponding to 5 vol% H_2O, 0.15 vol% CH_4, 0.16 vol% NO, 0.7 vol% CO and 0.57 vol% O_2 in Ar at a WHSV of 240 L h^{-1} g_{cat}^{-1}. The darker color corresponds to the first cycle and the lighter colors corresponds to the second and third cycle.

In Figure 4.10 there was a clear positive hysteresis between the ramp up and ramp down. As Pd/A produced a negative hysteresis, the positive hysteresis on Pd-Rh/A was most likely due to the presence of Rh. Table 4.5 provides a summary of the light-off temperatures of CH_4, NO and H_2 as well as the temperature when full conversion of CH_4 and NO was reached for all three catalysts. Evident from Table 4.5, Pd/A triggered H_2 production at lower temperatures than Pd-Rh/A, but it is worth noticing that the difference in temperature between a net H_2 production and 100 % CH_4 conversion was less for Pd-Rh/A than Pd/A, possibly due to a faster metal reduction over Pd-Rh/A .

Nevertheless, as summarized in Table 4.5, Pd/A clearly was the best catalyst under stoichiometric conditions regarding the light-off temperature of CH_4 conversion, the temperature for 100 % NO conversion and the triggering of CH_4-SR. From the ramps, Rh seemed to be limited for CH_4 oxidation only and did not reach full conversion of NO (Figure 4.9). Hence, when comparing Pd/A and Pd-Rh/A, as Rh seemed only helpful for NH_3 suppression during the ramp up, the lower Pd

45

content in Pd-Rh/A might be the reason why Pd/A is better. A clear difference between all three catalysts is that the activity of Pd/A and Pd-Rh/A improved for each cycle whereas it got worse over Rh/A. As Rh/A was the only catalyst that did not trigger H_2 production, it is possible that the formation of H_2 enhances the activity of the catalysts through the cycles by making it more reduced.

Table 4.5: A summery of the light-off temperatures of CH_4, NO and H_2 as well as the temperature when reaching 100 % conversion of CH_4 and NO for all three catalysts.

Sample	Cycle	CH4 T °C		NO T °C		H2 T C
		Light-off	100%	Light-off	100%	Light-off
Pd/A	1	355	521	446	483	484
	2	329	521	411	467	470
Rh/A	1	~ 375	-	<300	-	-
	2	~ 400	-	<300	-	-
	3	~ 400	-	<300	-	-
Pd-Rh/A	1	~ 350	551	<300	548	548
	2	~ 350	521	<300	516	513
	3	~ 350	514	<300	512	509

4.2.1.2   Effect of O_2 Dosage in the Feed

Steady state lambda sweeps were conducted to investigate the impact of lambda on the activity and the reactions schemes taking place over the catalysts, as they are greatly affected by the O_2 concentration. Sweeping tests from lean-to-rich ($\lambda = 1.2$ - 0; Figure 4.11a) and rich-to-lean ($\lambda = 0$ - 1.2; Figure 4.11b) were conducted by varying the O_2 dosage in the feed at 420 °C. The temperature was chosen based on a temperature from the stoichiometric temperature ramps were low conversion of NO and CH_4 were achieved.
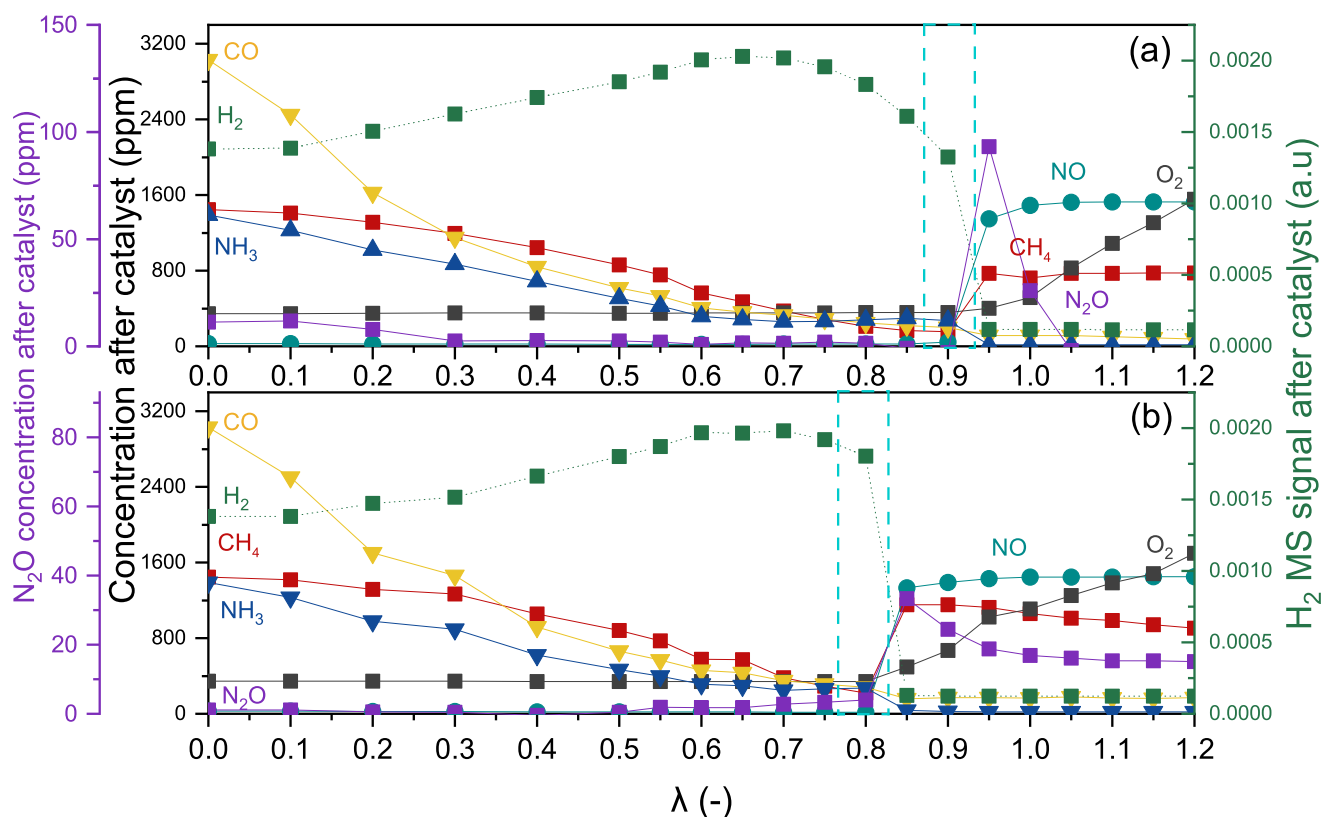
Figure 4.11: The concentration of CO, CH$_4$, NO, O$_2$,NH$_3$, N$_2$O and H$_2$ MS signal after catalyst on **Pd/A** during steady state lambda sweep from (a) lean-to-rich and (b) rich-to-lean at 420 °C.

On the lean side, over PdA (Figure 4.11a), no trace of CO was detected implying that it was fully oxidized by O$_2$ according to Reaction 1.3. A constant concentration of 800 ppm was observed of CH$_4$ corresponding to 53.3 % conversion. Over the lean side Pd was most likely in a more oxidative state promoting the direct oxidation of CH$_4$ by O$_2$. The NO concentration was also found to be quite constant at approximately 1600 ppm (same as the NO feed), but a sudden appearance of N$_2$O was observed at $\lambda = 0.95$ with a small decrease of NO concentration (Figure 4.11a). This N$_2$O peak was in accordance with the stoichiometric temperature ramps in Figure 4.8, where N$_2$O appeared immediately after NO conversion started at approximately the same temperature as the sweeps. However, when lambda reached 0.9 there was a CO-NO crossover point where NO was fully converted and the lowest concentration of CH$_4$ was observed. A breakthrough of H$_2$ and CO formation indicated that the catalyst was most likely reduced and CH$_4$-SR took place as also observed in the temperature ramps under stoichiometric conditions (Figure 4.8). After the crossover point NO was still fully converted and a production of NH$_3$ was detected reaching almost a

100 % selectivity at $\lambda = 0$. However, the increase in CH_4 and CO concentration indicated that even CH_4-SR pathway was sensitive to the O_2 concentration. It seemed that when O_2 was depleted from the reactive environment, the overall CH_4 conversion dropped. The highest concentration of CH_4 was found at $\lambda = 0$ of 1500 ppm indicating that the WGS reaction was producing the H_2 at the very rich conditions which was also the case during the rich-to-lean over Pd/A (Figure 4.11b). The concentrations of all compounds on the rich side were comparable to the corresponding lambdas at the lean-to-rich sweep, but the CO-NO crossover point was reached at $\lambda = 0.8$ instead of 0.9 resulting in a negative hysteresis.

Steady state lambda sweeps were also performed over Rh/A to investigate the optimized lambda for best NO and CH_4 conversion at 420 °C (Figure 4.12). On the lean side of the lean-to-rich sweep (Figure 4.12a), no CH_4 conversion was observed which was consistent with the conversion observed under stoichiometric temperature ramps where little or no CH_4 was converted (Figure 4.9). The NO concentration however, seemed to decrease with the decreasing lambda which is in accordance with NO reduction preferring a more reduced catalyst. The NO conversion seemed to have a selectivity of approximately 10 % towards N_2O formation which is consistent with Rh promoting N_2O under lean conditions as mentioned in Section 1.3.3.2. The CO-NO crossover point was found at $\lambda = 0.6$ detected by the breakthrough of H_2 and CO and the low concentration of CH_4 and NO (Figure 4.9a), indicating that the catalyst was most likely in a reduced state. After the CO-NO crossover point, Rh/A showed similar tendencies to Pd/A (Figure 4.11) where NO was still fully converted whereas CO and CH_4 concentration started to increase and a production of H_2 and NH_3 was observed. However, the NO and CH_4 concentrations were lower implying that a reduced Rh catalyst is more active than a reduced Pd catalyst. Furthermore, the decrease of NH_3 formation over Rh/A was due to the ability of Rh ability to suppress the formation NH_3 as mentioned in Section 1.3.3.2. At $\lambda = 0$, both CO and CH_4 were being converted suggesting that both were active in the H_2 production.
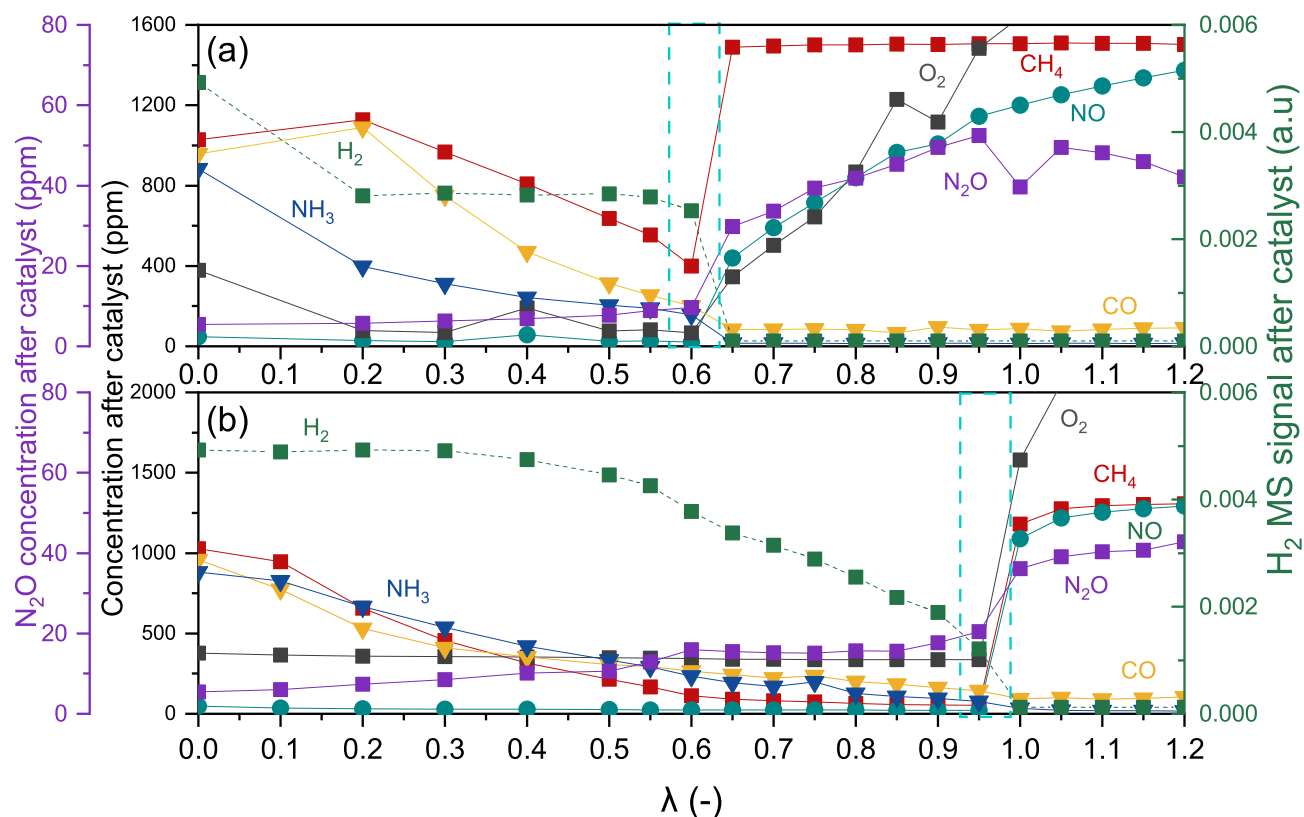
Figure 4.12: The concentration of CO, CH$_4$, NO, O$_2$, NH$_3$, N$_2$O and H$_2$ MS signal after catalyst on **Rh/A** during steady state lambda sweep from (a) lean-to-rich and (b) rich-to-lean at 420 °C.

Looking at rich-to-lean sweep over Rh/A (Figure 4.12b), the concentrations were similar to the lean-to-rich sweep, but the CO-NO cross-over point was shifted to $\lambda = 0.95$ creating a positive hysteresis indicating that Rh stays longer reduced in a net reducing environment [152]. The immediate increase in NO and CH$_4$ concentration is directly related to the change of a reduced to an oxidized surface on the catalyst due to the breakthrough of O$_2$. After the cross-over point, the O$_2$ concentration increased rapidly along with the concentration of CH$_4$ and NO. It is clear that Rh in reduced state is more active towards CH$_4$ and NO conversion.

Lambda sweeps were also conducted over Pd-Rh/A at 420 °C (Figure 4.13). On the lean side of the lean-to-rich sweep (Figure 4.13a), a low NO conversion accompanied by N$_2$O formation by Reaction 1.5 was already detected at $\lambda = 1.2$ which increased towards the CO-NO crossover point. The CH$_4$ concentration showed a similar trend as Pd/A which was attributed to oxidation by O$_2$ by Reaction 1.2. The CO-NO crossover point was found at $\lambda = 0.75$, whereas going towards richer conditions the concentration of CO, CH$_4$ and NH$_3$ increased as observed over Pd/A (Figure 4.11)

and Rh/A (Figure 4.12) as well. However, these concentrations were higher than Rh/A and lower than Pd/A which indicates that reduced Rh is more active towards CH_4-SR and WGS than Pd which was also apparent from the high H_2 signal over Rh/A and Pd-Rh/A compared to Pd/A. The concentrations observed going from rich-to-lean (Figure 4.13b) were very similar as the rich side in Figure 4.13a, but the CO-NO crossover point was found at a higher λ of 0.9 creating a positive hysteresis. After the CO-NO crossover point on the lean side the CH_4 and NO concentrations were constant.
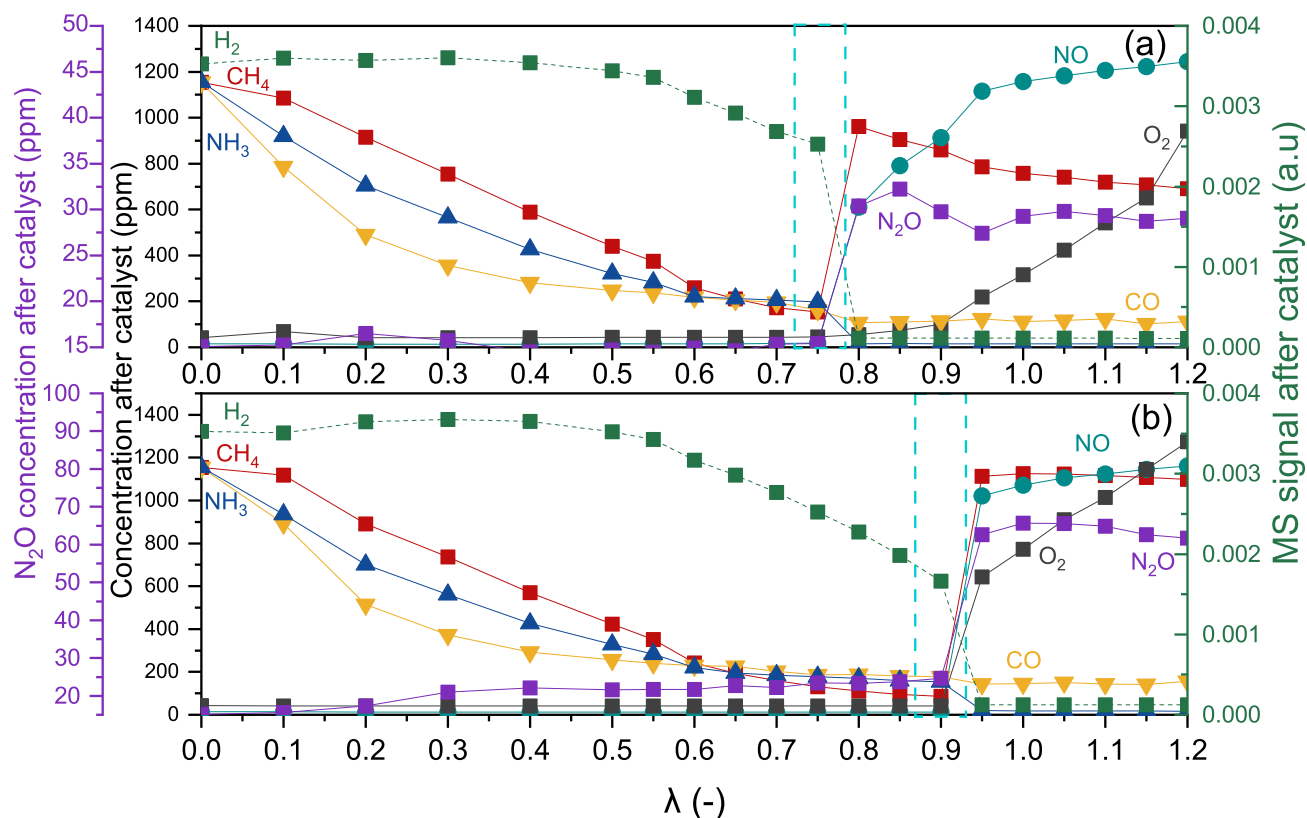
Figure 4.13: The concentration of CO, CH_4, NO, O_2,NH_3, N_2O and H_2 MS signal after catalyst on **Pd-Rh/A** during steady state lambda sweep from (a) lean-to-rich and (b) rich-to-lean at 420 °C.

Hysteresis effects were found for all three catalysts which was caused by phase changes that occur on the surface of Pd and Rh during the sweeps [153]. A positive hysteresis effect was discovered for Rh/A and Pd-Rh/A versus a negative effect on Pd/A, suggesting that the positive hysteresis is due to the presence of Rh and is promoting a wider lambda window of activity [154]. The crossover points shifted from leaner lambda in the order: Pd/A (0.9) > Pd-Rh/A (0.75) > Rh/A (0.6) which was probably due to a higher CH_4 oxidation activity observed in the same order on the lean side

consuming more O_2 and reducing the catalyst more easily [26]. Each catalyst achieved 100 % NO conversion once the catalyst was reduced, which is confirming the results of Gong et al. [26], stating that the NO conversion is directly related to the oxidation state of the catalyst based on their lambda sweeps on a commercial Pd-based TWC at different temperatures. The CH_4 conversion was also dependent on the oxidation state, but other factors such as the O_2 concentration, phase changes and the exposure history of the catalyst might also affect the CH_4 conversion.

4.2.1.3   The Effect of reduction pretreatment

From the lambda sweeps conducted on the catalysts it was discovered that the CO-NO crossover points were found at richer conditions where the catalyst was more reduced. Furthermore, it was clear that Rh seemed to be effective only when fully reduced. Stoichiometric temperature ramps after a reducing pretreatment was therefore performed to investigate if a prereduced catalyst enhanced activity. Additionally, it has also been reported that a reduction pretreatment on a Pd-based catalyst result in better CH_4 conversion at lower temperatures [155][13][156][157] as well as for Rh[158]. Figure 4.14 and 4.15 compare the results from the last cycle of the temperature ramps under stoichiometric conditions of the oxidation and reduction pretreatment considering CO, CH_4 conversion and H_2 MS signal (Figure 4.14) as well as NO conversion and NH_3 and N_2O concentration (Figure 4.15) respectively for all catalysts. The full activity of all cycles can be found in Appendix F for all catalysts.
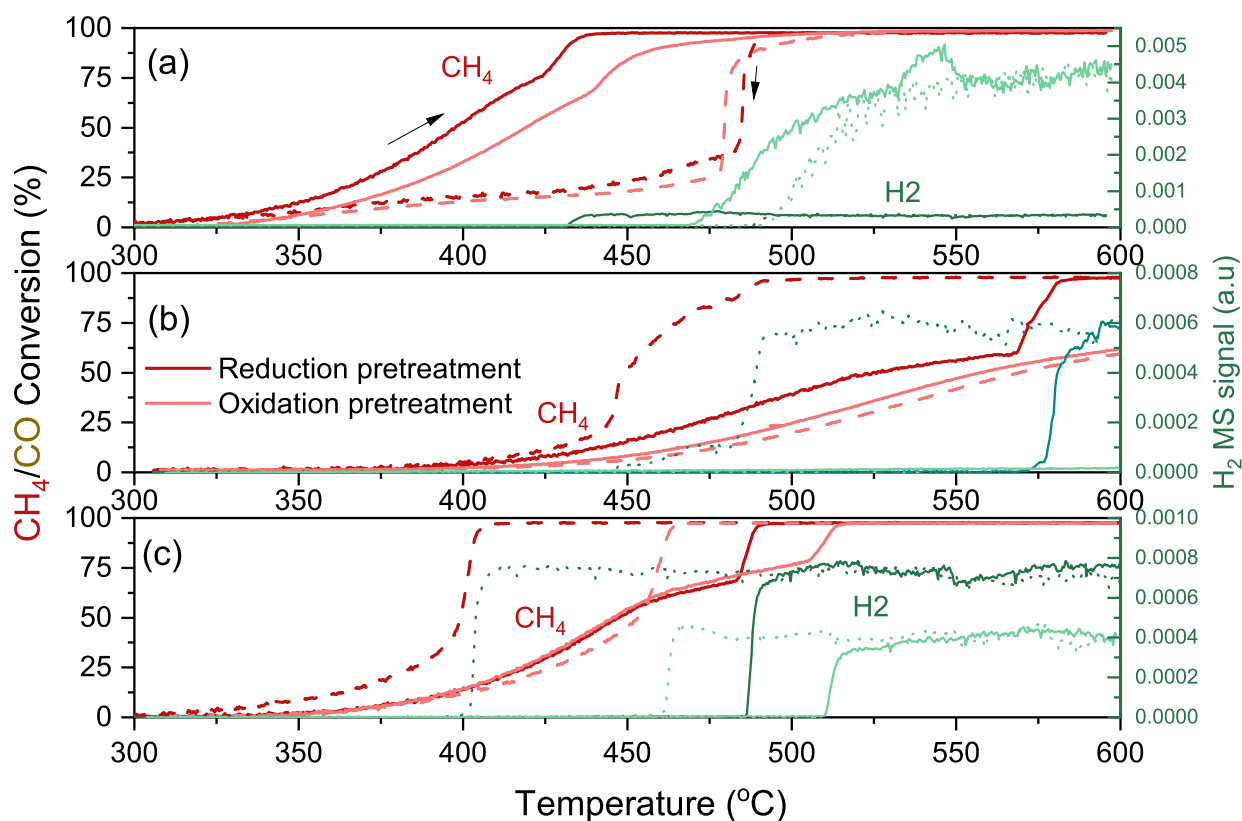
Figure 4.14: The CO and CH_4 conversion and the H_2 MS signal during the last cycle of temperature at λ = 1 on (a) **Pd/A**, (b) **Rh/A** and (c) **Pd-Rh/A** after reduction (dark colors) and oxidation (bright colors) pretreatments
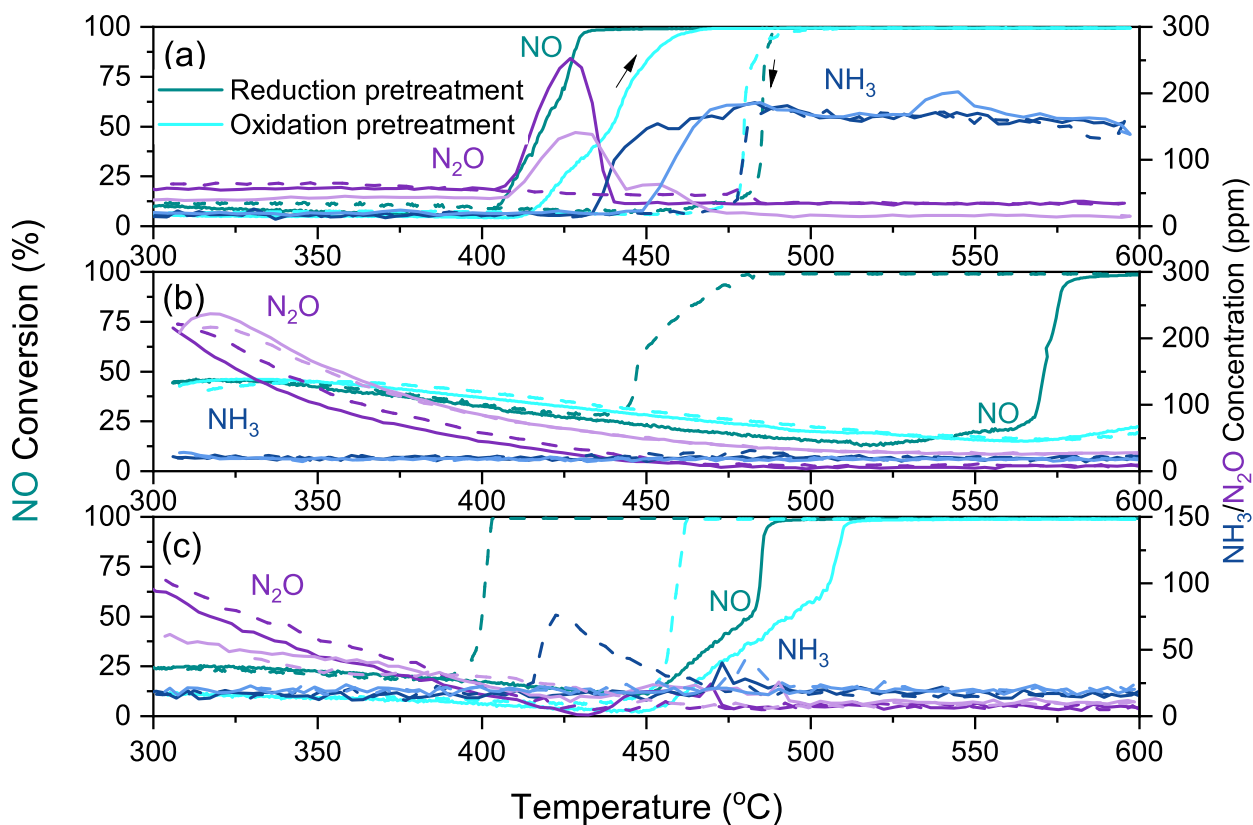
Figure 4.15: NO (turquoise) conversion and NH_3 and N_2O concentration during the last cycle of temperature ramps at $\lambda = 1$ on (a) **Pd/A**, (b) **Rh/A** and (c) **Pd-Rh/A** after reduction (dark colors) and oxidation (bright colors) pretreatments.

It is very apparent that the reduction pretreatment enhanced both NO and CH_4 conversion for all catalysts in Figure 4.14 and 4.15. For Pd/A (Figure 4.14a) the light-off temperature of CH_4 conversion decreased from 329 °C to 307 °C when prereduced. According to Wang et al. [155], the water inhibition effect observed on Pd-based catalyst due to the formation of OH groups on the surface, which would block the active sites for CH_4 [159], is negligible on a prereduced Pd catalyst. This could explain the improvement of activity as well as a higher amount of Pd metal particles being present [160]. The maximum conversion of CH_4 of 98 % was already reached at 438 °C compared to Rh/A at 587 °C and Pd-Rh/A at 483 °C. Moreover, a major improvement was observed in Figure 4.14b for Rh/A when exposed to a reduction pretreatment. The light-off temperature of CH_4 conversion was similar, but unlike the preoxidized sample, CH_4-SR was triggered at 568 °C, which in turn induced full pollutant abatement. This also resulted in a positive hysteresis in the descending ramp, unlike Pd/A which had a negative hysteresis. Similar to Rh/A, the CH_4 conversion over prereduced Pd-Rh/A (Figure 4.14c) seemed to follow the same

curve as the preoxidized Pd-Rh/A until 483 °C, when the conversion rapidly increased followed by H_2 formation. As in the case of the preoxidized sample, the descending ramp resulted in a positive hysteresis, but the high conversion was held for lower temperatures which was also observed for the NO conversion leading to a wider hysteresis.

The NO conversion over prereduced Pd/A also resulted in a lower light-off temperature of 403 °C, but a higher concentration of N_2O was observed which decreased rapidly once H_2 formation was present. NH_3 formation was detected on Pd/A in accordance with the H_2 production, whereas no and small amounts of NH_3 was observed on Rh/A and Pd-Rh/A respectively due to Rh's ability to suppress the NH_3. A positive hysteresis was also observed for the NO conversion over Rh/A, which, after a sharp increase, reached its maximum conversion of 98.6% at 588 °C shortly after the H_2 formation was observed. The 50 % NO conversion at 300 °C of both preoxidized and prereduced Rh/A led to similar amounts of N_2O, which was also observed for Pd-Rh/A but in less amounts due to a lower NO conversion at this temperature. Similar to the CH_4 conversion over preoxidized Pd-Rh/A, the prereduced sample led to a lower temperature for both the light-off and maximum conversion of NO.

As observed in Figure 4.9 the activity of Rh/A decreased for each cycle, but when Rh/A had been exposed to a reduction pretreatment the activity was clearly increasing with each temperature cycle as seen in Figure F.2. This strengthen the hypothesis from Section 4.2.1.1, that the triggering of CH_4-SR and H_2 formation enhances the activity of the catalysts. According to Yao et al. [67], the average oxidation state of Rh is Rh^{3+} which is present as Rh_2O_3 under oxidizing conditions, such as after the oxidation pretreatment. From Figure 4.9 it is apparent that Rh_2O_3 is not active towards CH_4 conversion where a limited CH_4 and NO conversion was detected. However, after reduction there was a sharp increase for both CH_4 and NO conversion resulting in a positive hysteresis possibly due to Rh keeping the reduced state longer. A possible explanation for the improved activity can be that, as mentioned in Section 4.2.1.1, the Rh_2O_3 forms weak interactions with the support according to Reaction 4.1. However, this metal-support interaction can reduce rapidly to active metal Rh when the conditions turn slightly reducing according to Reaction 4.2 [151].

$$Rh_2O_3 \cdot Al_2O_3 + 3H_2 \longrightarrow 2Rh + Al_2O_3 + 3H_2O \qquad (4.2)$$
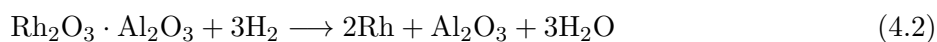
From both preoxidized and prereduced Pd/A it is possible to assume that the CH_4 oxidation at lower temperatures consumes O_2 and slowly reduces PdO to Pd^0 which triggers NO conversion as it starts converting at higher temperatures. Once all O_2 is consumed, Pd is considered as fully reduced Pd^0, which triggers the CH_4-SR and NO reduction. However, a negative hysteresis has been observed over all preoxidized Pd/A, prereduced Pd/A and during the lambda sweeps indicating that Pd tends to be oxidized rather than reduced and PdO forms at higher temperatures creating

the negative hysteresis.

As mentioned in Section 4.2.1.1 Pd is the main active component in the preoxidized Pd-Rh/A at lower temperatures until CH_4-SR is triggered. It is believed that during the temperature ramps performed over the preoxidised sample, Rh was activated through its reduction only once H_2 formation was induced from the CH_4-SR reaction. When H_2 was produced in situ, it seemed that the reduced Rh species allowed to maintain Pd reduced longer which therefore led to a positive hysteresis. When the reduction preteatment was performed, due to the higher amount of H_2 flow over the catalyst (2 vol%) the Rh species were most probably more reduced, which led to stronger andenhanced interaction between Rh (reduced) and Pd species. This would explain why after a reduction pretreatment, the positive hysteresis was wider than when the catalyst was reduced by the in situ H_2 formation. The fact the the reduction pretreatment enhanced the activity of Rh is emphasized by the results achieved over the Rh/A samples. After reducing pretreatment, it is possible to trigger CH_4-SR and NO reduction reactions (hence, reduction of Rh). Then, the in situ H_2 formation appeared to maintain Rh reduced longer as observed from the positive hysteresis. This would show that, indeed, the in situ H_2 formed did play an important role in maintaining the Rh species active. (Figure 4.14c and 4.15c).

As already suggested through CO-DRIFT in Section 4.1.6 there is a possibility of synergy between Pd and Rh in Pd-Rh/A. According to Hu et al. [64], who studied the synergic effect on a Pt-Rh TWC, Reaction 4.2 takes place at lower temperatures (<560 K) on a bimetallic Pt-Rh catalyst compared to a Rh catalyst alone. On the other hand, Vedyagin et al. [161], stated that a Pd-Rh alloy prevented the Rh to interact with the support. In both studies, however, the synergy between Pd and Rh prevents deactivation of Rh. This is apparent from the sharp increase in CH_4 and NO conversion, most likely due to reduced active Rh metals, which takes place at lower temperatures over Pd-Rh/A than over prereduced Rh/A.

4.2.1.4   The effect of Rh in Pd-Rh/A

From the stoichiometric activity ramps and the lambda sweeps a positive hysteresis was only observed on Rh/A and Pd-Rh/A indicating an effect of Rh on Pd as Pd/A alone resulted in a negative hysteresis. From the discussion above, it is understood that reduced Rh species seem to play an important role in the reaction scheme and reactivity of Pd. Three hypothesis arose such as does Rh keep Pd reduced at lower temperatures? Does Rh make Pd oxidize more easily? Or is the positive hysteresis only due to Rh alone?

In order to answer these questions in situ XRD was conducted on Pd/A, Pd-Rh/A and a mechanical mix of Pd/A and Rh/A (Pd/A_Rh/A) while keeping the Pd:Rh ratio at 3:2. The patterns were collected during a heating ramp (RT - 600 °C) while the sample was exposed to H_2 (Figure 4.16), followed by a cooling ramp (600 - 300 °C) in O_2 (Figure 4.17) as to mimic the temperature ramps

during activity.Because Rh was not detected in the XRD patterns (Figure 4.1), only the Pd/PdO system was investigated in this experiment.

As mentioned in Section 4.1.2, the most intense peak for PdO is located at 33.9 °. In Figure 4.16a and 4.16c the PdO peaks were clearly detected for Pd/A and Pd/A_Rh/A at 60 °C during the heating ramp in reduced atmosphere. Moving to higher temperatures, the peak disappeared which proved that the samples were fully reduced between 60 - 170 °C which was also clear by the appearance of a peak at 39.4 °indicating the presence of Pd^0. However, Pd-Rh/A seemed to already be reduced before the first XRD pattern was collected as only the peak corresponding to Pd^0 was observed for all temperatures (Figure 4.16b), which points toward Rh promoting reduction of Pd.
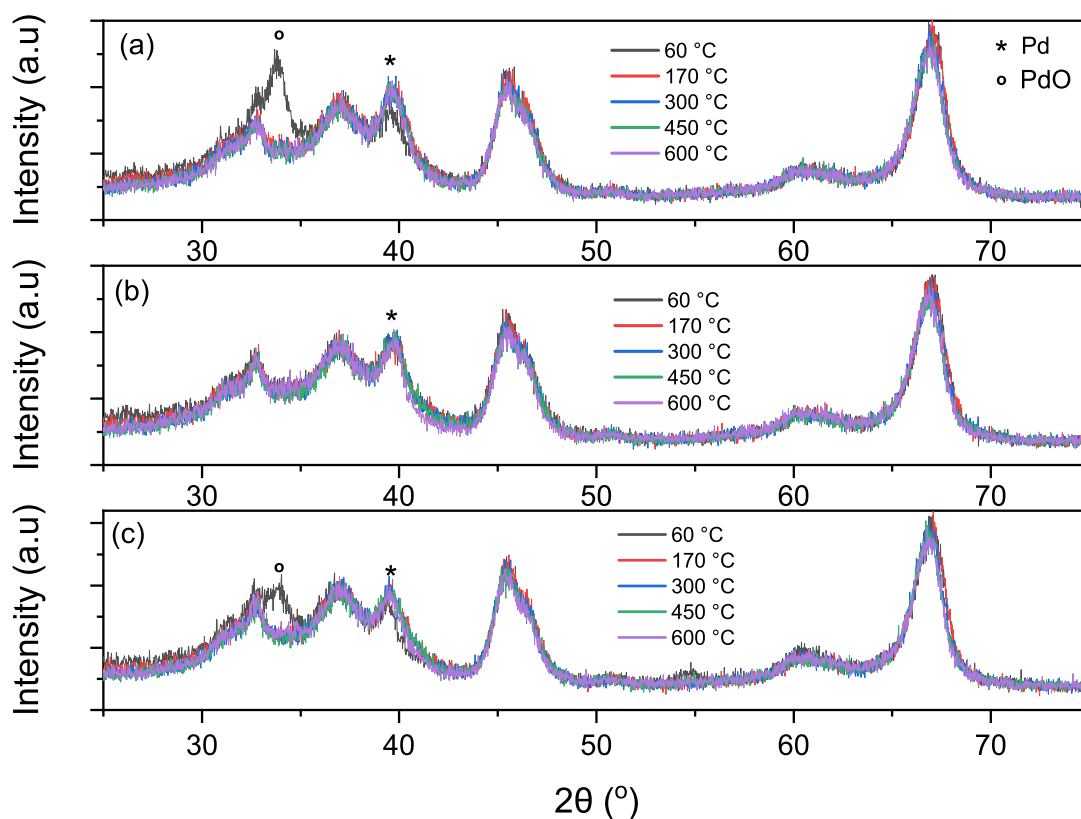
Figure 4.16: Powder in situ XRD patterns collected during a heating ramp at different temperatures while being exposed to 2 vol% H_2 in N_2 for (a) **Pd/A**, (b) **Pd-Rh/A** and (c) **Pd/A_Rh/A**.

During the cooling ramp in O_2, Pd/A and Pd/A_Rh/A again showed similar results where the peak of PdO (33.9 °) started to appear at around 475 °C (Figure 4.17a and 4.17c). On Pd-Rh/A however, the PdO peak appeared at 500 °C. The higher temperature for the oxidation of Pd^0 on

Pd-Rh/A indicates a promotion of oxidation on Pd.
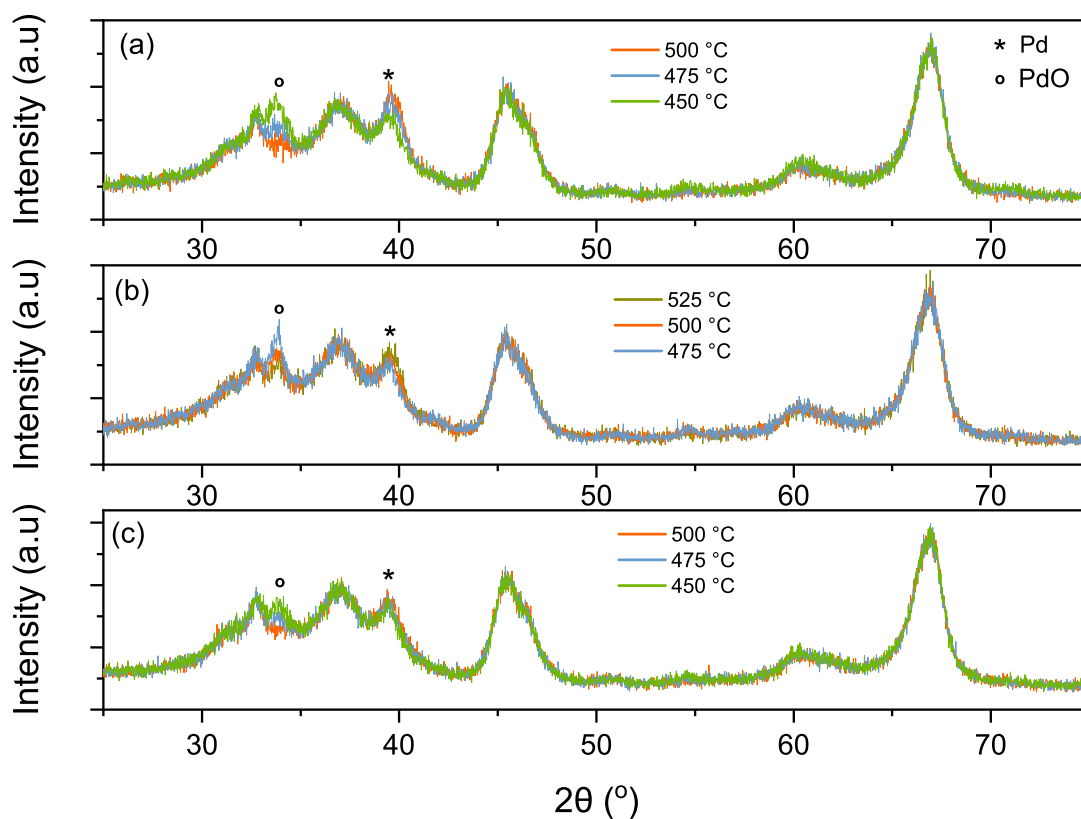
Figure 4.17: Powder in situ XRD patterns collected during a cooling ramp after reduction at different temperatures while being exposed to 2 vol% O_2 in N_2 for (a) **Pd/A**, (b) **Pd-Rh/A** and (c) **Pd/A_Rh/A**.

From both temperature ramps, Pd/A and Pd/A_Rh/A reduced and oxidized at the same temperature as was expected since Pd/A_Rh/A was only physically mixed (so no close contact between Pd and Rh). As this was observed at different temperatures for Pd-Rh/A, where it reduced at lower temperatures and oxidized at higher temperatures than Pd/A and Pd/A_Rh/A, it was clear that Rh enhanced the redox properties of Pd. This likely suggests an intimate contact of Pd and Rh, maybe a formation of an alloy in the Pd-Rh/A sample. Another indication of a synergic effect between Pd and Rh was obtained by performing a temperature ramp on the prereduced Pd/A_Rh/A (Figure 4.18).
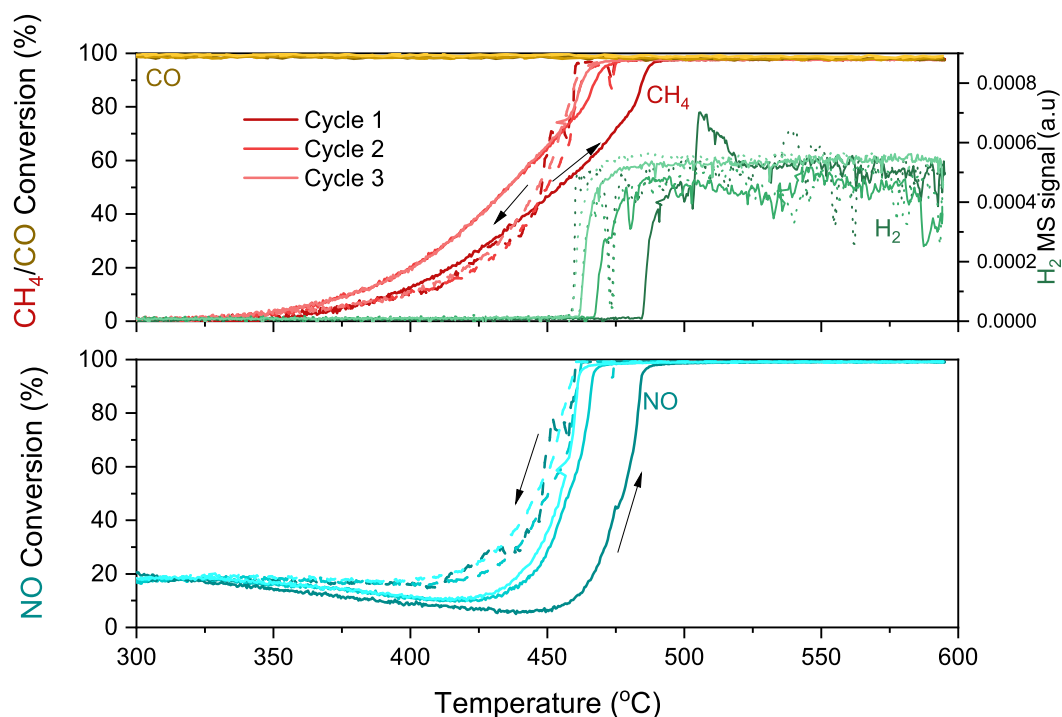
Figure 4.18: CO, CH$_4$ and NO conversion, H$_2$ MS signal and NH$_3$ and N$_2$O concentration during three temperature cycles of heating (——) and cooling (- - -) cooling over **Pd/A__Rh/A** under stoichiometric conditions corresponding to 5 vol% H$_2$O, 0.15 vol% CH$_4$, 0.16 vol% NO, 0.7 vol% CO and 0.57 vol% O$_2$ in Ar at a WHSV of 240 L h^{-1} g$_{cat}^{-1}$, after reduction pretreatment. The darker colors correspond to the first cycle and the lighter colors correspond to the second and third cycle.

Comparing the temperature ramps over Pd/A__Rh/A with prereduced Pd-Rh/A (Figure 4.14c and 4.15c) it was apparent that these were two different catalysts and that a mechanical mix of Pd and Rh is different than a chemical mix. From the results of in situ XRD, CO-DRIFT and the temperature ramp over Pd/A__Rh/A it is possible to suggest that the Pd and Rh particles on Pd-Rh/A are located closely on the alumina support influencing each others electron density. Unfortunately it was not possible to conduct an EDX map to fully confirm this statement, as the K-edge of Pd and Rh are too close in energy, and therefore indistinguishable. A possible solution would be to perform electron energy-loss spectroscopy (EELS) which can provide a better identification of Rh and Pd [162].

From the in situ XRD it appeared that Rh promoted the redox properties of Pd. However, it was not possible to directly compare the in situ XRD with the activity ramps as the conditions are different. During the activity ramps there was no H$_2$ in the feed, and the reducing agents were CH$_4$ and CO. However there was O$_2$ present in the feed, but in a concentration of 0.57 vol% compared

to the 2 vol% O_2 used in the in situ XRD experiments, which was due to the limit of the mass flow controllers. As to further investigate the reason for the positive hysteresis observed in Pd-Rh/A ex situ XAS was performed on the following samples summarized in Table 4.6. The samples measured after activity were frozen at 425 °C during the cooling ramp in order to obtain information about the oxidation states of the metals during the hysteresis. The samples that were only pretreated was also frozen, but at 300 °C.

Table 4.6: XAS measured samples, their corresponding sample code and the edge that was measured. [1] represents the samples that were frozen in Argon at 425 °C during cool down to room temperature and [2] corresponds to samples frozen at 300 °C.

Sample	Sample code	Edge
Pd foil	Pd-red	Pd
Rh foil	Rh-red	Rh
Pd/A as it is	Pd/A-fresh	Pd
Rh/A as it is	Rh/A-fresh	Rh
Pd-Rh/A as it is	Pd-Rh/A-fresh	Pd, Rh
Pd/A prereduced [2]	Pd/A-H2 PT	Pd
Rh/A prereduced [2]	Rh/A-H2 PT	Rh
Rh/A preoxidized [2]	Rh/A-O2 PT	Rh
Pd/A activity after prereduction [1]	Pd/A act-H2 PT	Pd
Pd-Rh/A activity after prereduction [1]	Pd-Rh/A-act-H2 PT	Pd, Rh
Pd-Rh/A activity after preoxidation [1]	Pd-Rh/A-act-O2 PT	Pd, Rh

Figure 4.19 and 4.20 shows the XANES region of the XAS spectra represented at the Pd K-edge and the Rh K-edge and provides information about the oxidation state as mentioned in Section 2.2.8. As a reference, the spectra of the Pd and Rh foils were plotted. After calcination in air, Pd/A-fresh and Pd-Rh/A-fresh were seen to be fully oxidised, as observed from the XANES shape and the white line which was shifted to higher energy when compared to the Pd reference foil Figure 4.19. On the other hand, Rh appeared to be more oxidized after an oxidation pretreatment was applied than after calcination in air at 550 °C (though in the latter case, the Rh species were still mainly oxidised). The Rh oxidation state was seen to be similar after calcination for both samples, Rh/A-fresh and Pd-Rh/A-fresh as confirmed in the insert of Figure 4.20. As mentioned previously in Section 4.2.1.3 a major improvement in activity over prereduced Rh/A compared to Rh/A-O_2

PT was observed (Figure 4.14b and 4.15b). If more active Rh metal is present at the start of the temperature ramp, it is possibly easier to trigger the fully reduced state at lower temperatures [160]. Hence, the ex-situ XAS confirmed that indeed, after a reducing pretreatment,the Rh species were fully reduced. The Pd in Pd-Rh/A-act-O_2 PT and Pd-Rh/A-act-H_2 PT seemed to be equally reduced as Pd in Pd/A-H_2 PT (Figure 4.19). Looking at the insert of Figure 4.19 the three samples seemed to be aligned with Pd-red and are therefore considered as fully reduced Pd-samples. Both Pd-Rh/A-act-O_2 PT and Pd-Rh/A-act-H_2 PT were frozen at 425 °C which from the catalytic results (Figure F.8 and F.7) were found to be in the high abatement rate regime (full NO, and CH_4 conversion, while CH_4-SR was taking place). Hence, these results confirm that when CH_4-SR reaction pathway was taking place, and all pollutants were converted, the Pd species were fully reduced.

Looking at the Rh K-edge for the same samples (Figure 4.20), Rh was partially reduced in both samples, but Rh in Pd-Rh/A-act-H_2 PT had a higher degree of reduction which was clear from both the shift of the white line and the XANES shape. Pd/A-act-H_2 PT was also frozen at 425 °C corresponding to the end of its hysteresis (Figure 4.14a and 4.15a). By examining the Pd K-edge XANES spectra (Figure 4.19), the Pd in Pd/A-act-H_2 PT seemed to be partially oxidized which implies that as soon as the activity towards CH_4 and NO dropped and CH_4-SR vanished, the catalyst was not fully reduced anymore. This confirms that the high activity regime collapses as soon as the Pd species reoxidize. Comparing with the results (both catalytic and spectroscopic) achieved over Pd-Rh/A-act-O_2 PT indicates that when only Pd is present it oxidizes at higher temperatures in the cooling ramp compared to Pd-Rh/A. From the XANES spectra it is clear that the presence of reduced Pd is crucial to achieve high pollutant abatement rates (due to the promotion of CH_4-SR), while the presence of reduced Rh (which is enhanced by a reduction pretreatment) allows to keep the metallic Pd species for longer time (lower temperatures). The second statement was further emphasized by the in situ XRD results as it was clear that Pd reduced at lower temperatures in Pd-Rh/A than Pd/A and Pd/A_Rh/A and that Rh interferes with the redox properties of Pd.
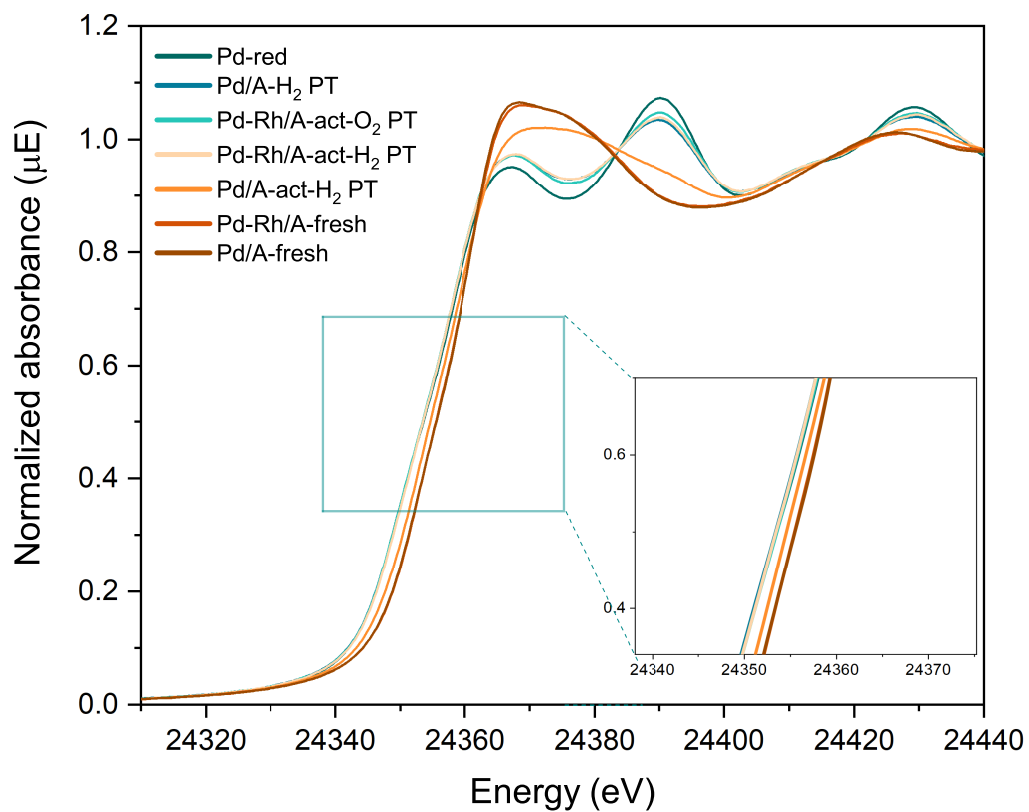
Figure 4.19: Ex-situ fluorescence Pd K-edge XAS spectra of samples described in Table 4.6.
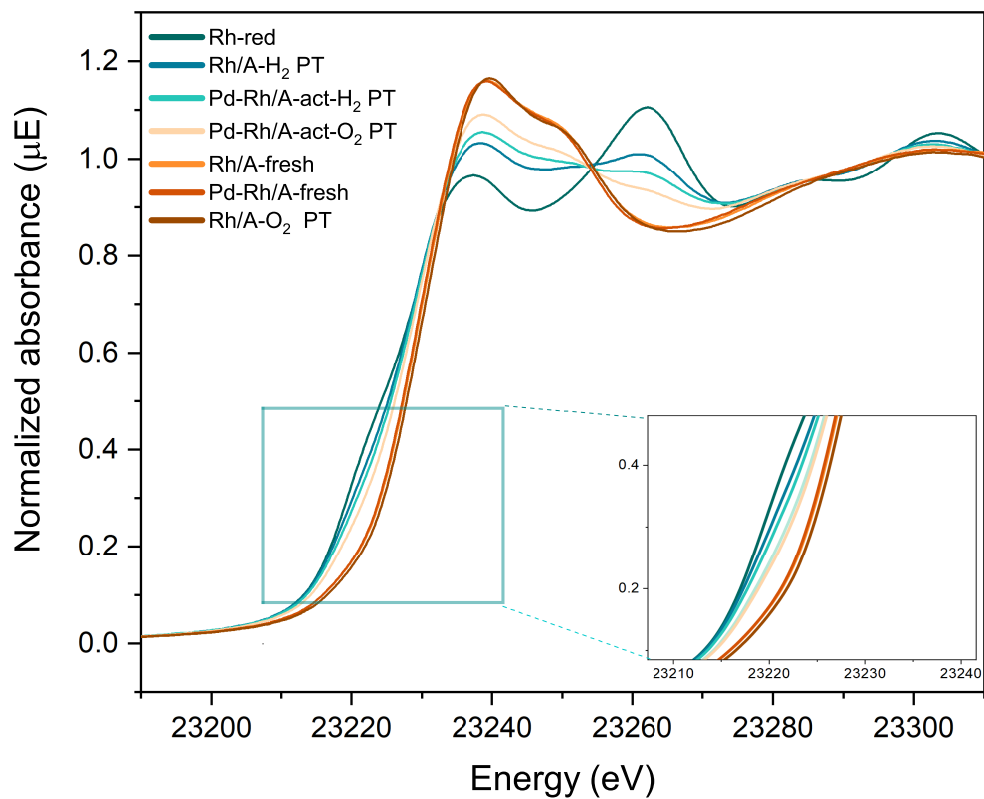
Figure 4.20: Ex-situ fluorescence Rh K-edge XAS spectra of samples described in Table 4.6.

4.2.1.5 O2 Dithering Optimization

In real TWC operation the engine oscillates between rich and lean conditions at different frequencies. As mentioned in Section 1.3.2 studies have shown that a varying O_2 feed improves the catalytic activity especially with respect to CH_4 conversion. In order to find the optimized parameters for CH_4 conversion, steady state experiments at 420 °C with a varying O_2 amplitude around stoichiometric conditions, $\lambda = 1\pm$ A, at different frequencies were carried out where A is the amplitude. The results are presented in Figure 4.21, 4.22 and 4.23 for Pd/A, Rh/A and Pd-Rh/A respectively.

The conversion of NO and CH_4 showed the same dependence on the dithering conditions for all three catalysts, which suggests that CH_4 and NO conversion are closely related to each other under realistic driving conditions [26]. The amplitude of the dithering seemed to have more impact on the CH_4 and NO conversion than the frequency especially on Rh/A and Pd-Rh/A (Figure 4.22 and 4.23). The lower the amplitude, the lower the conversion of CH_4 and NO. This is due to a lower fraction of reduced noble metal, which is the favorable state for the CH_4-SR and NO conversion [155] [52]. The dithering frequencies appeared to affect the conversions on Pd/A more than Rh/A and Pd-Rh/A especially at higher amplitudes, possibly due to Rh^0 promoting the NO reduction and CH_4-SR in more varying conditions than Pd.

Rh/A and Pd-Rh/A showed similar dependence on the O_2 dithering frequencies, but a higher amplitude was necessary for the reduction of Rh/A. This implied that it is harder to reduce Rh alone, which is consistent with the results of the activity under stoichiometric conditions on Rh/A (Figure 4.9) and the lambda sweep (Figure 4.12).

The CO conversions were > 96% for all catalysts. Higher amplitudes at lower frequencies increased the CO conversion, which was the opposite case for the NO and CH_4 conversion. As an oxidized catalyst is preferred for the CO oxidation, it seems like a lower frequency keeps the catalyst more oxidized (Figure 4.21f) or does not produce H_2 at all as observed in Figure 4.21f, 4.22f and 4.23f. However, it is also possible that the CO observed at the higher frequencies is due to the promotion of CH_4 partial oxidation or sCH_4-SR [26].

High NH_3 concentration was observed at the higher amplitudes for all catalysts, being the highest for Pd/A, due to the H_2 formation from CH_4-SR and the WGS. On the contrary, the N_2O concentration decreased at higher amplitudes as a result of the selectivity of NO conversion changing to NH_3 at reducing conditions [26].
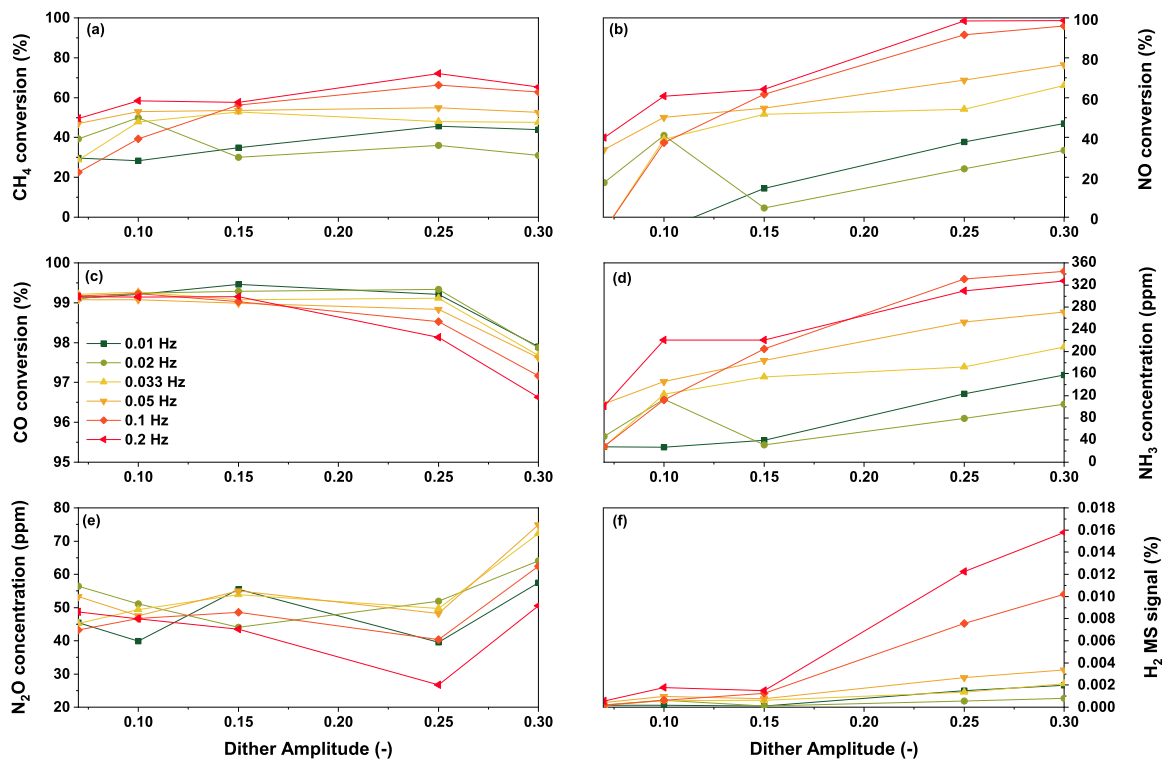
Figure 4.21: (a) CH_4, (b) NO and (c) CO conversion, (d) NH_3 and (e) N_2O concentration and (f) H_2 MS signal during O_2 dithering with different dithering amplitudes varied from $\lambda = 1\pm$ 0.07 to $\lambda = 1\pm$ 0.30 and different dithering frequencies from 0.001 Hz to 0.2 Hz on **Pd/A**.
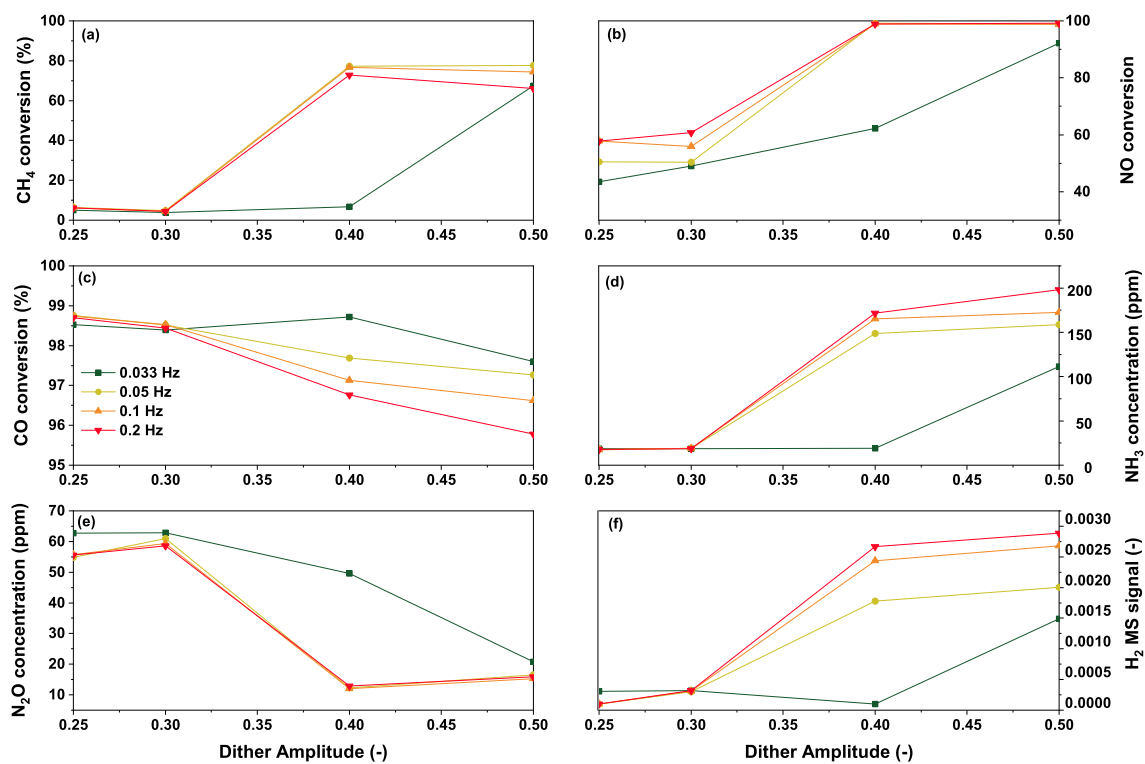
Figure 4.22: (a) CH_4, (b) NO and (c) CO conversion, (d) NH_3 and (e) N_2O concentration and (f) H_2 MS signal during O_2 dithering with different dithering amplitudes varied from $\lambda = 1\pm 0.25$ to $\lambda = 1\pm 0.50$ and different dithering frequencies from 0.033 Hz to 0.2 Hz on **Rh/A**.
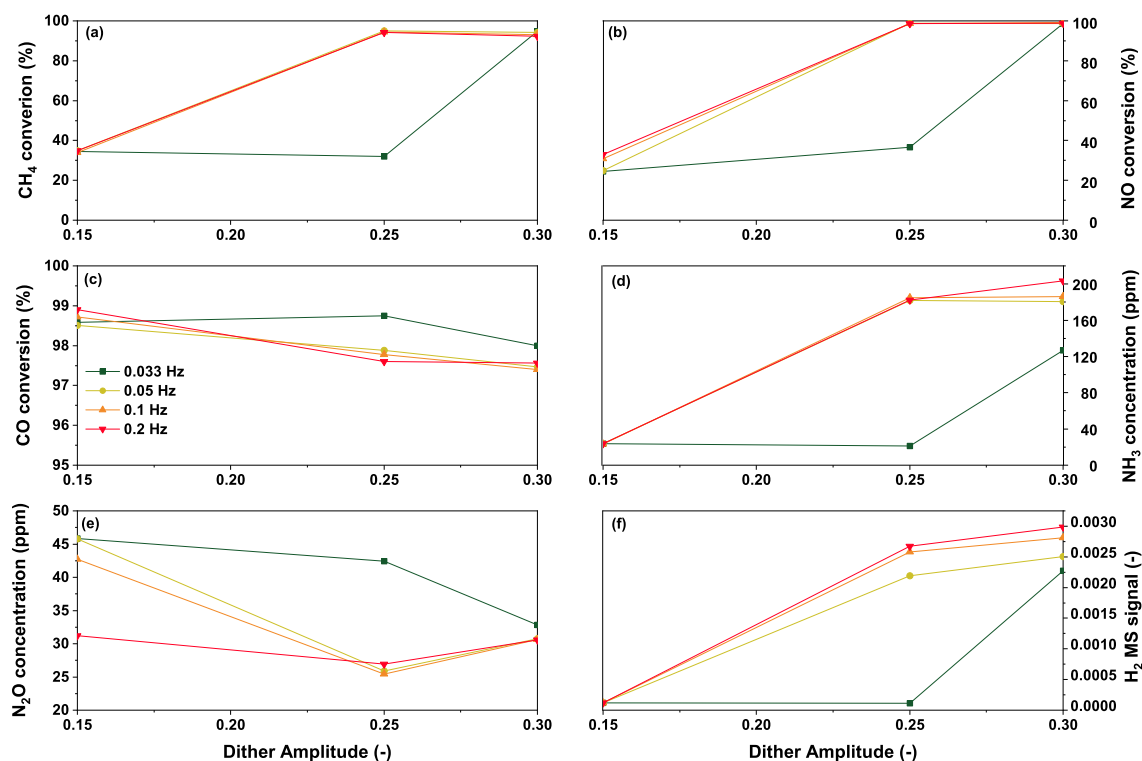
Figure 4.23: (a) CH_4, (b) NO and (c) CO conversion, (d) NH_3 and (e) N_2O concentration and (f) H_2 MS signal during O_2 dithering with different dithering amplitudes varied from $\lambda = 1\pm 0.15$ to $\lambda = 1\pm 0.30$ and different dithering frequencies from 0.033 Hz to 0.2 Hz on **Pd-Rh/A**.

Figure 4.21 shows that Pd/A gave the best results at an amplitude of 0.25 at the higher frequencies considering the NO and CH_4 conversion. However, considering the CO conversion, it seemed to prefer the lower frequencies which also resulted in the lowest concentration of NH_3. The optimized amplitude for Rh/A seemed to be 0.40 according to the results shown in Figure 4.22. Considering the NO conversion the three highest frequencies gave similar high conversions, but in view of the CH_4 and CO conversion the frequency of 0.05 Hz gave the highest conversion. It also resulted in a lower NH_3 concentration as well as a very low N_2O concentration. This seemed to also be the case for Pd-Rh/A, where the three highest frequencies resulted in more than 90 % conversion of NO and CH_4. However, these frequencies seemed to have a minimum effect on CO conversion, N_2O and NH_3 concentration. The frequency of 0.2 Hz was then chosen due to less oscillations as can be seen in Figure G.1 in Appendix G.1 which describes the outlet gases during 5 min of pulsing. A summary of the optimized parameters can be seen in Table 4.7.

Table 4.7: A summary of the optimized amplitude and frequency and their respective CH_4 and NO conversion for each sample during O_2 dithering.

Sample	Amplitude [-]	Frequency [Hz]	CH4 conversion [%]	NO conversion [%]
Pd/A	0.25	0.2	72.1	98.5
Rh/A	0.40	0.05	77.3	99.1
Pd-Rh/A	0.25	0.2	94.5	98.8

The optimized amplitudes of the catalysts (Table 4.7) were consistent with the CO-NO crossover points found during the lean-to-rich lambda sweep in Figure 4.11, 4.12 and 4.13. The crossover points were $\lambda = 0.9$, $\lambda = 0.75$ and $\lambda = 0.60$ for Pd/A, Pd-Rh/A and Rh/A respectively, which indicates that the amplitude must result in a λ-value (in the rich pulse) that is similar or higher than the CO-NO crossover point to fully reduce the catalyst. This corresponded exactly with the optimized amplitude for Pd-Rh/A and Rh/A at 0.25 and 0.40 respectively ($\lambda = 1 - A$), which was the lowest amplitude needed to achieve high conversions of NO and CH_4.

4.2.1.6 Temperature Ramp under Optimized O_2 Dithering Conditions

Varying the amplitude and the frequencies clearly had a positive impact on all the three catalysts under isothermal conditions. However, as to clearly see if the dithering conditions had an impact on the activity at lower temperatures, temperature ramps were conducted under the optimized conditions for each catalyst and are presented in Figure 4.24, 4.25 and 4.22 for Pd/A, Pd-Rh/A and Rh/A respectively.

In the lower temperature region over Pd/A, clear oscillations in the CH_4 and NO conversions were observed corresponding to the varying O_2 concentration. A closer look on the oscillations revealed that a higher NO conversion was obtained during the rich conditions and a higher CH_4 conversion during the lean conditions due to its oxidation by O_2 at lower temperatures (Figure G.2). The light-off temperature of CH_4 was similar to the temperature ramps under stoichiometric conditions, however CH_4-SR was triggered already at 400 °C, where a sharp increase in conversion was observed reaching 65 % before the curve stabilized and slowly moved towards maximum conversion. The NO conversion was already at 20 % at 300 °C and reached maximum conversion when H_2 was detected, the same temperature where CH_4 conversion increased sharply. The increased activity, already noticeable at 300 °C, is possibly due to a stimulation of a more active Pd^0/PdO mix by the periodic shifting between rich and lean conditions [8][19][26]. This active Pd^0/PdO mix seemed to be prone to reduction due to the low temperature triggering of CH_4-SR. The previous activity ramps over Pd/A usually resulted in a negative hysteresis during the cooling ramps (Figure 4.8, 4.14a), however the optimized O_2 dithering conditions clearly promoted a positive hysteresis where

most likely the dithering conditions maintained Pd in reduced state. Nevertheless, the clearly improved activity also resulted in unwanted by-products. The maximum concentration of N_2O was found to be ca. 300 ppm which was comparable to the amount produced in the stoichiometric ramps (Figure 4.8). When 79 % of NO was converting there was 68 % selectivity towards NH_3 at 600 °C for cycle 1 and 2 respectively. Additionally, a decrease in CO conversion was noticeable at higher temperatures. This was also observed by Gong et al. during dithering temperature ramps on a commercial Pd-based TWC for NG engines [26], who ascribed the CO slip to CH_4-SR (Reaction 1.6) or CH_4 partial oxidation (Reaction 4.3).

$$CH_4 + \frac{1}{2}O_2 \longrightarrow CO + 2H_2 \qquad (4.3)$$

Figure 4.24: CO, CH_4 and NO conversion, H_2 MS signal and NH_3 and N_2O concentration during two temperature cycles of heating (——) and cooling (‑ ‑ ‑) over **Pd/A** under optimized O_2 dithering conditions with $\lambda = 1 \pm 0.25$ at at a frequency of 0.2 Hz corresponding to 5 vol% H_2O, 0.15 vol% CH_4, 0.16 vol% NO, 0.7 vol% CO and 0.57 ± 0.143 vol% O_2 in Ar at a WHSV of 240 L h^{-1} g_{cat}^{-1}. The darker color correspond to the first cycle and the lighter color corresponds to the second cycle.

Similar to Pd/A, the temperature ramp under optimized O_2 dithering conditions over Pd-Rh/A resulted in a major improvement (Figure 4.25). The CH_4 light-off temperature of approximately 350 °C for both cycles resembled the one found in the stoichiometric ramps (Figure 4.10). However,

CH_4-SR seemed to be triggered at 448 °C with a sharp increase, which previously has been suggested as an effect of Rh. H_2 production followed immediately at 450 °C which was detected at an even lower temperatures in cycle 2. NO conversion started at 300 °C as previously seen for the stoichiometric ramps ((Figure 4.10 and 4.15c), however the conversion was as high as 50 % in cycle 2 leading to ca. 275 ppm N_2O formation which is more than what has been observed in the previous stoichiometric ramps. The NO conversion reached its maximum at the same temperature as the production of H_2 was observed. The production of NH_3 had its peak slightly later at 258 ppm, which shows the benefit of adding Rh to the Pd-catalyst. This benefit is also distinct from the large positive hysteresis lasting almost to 300 °C. From XAS it was clear that the positive hysteresis is due to Rh maintaining the metallic character of Pd, but as seen in Figure 4.25 this is further promoted by the O_2 dithering.
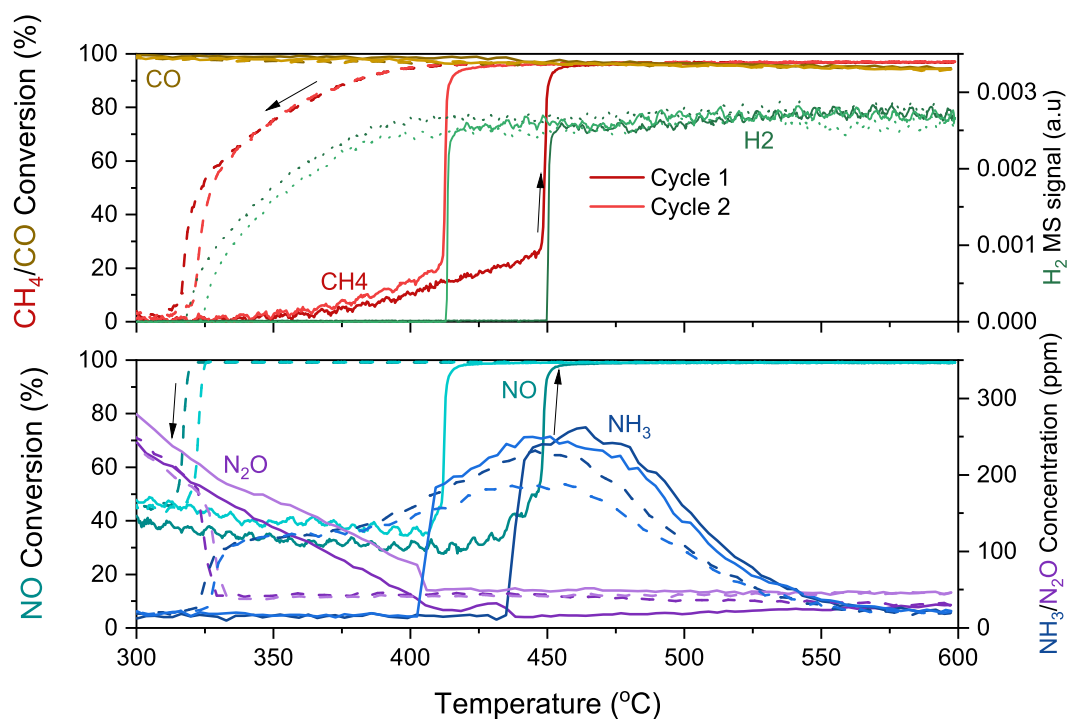
Figure 4.25: CO, CH_4 and NO conversion, H_2 MS signal and NH_3 and N_2O concentration during two temperature cycles of heating (—) and cooling (- - -) over **Pd-Rh/A** under optimized O_2 dithering conditions with $\lambda = 1 \pm 0.25$ at at a frequency of 0.2 Hz corresponding to 5 vol% H_2O, 0.15 vol% CH_4, 0.16 vol% NO, 0.7 vol% CO and 0.57 ± 0.143 vol% O_2 in Ar at a WHSV of 240 L h^{-1} g_{cat}^{-1}. The darker color corresponds to the first cycle and the lighter color correspond to the second.

Unlike the two other alumina-based samples, the optimized O_2 conditions for Rh/A were performed with an amplitude of 0.4 ($\lambda = 1 \pm 0.4$) and a frequency of 0.002 Hz. The corresponding temperature ramps are displayed in Figure 4.26, where the effect of the low frequency was clearly shown in the NO conversion. Compared to the CH_4 conversion, the oscillations for NO visibly followed the oscillations in the O_2 dosage as demonstrated in Figure G.3. This confirmed what was mentioned during the lambda sweeps in Section 4.2.1.2 that the NO conversion is more sensitive to the oxidation state than CH_4. Similar to Pd/A and Pd-Rh/A the CH_4 conversion started increasing at approximately 360 °C, where CH_4-SR was detected at 430, 410 and 400 for cycle 1, 2 and 3 respectively with an immediate H_2 production as also observed on Pd-Rh/A. The oscillations from the varying O_2 amplitude was also recognisable in the H_2 MS signal.

At 300 °C, 70 % NO was already converted. However, this high conversion resulted in the highest concentration of N_2O over Rh/A of 210 ppm. NO reached its maximum conversion at the same temperature as H_2 was detected, and a peak of NH_3 was observed which had not been detected in previous activity ramps over Rh/A. However, instead of increasing in concentration with temperature as on Pd/A, it decreased to $\sim$ 0 ppm in agreement with showing Rh's ability to suppress NH_3 formation. The O_2 dithering had a negative effect on CO conversion as already observed by the CO-slip over Pd/A and Pd-Rh/A. However, over Rh/A CO conversion never reached 100 % conversion, but stayed constant at 90 %. Tagliaferri et al. [154], who studied O_2 dithering over Rh containing TWC for gasoline engines, observed low CO conversion already at 310 °C implying that O_2 dithering inhibits the CO oxidation performance. However, due to smaller oscillations, the better light-off temperatures and the higher CO conversion over Pd/A and Pd-Rh/A, activity temperatures over Rh/A was also performed with the frequency of 0.2 Hz while keeping the amplitude of 0.4 (Figure 4.27).
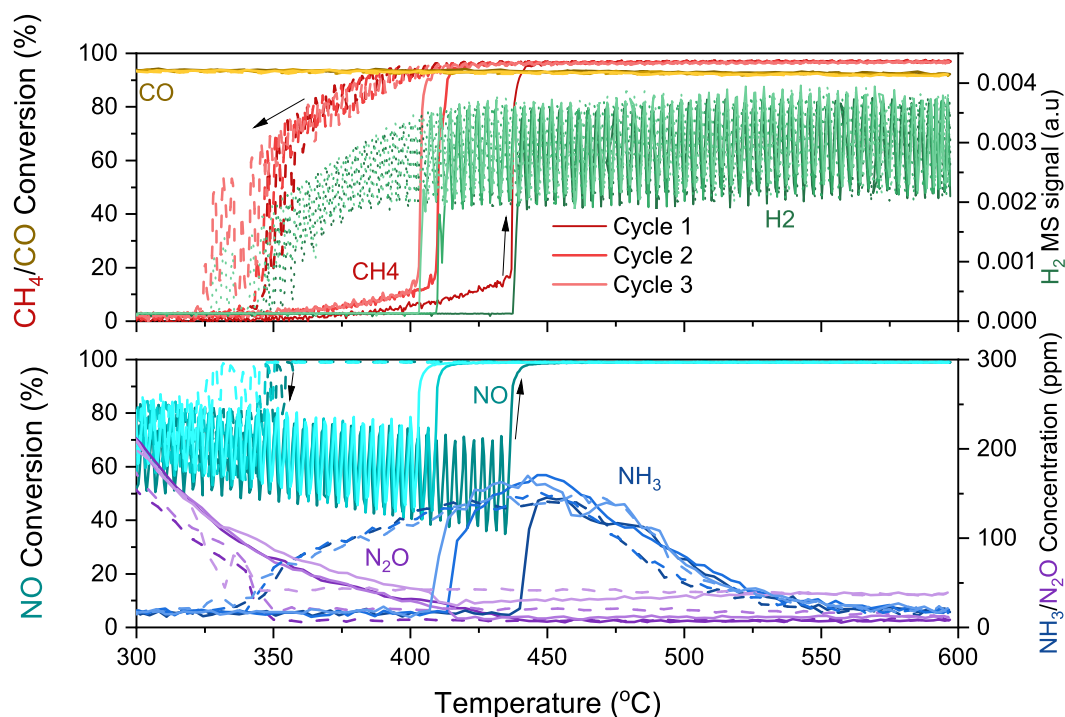
Figure 4.26: CO, CH_4 and NO conversion, H_2 MS signal and NH_3 and N_2O concentration during three temperature cycles of heating (——) and cooling (- - -) over **Rh/A** under optimized O_2 dithering conditions with $\lambda = 1 \pm 0.4$ at at a frequency of 0.05 Hz corresponding to 5 vol% H_2O, 0.15 vol% CH_4, 0.16 vol% NO, 0.7 vol% CO and 0.57 ± 0.228 vol% O_2 in Ar at a WHSV of 240 L h^{-1} g_{cat}^{-1}. The darker color corresponds to the first cycle and the lighter colors corresponds to the second and third cycle.

The change in the frequency from 0.05 Hz to 0.2 Hz showed an improvement (Figure 4.27). The light-off temperature for CH_4 was found at 350 °C where CH_4-SR was triggered already at 410 °C with a maximum conversion at 434 °C for cycle 1. However, during the cooling ramp already 30% CH_4 was converted at 300 °C, resulting in a light-off temperature close to 300 °C for cycle 2. In cycle 3, there was no light-off temperature in the chosen temperature range as CH_4 was highly converted. This promoted the NO conversion as NO usually reaches maximum conversion once a net H_2 production is detected. NO reached its maximum conversion at 414 °C for cycle 1, 331 °C for cycle 2 and stayed fully converted throughout cycle 3 which resulted in no N_2O in contrary to the behaviour in oxidizing environments. However, NH_3 was observed in all cycles with a maximum of 250 ppm for the heating ramp of cycle 2 and 3 at 450 °C. This amount was still lower than what was observed for Pd-Rh/A (Figure 4.25) and Pd/A (Figure 4.24).
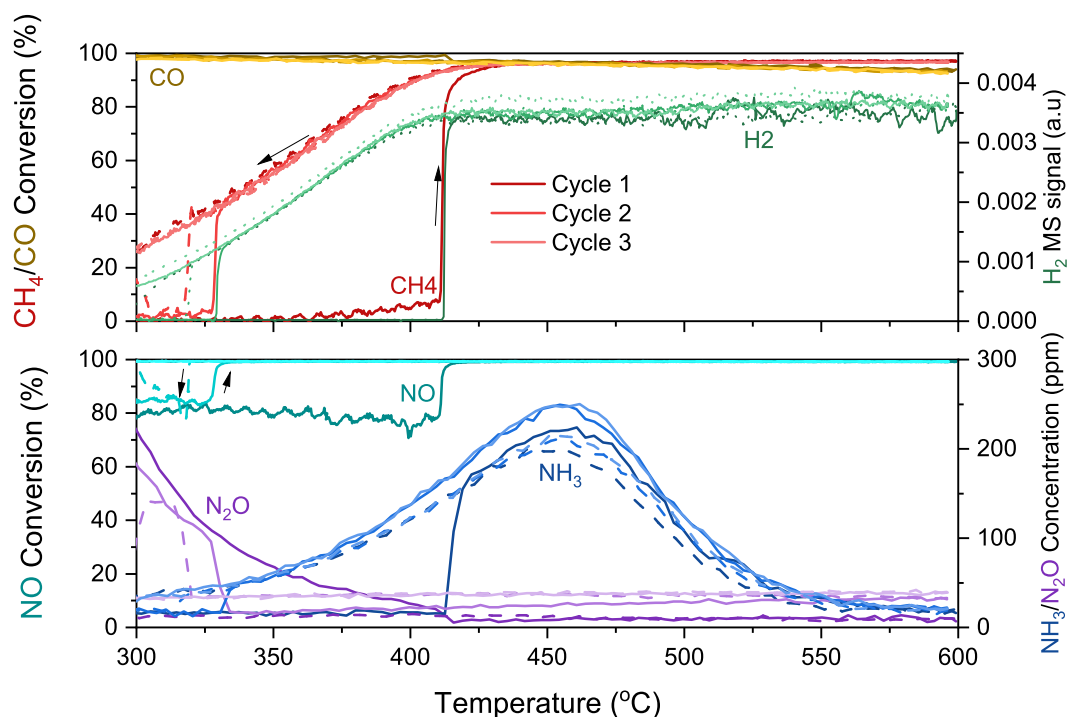
Figure 4.27: CO, CH_4 and NO conversion, H_2 MS signal and NH_3 and N_2O concentration during three temperature cycles of heating (——) and cooling (- - -) over **Rh/A** under optimized O_2 dithering conditions with $\lambda = 1 \pm 0.4$ at at a frequency of 0.2 Hz corresponding to 5 vol% H_2O, 0.15 vol% CH_4, 0.16 vol% NO, 0.7 vol% CO and 0.57 ± 0.228 vol% O_2 in Ar at a WHSV of 240 L h^{-1} g_{cat}^{-1}. The darker color corresponds to the first cycle and the lighter colors corresponds to the second and third cycle.

A noticeable trend during the temperature ramps under O_2 dithering conditions was the sharp increase in CH_4 conversion for Pd-Rh/A and Rh/A compared to Pd/A once SR is triggered.

All the ramps performed under O_2 dithering conditions seemed to enhance the activity which is consistent with results from the literature [163][8][164][27][26][154][165]. Some authors proposed the catalytic enhancement to be a result of dithering restraining self-poisoning on the surface of the catalyst, but over TWC for gasoline engines [154][165]. Other authors ascribe the positive results to a more active Pd/PdO mix due to the shifting between net-reduced and net-oxidized conditions [163][8][164][27]. Clearly Rh/A resulted in the most active catalyst under O_2 dithering conditions. A possible explanation is that the O_2 dithering promotes reduction of the active metals which is most beneficial for Rh/A, as discussed in Section 4.2.1.2, where reduced Rh seemed more active towards CH_4-SR and WGS than the reduced Pd-based catalysts. However, there is not much results in literature on O_2 dithering over a Rh-based TWC. This should be further investigated as clearly O_2 dithering has a tremendous impact on the Rh-catalyst compared to the static operations

and the other catalysts investigated.

4.2.1.7 Stability Test

Isothermic stability tests were carried out at 420 °C over Pd-Rh/A over static conditions ($\lambda = 0.75$ and $\lambda = 1$) and dynamic conditions ($\lambda = 1 \pm 0.25$ at 0.2 Hz) for 60 h (Figure 4.28) to see if any deactivation occurred during pulsing.
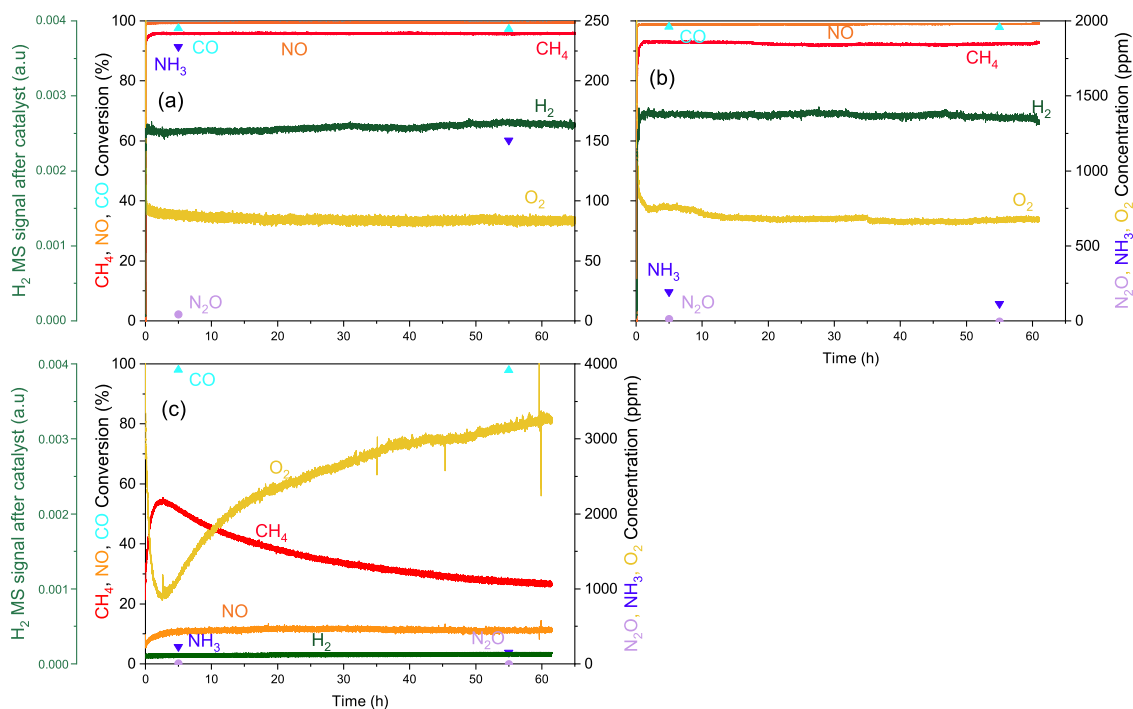
Figure 4.28: Stability tests at 420 °C for 60 h over Pd-Rh/A under different O_2 dosage (a) $\lambda = 0.75$, (b) $\lambda = 1 \pm 0.25$ at 0.2 Hz and (c) $\lambda = 1$.

Comparing the stability tests, the Pd-Rh/A exposed to $\lambda = 0.75$ (Figure 4.28a) and $\lambda = 1 \pm 0.25$ at 0.2 Hz (Figure 4.28b) displayed comparable results regarding NO and CH_4 conversion. During stoichiometric temperature ramps over Pd-Rh/A, only CH_4 oxidation was observed at 420 °C (Figure 4.10). This was also detected during the stability test at $\lambda = 1$ (Figure 4.28c), however a decrease in activity was observed after the first 3 h on stream indicating a deactivation of the catalyst under stoichiometric conditions. This is possibly attributed to the formation of inactive $Pd(OH)_2$ due to the H_2O in the feed that reacts with Pd when an excess of O_2 is present [166]. TEM images were also collected after the stability tests and are shown in Figure 4.29 with its corresponding average particle size. The average particle size of Pd-Rh/A after the stability test

under dynamic ($\lambda = 1 \pm 0.25$) conditions was 6.2 nm, which is roughly the same as the average particle size of the fresh Pd-Rh/A (6.3 nm). However, sintering was observed for both Pd-Rh/A-samples exposed to static conditions resulting in a growth visible in the TEM images and an average particle size of 8.0 nm and 8.6 nm for $\lambda = 0.75$ and $\lambda = 1$ respectively. The deactivation was not visible under the stability test for $\lambda = 0.75$, indicating that the time on stream was not long enough to distinguish the sintering effect on the activity.
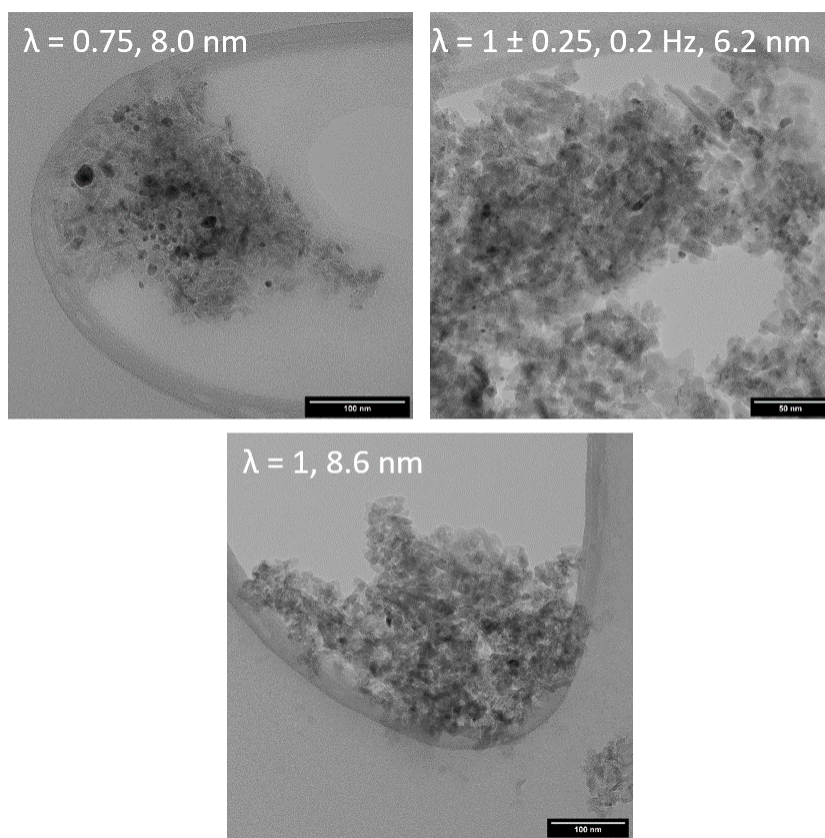
Figure 4.29: TEM images of Pd-Rh/A its corresponding average particle size after stability test under different conditions.

As seen in Section 4.2.1.6, O_2 dithering conditions are beneficial for high conversion, but from the stability tests it seems to be advantageous against deactivation and metal particle sintering as well.

4.2.2 Ceria-Zirconia Supported Catalysts

Real life TWC usually contain ceria as it has the ability to store, release and exchange O_2 through its redox properties and therefore enhances the activity as mentioned in Section 1.3.4.2. For this purpose CZ supported samples were synthesized as a comparison with the non-reducing support alumina. Unfortunately, due to time restrictions, only Rh/CZ and Pd-Rh/CZ were synthesized and tested. These active metals were chosen due to the impressive results of Rh/A under O_2 dithering conditions and the interesting promotion of the redox properties of Pd by Rh in Pd-Rh/A.

4.2.2.1 Stoichiometric Temperature Ramps after Reduction and Oxidation Pretreatment

First, stoichiometric ($\lambda = 1$) temperature ramps were conducted over Rh/CZ (Figure 4.30). Similar to Rh/A (Figure 4.9), only oxidization of CH_4 by Reaction 1.2 was observed which was apparent by an increase in MS-signal of H_2O and CO_2 (Figure E.4). The CH_4 light-off temperature was found at approximately 410 °C for each cycle reaching a maximum CH_4 conversion of 62 % at 600 °C. The lack of higher conversion over Rh/CZ was most likely due to the O_2 back spillover from CZ to Rh, as seen in the TPR-profiles (Figure 4.4) and from the high OSC (Table 4.4), that stabilizes Rh in an oxidized state which results in a lower activity [167], especially for NO reduction as it prefers a net reducing environment [27]. It has also been suggested that Rh diffuses into the ceria lattice during oxidation at 500 °C [168], which is similar conditions as the oxidation pretreatment that reaches 600 °C. The NO conversion over Rh/CZ was also found to be lower than over Rh/A most likely due to the oxidized Rh. However, the two Rh-based catalysts had an equal selectivity towards N_2O (Reaction 1.5). The CO conversion seemed relatively constant throughout the ramps of approximately 98 %.
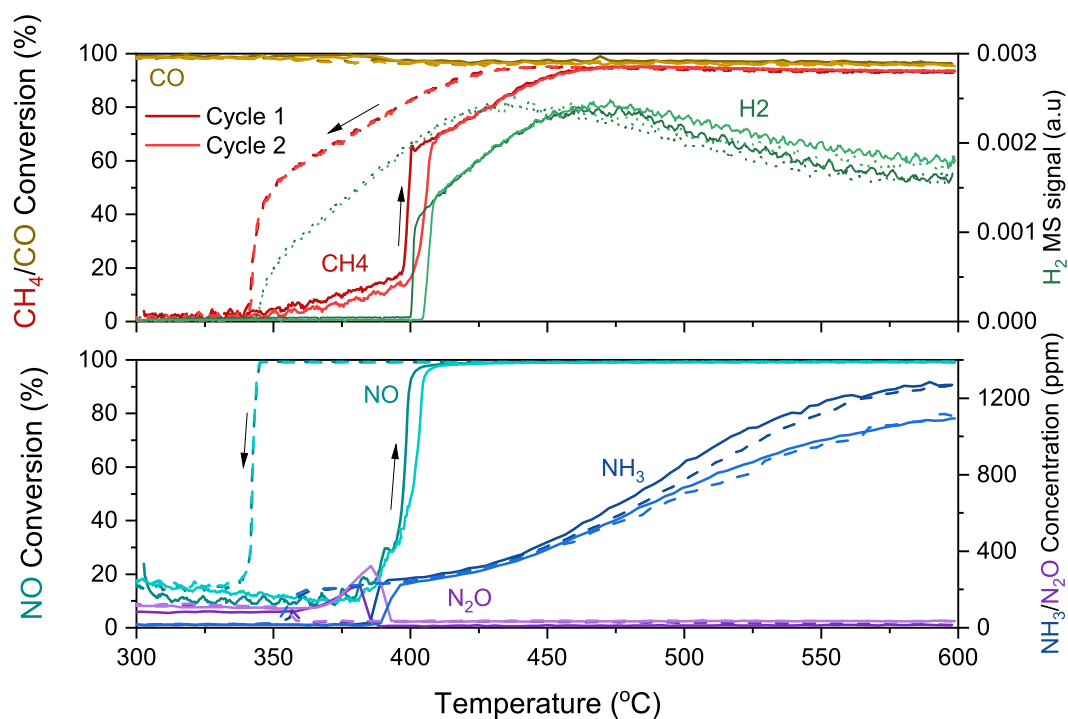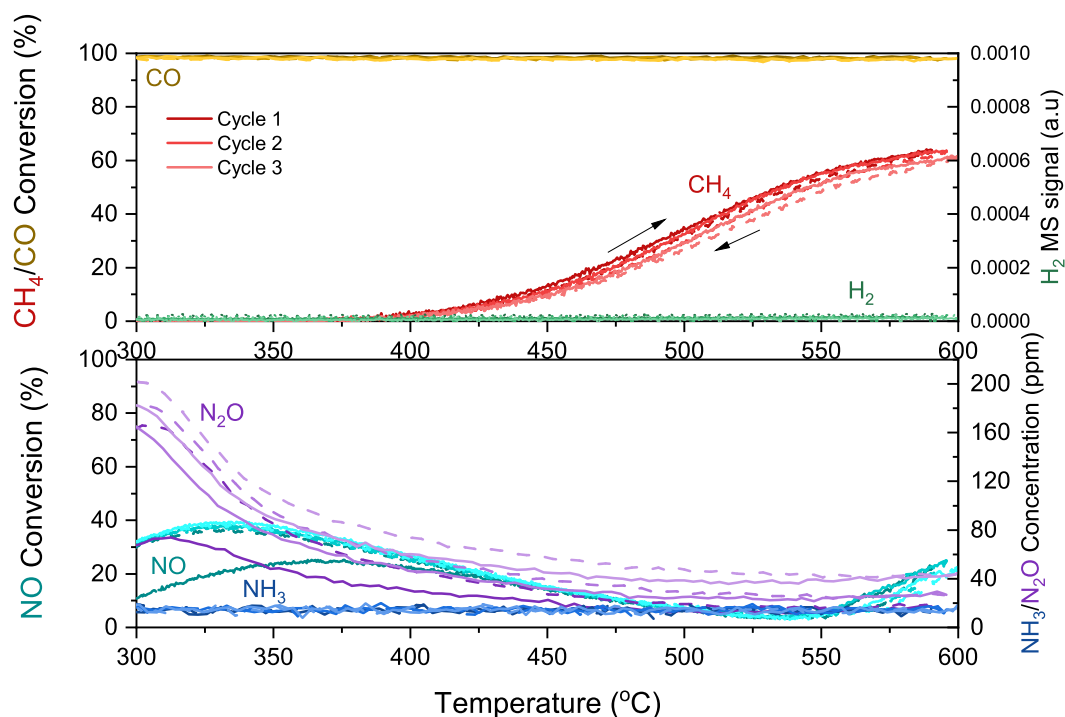
Figure 4.30: CO, CH_4 and NO conversion, H_2 MS signal and NH_3 and N_2O concentration over during three temperature cycles of heating (——) and cooling (- - -) over **Rh/CZ** under stoichiometric conditions corresponding to 5 vol % H_2O, 0.15 vol% CH_4, 0.16 vol% NO, 0.7 vol% CO and 0.57 vol% O_2 in Ar at a WHSV of 240 L h^{-1} g_{cat}^{-1}. The darker color corresponds to the first cycle and the lighter colors corresponds to the second and third cycle.

The stoichiometric temperature ramps over Pd-Rh/CZ ars presented in Figure 4.31. A similar light-off temperature for CH_4 conversion to Pd-Rh/A (Figure 4.10), at ca. 350 °C, was observed for all three cycles. As proved by Figure E.5, the increase in H_2O and CO_2 signal indicated that CH_4 was oxidized according to Reaction 1.2 until 578, 561 and 568 °C for cycle 1, 2 and 3 respectively where a decrease in H_2O pointed to the promotion of CH_4-SR (Reaction 1.6). This is ca. 50 °C higher than in Pd-Rh/A even though it has been mentioned in literature that ceria promotes CH_4-SR. However, the positive hysteresis over Pd-Rh/CZ was ca. 40 °C wider than the Pd-Rh/A which indicates this effect. The late triggering of CH_4-SR was most likely due to the same reason as the low conversion of Rh/CZ; the high OSC (Table 4.4) made it harder to reduce the catalyst. From Figure E.3 the O_2 signal was negligible at ca. 500 °C, suggesting that the increase in CH_4 oxidation from this temperature until CH_4-SR was due to O_2 stored in the catalyst or O_2 formed from the NO reduction mostly by Reaction 1.4, but also by Reaction 1.5 as a small amount of N_2O was detected in all heating ramps at approximately 525 °C. The NO conversion reached its maximum at the same temperature as a net H_2 production was detected indicating that NO was being reduced

according to Reaction 4.15. No NH_3 was detected at higher temperatures, however in the cooling ramp a small peak was present at around 475 °C. This was around the same temperature as a peak of NH_3 was observed over Rh/A during O_2 dithering temperature ramps (Figure 4.26 and 4.27) and Pd-Rh/A (Figure 4.25 and 4.15), which indicates that if the Rh-catalyst is under a net reducing atmosphere at around this temperature the formation of NH_3 is not fully suppressed.

Figure 4.31: CO, CH_4 and NO conversion, H_2 MS signal and NH_3 and N_2O concentration over during three temperature cycles of heating (——) and cooling (- - -) over **Pd-Rh/CZ** under stoichiometric conditions corresponding to 5 vol % H_2O, 0.15 vol% CH_4, 0.16 vol% NO, 0.7 vol% CO and 0.57 vol% O_2 in Ar at a WHSV of 240 L h^{-1} g$_{cat}^{-1}$. The darker colors corresponds to the first cycle and the lighter color corresponds to the second and third cycle.

Due to the visible improvement in activity over the alumina-based samples under stoichiometric conditions after a reductive pretreatment, it was also of interest to study the same effect on the CZ-based samples. Figure 4.32 and Figure 4.33 display the comparison between the effect of the oxidation and the reduction pretreatment under stoichiometric conditions during the last cycle over Rh/CZ and Pd-Rh/CZ respectively. The full three cycles performed after reduction pretreatment can be found in Figure F.4 and F.5 for Rh/CZ and Pd-Rh/CZ respectively. The improvement that was observed by the reduction pretreatment over both Rh/A and Pd-Rh/A (Figure 4.14b/c and 4.15b/c) was not observed over Rh/CZ (Figure 4.32) and Pd-Rh/CZ (Figure 4.33). After the reduction pretreatment the catalysts were most likely reduced. However, the oxygen storage

components acted as a O_2 buffer as soon as the full reactive mixture was fed to the catalyst keeping the catalysts oxidized [8]. Nevertheless, it would be interesting to see if full reduction of the CZ-based samples were achieved after the reductive pretreatment and how it reacts at 300 °C when the mixture is introduced to the system using for example XAS.

Similar to Pd-Rh/A, barely any NH_3 formation was observed over Pd-Rh/CZ. A stoichiometric temperature ramp over 11 wt% Pd/CZ (Figure F.6) can confirm that the suppression of NH_3 was due to Rh only as no significant improvement was observed between Pd/A (Figure 4.8) and Pd/CZ
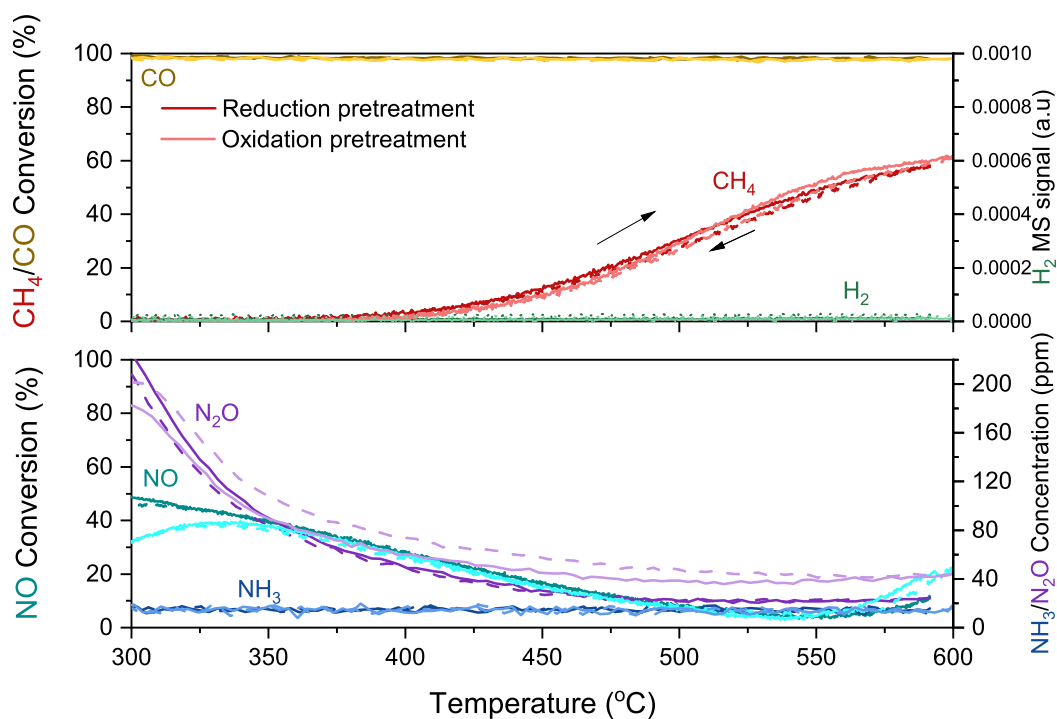
Figure 4.32: CO, CH_4 and NO conversion, H_2 MS signal and NH_3 and N_2O concentration during the last cycle of temperature at $\lambda = 1$ over **Rh/CZ** after reduction (dark colors) and oxidation (bright colors) pretreatments
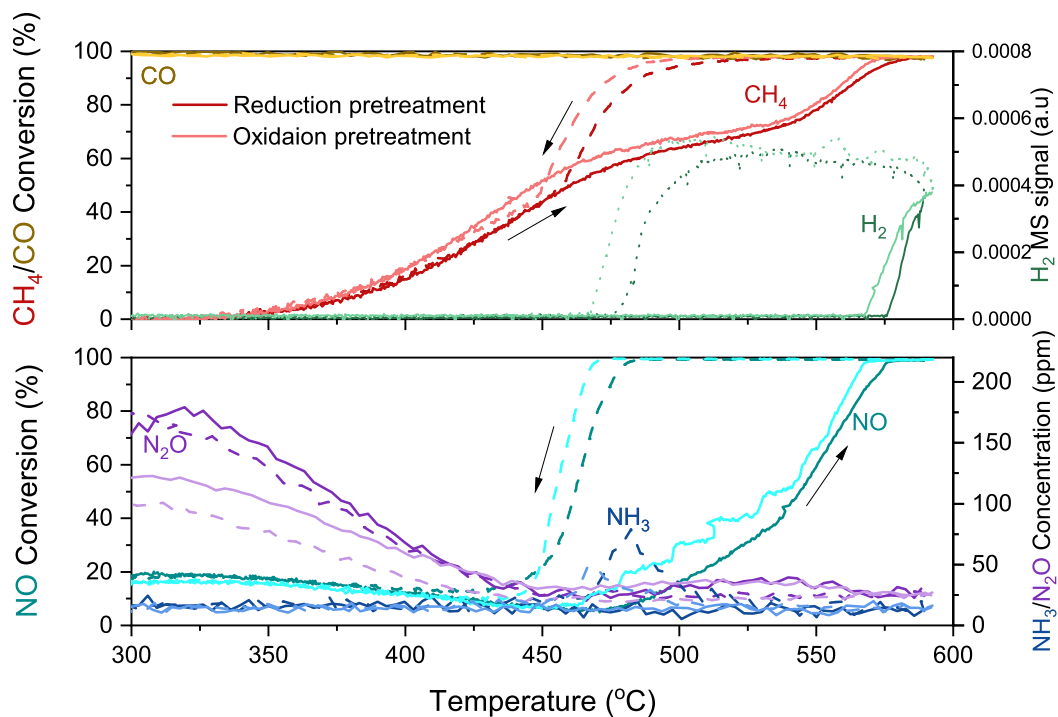
Figure 4.33: CO, CH_4 and NO conversion, H_2 MS signal and NH_3 and N_2O concentration during the last cycle of temperature at $\lambda = 1$ over **Pd-Rh/CZ** after reduction (dark colors) and oxidation (bright colors) pretreatments

.

4.2.2.2 Lambda Sweeps

Lean-to-rich and rich-to-lean lambda sweeps were also conducted over the CZ-based samples to see how the reducible support affects the metal particles compared to the alumina-based samples considering the CO-NO crossover point. The sweeps were performed at 420 °C as this was a temperature with low conversion in stoichiometric ramps over both Rh/CZ and Pd-Rh/CZ as seen in Section 4.2.2.

Compared to the lean-to-rich sweeps over Rh/A (Figure 4.12a) where no CH_4 conversion was observed on the lean side, Rh/CZ seemed to promote low conversion of CH_4 (roughly 6 %, Figure 4.34a). This was in accordance with the results obtained from the stoichiometric ramps at the same temperature (Figure 4.32). The NO followed the same trend as over Rh/A, where the concentration decreased while going to richer conditions with a corresponding production of N_2O until reaching maximum conversion at the CO-NO crossover point found at $\lambda = 0.6$, the same λ as Rh/A. At the crossover point, a corresponding increase in NH_3 and CO concentration was identified. However, the CO concentration did not increase as much as over Rh/A as well as the CH_4 concentration which reached 450 ppm at $\lambda = 0$ compared to 1000 ppm over Rh/A. This is because CZ promotes CH_4-SR. However, it is clear that CZ also promotes the WGS, as the amount of H_2 was the same as over Rh/A, but also a higher amount of NH_3 indicating a higher overall H_2 production over Rh/CZ. This can be confirmed by a study conducted by Halabi et al. [57], who performed WGS experiment over $Ce_{0.6}Zr_{0.4}O_2$ in a temperature range of 400-575 °C. They observed CO conversion already at 400 °C and concluded that CZ is active towards the WGS.

Following the rich-to-lean sweep (Figure 4.34a), the rich side was very similar to the rich side in the lean-to-rich sweeps. However the CO-NO crossover point was found at $\lambda = 0.9$, a lower λ-value than Rh/A ($\lambda = 0.95$). As discussed previously CZ promotes an O_2 back spillover to the active metals, and therefore promotes oxidation at richer λ-values. On the lean side of the crossover point the concentrations of CH_4 and NO were very similar to the concentrations on the lean side in Figure 4.34a at identical λ-values.
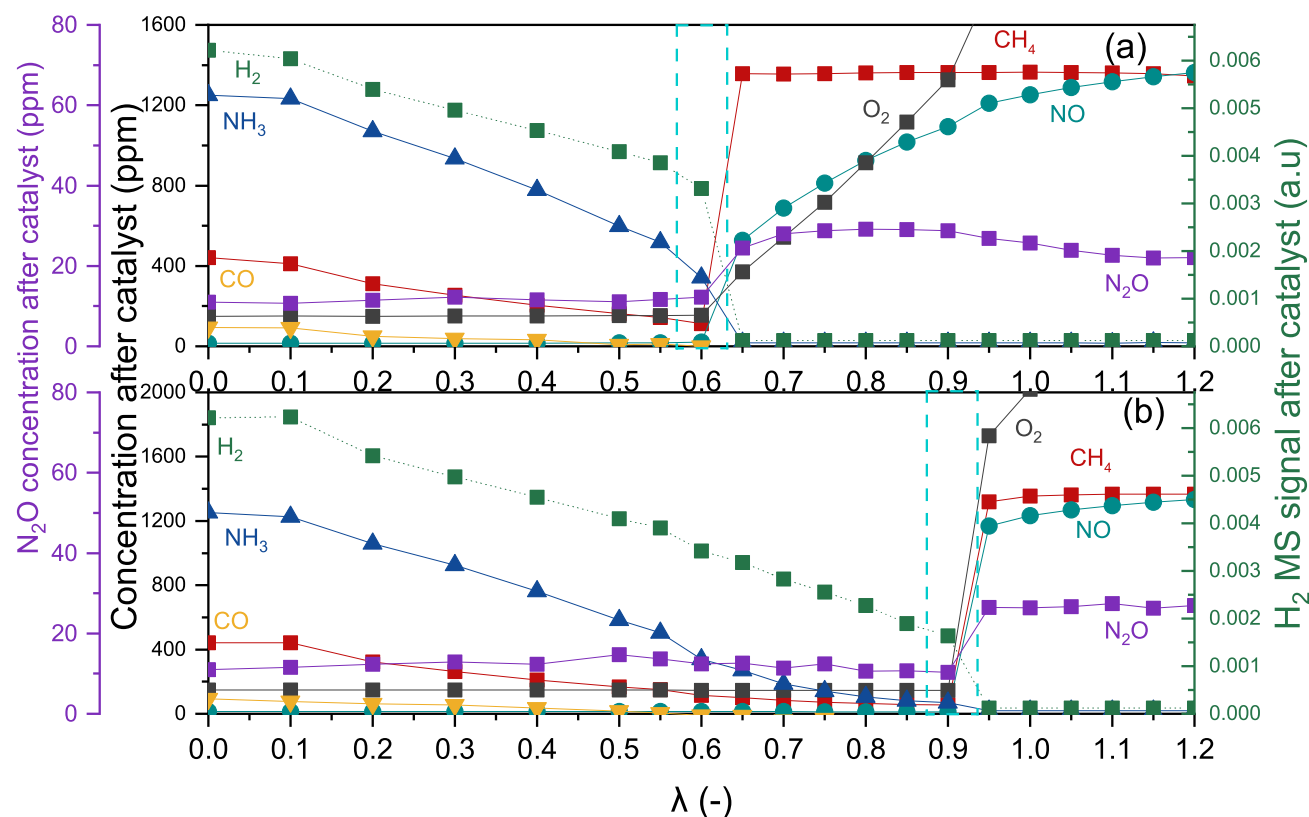
Figure 4.34: The concentration of CO, CH_4, NO, O_2, NH_3 and N_2O and H_2 MS signal after catalyst on **Rh/CZ** during steady state lambda sweep from (a) lean-to-rich and (b) rich-to-lean at 420 °C.

The experimental lambda sweeps over Pd-Rh/CZ are presented in Figure 4.35a and 4.35b for lean-to-rich and rich-to-lean sweep respectively. Looking at the lean side of the lean-to-rich sweep a constant CH_4 conversion of 20 % was observed. However, at the λ-value in the sweeps over Pd-Rh/A there seemed to be a higher conversion of CH_4 (Figure 4.13a). As Pd is more active for direct CH_4 oxidation in a mixed Pd/PdO state it is possible that the lower conversion over Pd-Rh/CZ is due to CZ promoting Pd oxidation which inhibits CH_4 oxidation by O_2.

The NO concentration seemed to follow the same trend as over Pd-Rh/A, but higher concentrations were observed possibly also due to the O_2 back spillover from CZ. The CO-NO crossover point was identified at $\lambda = 0.7$ due to the breakthrough of H_2 and CO. This point was located at a richer λ-value than for Pd-Rh/A ($\lambda = 0.75$). As CO and CH_4 were the only reducing species present at the lean side, the shift was most likely due to the lower CH_4 conversion observed on Pd-Rh/CZ reducing the catalyst at a slower rate. After the crossover point, the concentrations at the rich

side were more similar to the concentrations at the rich side over Rh/CZ (Figure 4.34a) than over Pd-Rh/A (Figure 4.13a), possibly pointing towards a metal-CZ interaction being more efficient under richer conditions.
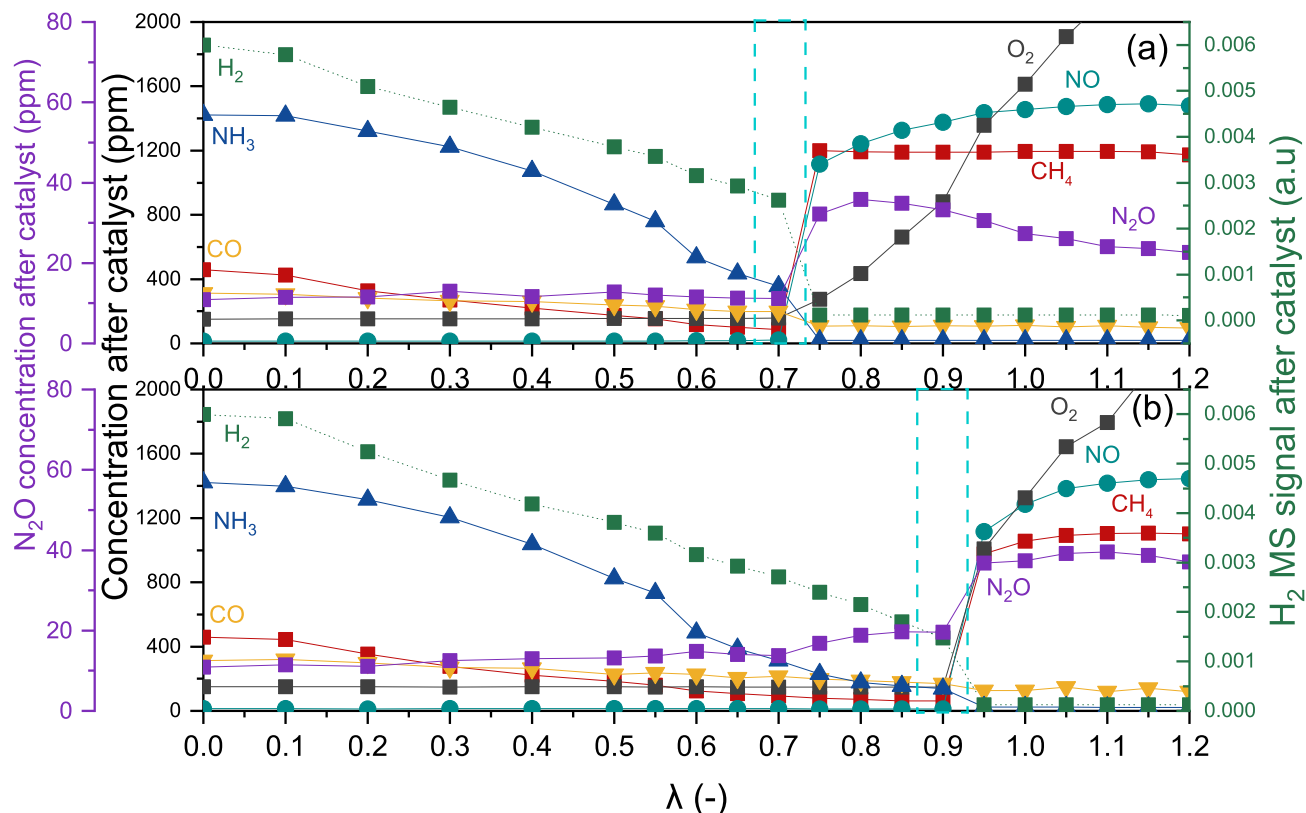
Figure 4.35: The concentration of CO, CH_4, NO, O_2, NH_3 and N_2O and H_2 MS signal after catalyst on **Pd-Rh/CZ** during steady state lambda sweep from (a) lean-to-rich and (b) rich-to-lean at 420 °C.

Looking at the rich-to-lean sweep (Figure 4.35b), the rich side was again quite similar to the rich side during the lean-to-rich sweep except that the crossover point was located at $\lambda = 0.9$. This is the same λ-value at the crossover point for both Rh/CZ and Pd-Rh/A.

Comparing the lambda sweeps of the CZ-based samples with the sweeps obtained over the alumina-based samples (Section 4.2.1.2), CZ did not seem to promote a wider lambda window of activity on the catalysts. However, it was evident that CZ promoted CH_4-SR and WGS under richer conditions.

4.2.2.3   Optimization of O_2 Dithering Conditions

As observed in Section 4.2.1.6, temperature ramps under the optimized O_2 dithering conditions resulted in great improvements for all alumina-based samples. As a result optimization of O_2 dithering conditions was also attempted over Rh/CZ (Figure 4.36) and Pd-Rh/CZ (Figure 4.37). The steady state experiments were again carried out at 420 °C with a varied amplitude, A, around $\lambda = 1$ at different frequencies. The chosen amplitudes were based on the λ-value at the CO-NO crossover point in the previous section.

Similar to the optimization over the alumina-based samples, the amplitude seemed to have more impact towards the CH_4 and NO conversion than the frequency. However, the frequency still had an effect especially over Pd-Rh/CZ (Figure 4.37). The lower frequencies (0.33 and 0.05 Hz) did not seem to trigger CH_4-SR at low amplitudes probably due to the longer exposure time of O_2 during the lean pulse keeping the catalyst more oxidized during the rich pulse. Over Rh/CZ (Figure 4.36), the frequencies barely had a visible impact on the CH_4 and NO conversions. As the frequencies had similar impact on Pd-Rh/A and Rh/A, the difference on the CZ-based samples might be due to different interactions between the active metals and CZ.

For Rh/CZ the optimized amplitude of O_2 dithering corresponded to $\lambda = 1 \pm 0.4$ which resulted in roughly 90 % CH_4 conversion and 99 % NO conversion. As mentioned previously the frequencies did not have a great impact on the conversions, however the higher frequencies resulted in a higher NH_3 production (Figure 4.36d). The optimized frequency resulted in 0.05 Hz, hence the same O_2 dithering conditions as chosen for Rh/A. However, these conditions resulted in a CH_4 conversion of 77 % over Rh/A, again indicating that CZ is promoting CH_4-SR in net reducing conditions.
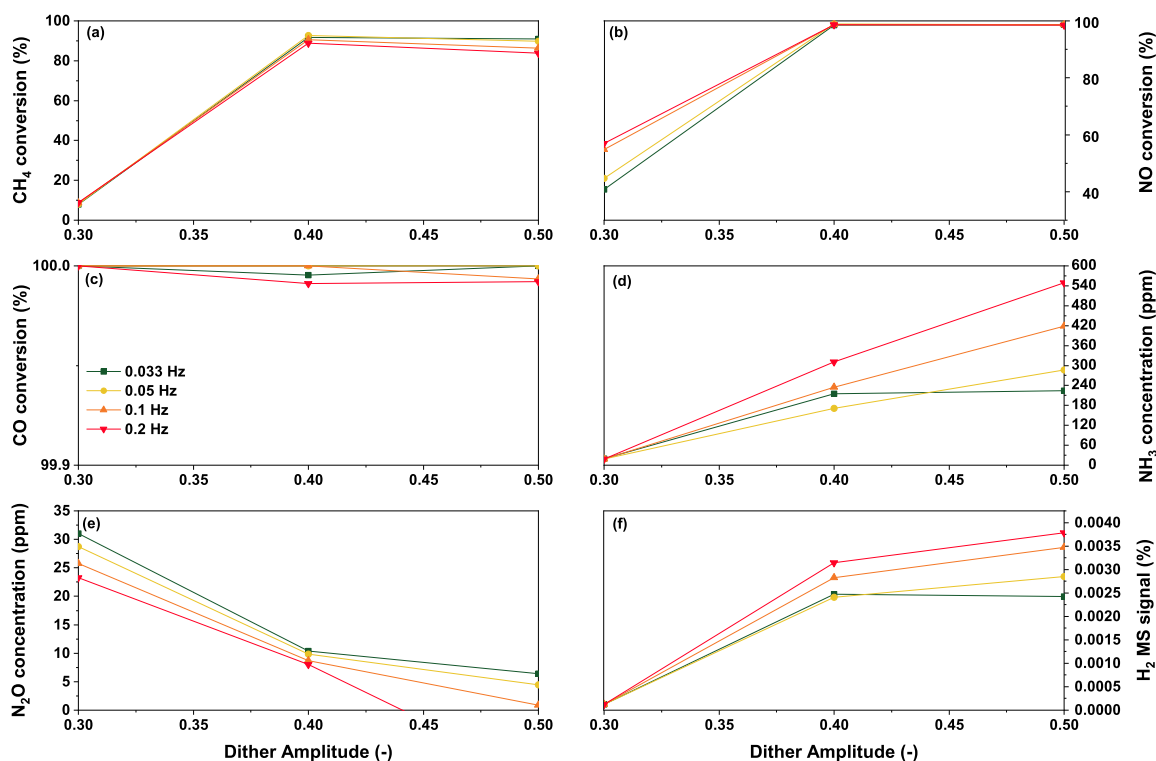
Figure 4.36: (a) CH_4, (b) NO and (c) CO conversion, (d) NH_3 and (e) N_2O concentration and (f) H_2 MS signal during O_2 dithering with different dithering amplitudes varied from $\lambda = 1\pm 0.30$ to $\lambda = 1\pm 0.50$ and different dithering frequencies from 0.033 Hz to 0.2 Hz on **Rh/CZ**.

For Pd-Rh/CZ a O_2 dithering amplitude of $\lambda = 1 \pm 0.3$ gave the best results with 93 % CH_4 and 98 % NO conversions at frequencies of 0.1 and 0.2 Hz. The frequencies did not seem to influence the N_2O formation at all, so the optimized frequency was chosen based on CO conversion and NH_3 production which resulted in a frequency of 0.1 Hz.
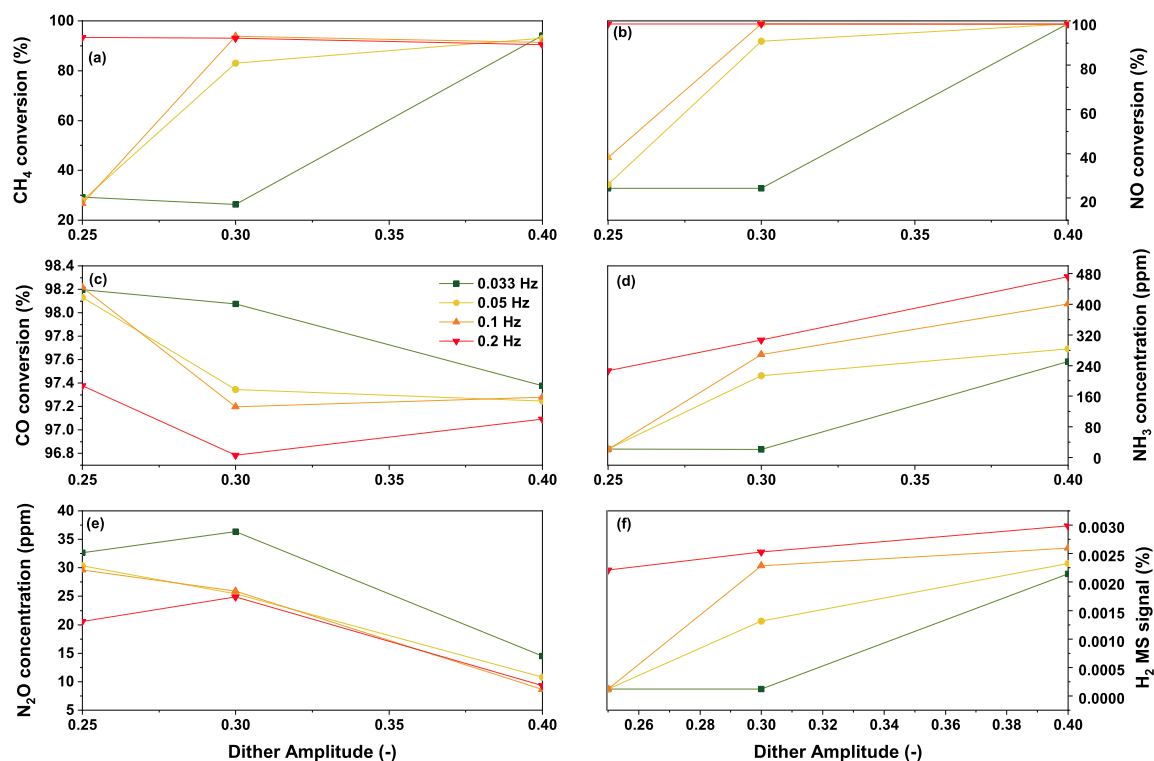
Figure 4.37: (a) CH_4, (b) NO and (c) CO conversion, (d) NH_3 and (e) N_2O concentration and (f) H_2 MS signal during O_2 dithering with different dithering amplitudes varied from $\lambda = 1\pm 0.25$ to $\lambda = 1\pm 0.40$ and different dithering frequencies from 0.033 Hz to 0.2 Hz on **Pd-Rh/CZ**.

4.2.2.4 Temperature Ramps Under the Optimized O_2 Dithering Conditions

As the alumina-based samples, the CZ-based samples showed a major improvement when varying the O_2 feed as optimized in Section 4.2.2.3 in temperature ramps. Previous temperature ramps over Rh/CZ did not result in any significant activity where the catalyst was not able to trigger CH_4-SR after oxidation and reduction pretreatments (Figure 4.32). Nevertheless, the optimized O_2 dithering conditions seemed to be key to enhance the activity of Rh/CZ (Figure 4.38). The light-off temperature of CH_4 conversion was found at roughly 350 °C for all three cycles, and reached its maximum conversion already at 470, 440 and 430 °C for cycle 1, 2 and 3 respectively, the same temperature at which H_2 was observed. The NO conversion was already between 40 and 80 % depending on the oscillations and produced roughly 210 pmm N_2O at 300 °C. The N_2O concentration decreased with increasing temperature and was negligible once NH_3 appeared and NO achieved maximum conversion shortly after at the same temperature as CH_4.

The O_2 dithering conditions over Rh/CZ were identical to the one obtained over Rh/A (Figure 4.27). An improvement of CO conversion was achieved over Rh/CZ most likely due to its high OSC. However the maximum conversions of NO and CH_4 were reached at a higher temperature over Rh/CZ, possibly due to the 20 s long pulses oxidizing Ce in the lean pulse which keeps the metal more oxidized in the following rich pulse.

Halibi et al. [57], suggested a mechanism for CH_4-SR over $Rh/Ce_{0.6}Zr_{0.4}O_2$ where CH_4 adsorbs dissociatively on the active sites of Rh, and the H_2O on ceria. However, Kundakovic et al. [169], proposed that the dissociation of H_2O only happens on reduced ceria and is promoted by Rh at lower temperatures. This might be a possible reason for the wide positive hysteresis of Rh/CZ lasting all the way to 305 °C during the cooling ramp where also CZ seemed to even out the pulses as they are not as visible as over Rh/A.
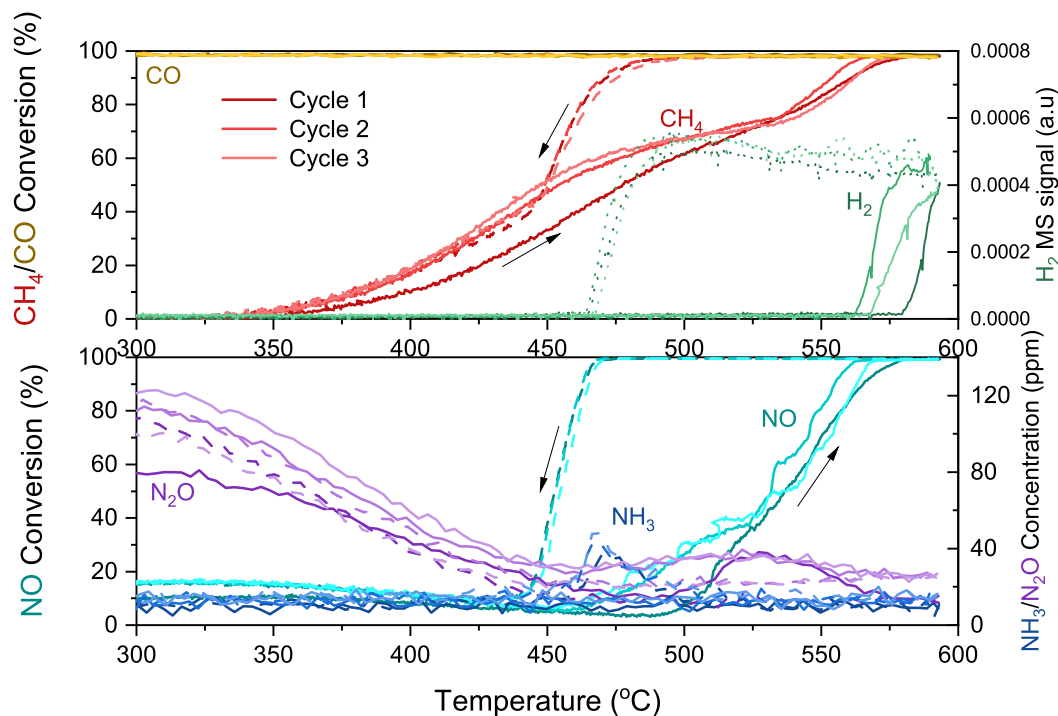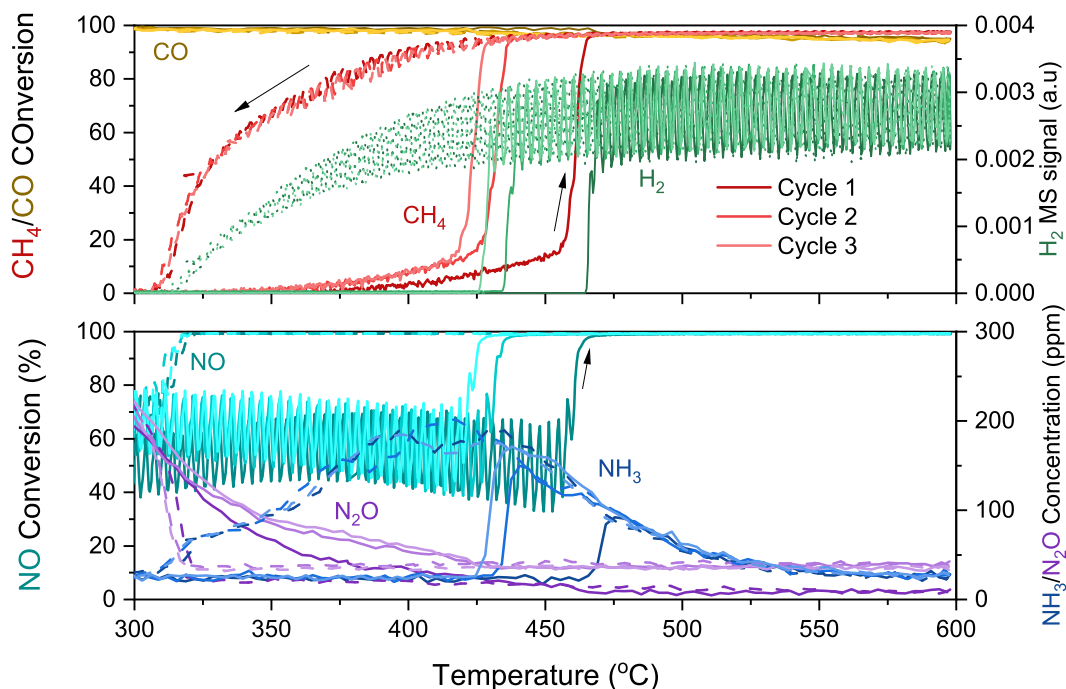

Figure 4.38: CO, CH_4 and NO conversion, H_2 MS signal and NH_3 and N_2O concentration during three temperature cycles of heating (——) and cooling (- - -) over **Rh/CZ** under optimized O_2 dithering conditions with $\lambda = 1 \pm 0.40$ at at a frequency of 0.05 Hz corresponding to 5 vol% H_2O, 0.15 vol% CH_4, 0.16 vol% NO, 0.7 vol% CO and 0.57 ± 0.143 vol% O_2 in Ar at a WHSV of 240 L h^{-1} g_{cat}^{-1}. The darker color corresponds to the first cycle and the lighter colors corresponds to the second and third cycle.

As in the case of Rh/A, the oscillations with a frequency of 0.05 Hz were large and also seemed

to delay the triggering of CH_4-SR due to the redox properties of Ce. The O_2 dithering conditions was optimized at 420 °C, and in an attempt to improve conversion at even lower temperatures, temperature ramps over Rh/CZ with the same amplitude of $\lambda = 1 \pm 0.40$, but with a higher frequency of 0.2 Hz was tested (Figure 4.39). The light-off temperature for cycle 1 when dithering at 0.05 Hz was 350 °C, under 0.2 Hz it had decreased to 325 °C where CH_4-SR seemed to be triggered already at 330 °C. After this point the catalyst never seemed to stop producing H_2, creating a net reducing atmosphere throughout the whole experiment. As mentioned previously NO reduction preferred net reducing conditions which was clearly observed over Rh/CZ, where after reaching maximum conversion at ca. 350 °C in cycle 1 it stayed converted through the rest of the cycles. As a consequence, N_2O was only produced in the first ramp up, but large amounts of NH_3 were detected with a maximum of 410 ppm during the heating ramp in cycle 1. This is the largest amount of NH_3 observed over any of the Rh-based catalysts in this study, which indicates that good conversions comes with a price. However, out of N_2O and NH_3, NH_3 is easier to remove with a possible oxidation catalyst downstream for both NH_3 and H_2 removal [24]. It is therefore better to work in rich conditions and produce NH_3 than lean/stoichiometric conditions and obtain N_2O. The enhanced activity over Rh/CZ with the higher frequency might be due to the shorter exposure time of the lean pulses possibly promoting reduction and making Rh/CZ the best catalyst in this work.
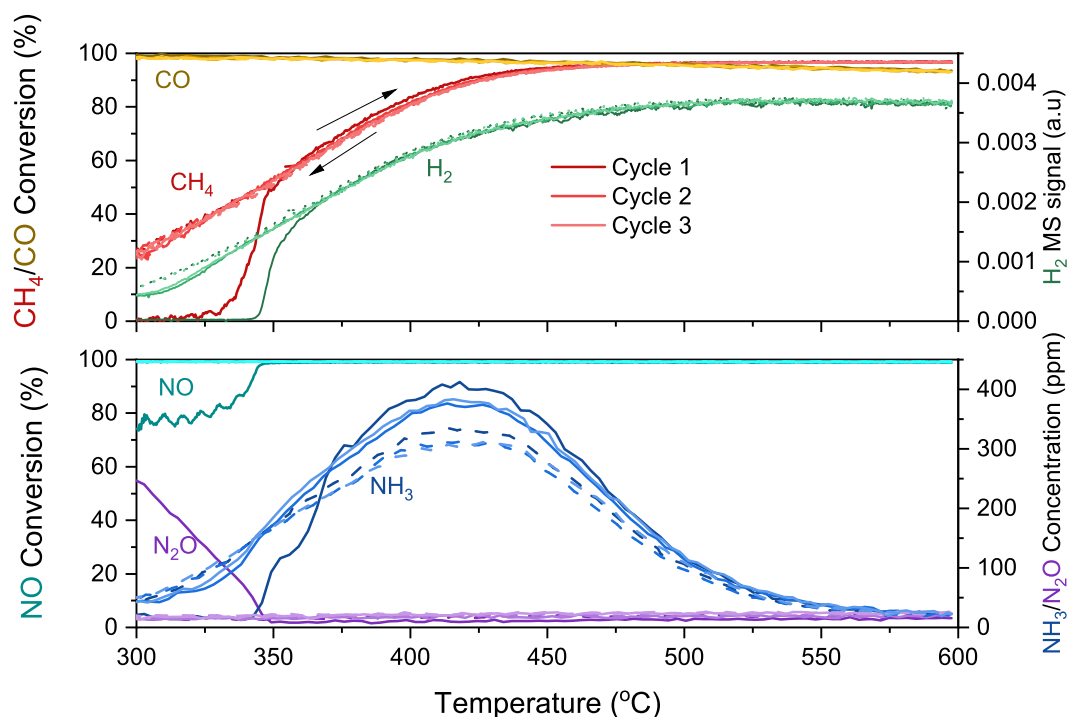
Figure 4.39: CO, CH_4 and NO conversion, H_2 MS signal and NH_3 and N_2O concentration during three temperature cycles of heating (——) and cooling (- - -) over **Rh/CZ** under optimized O_2 dithering conditions with $\lambda = 1 \pm 0.40$ at at a frequency of 0.2 Hz corresponding to 5 vol% H_2O, 0.15 vol% CH_4, 0.16 vol% NO, 0.7 vol% CO and 0.57 ± 0.143 vol% O_2 in Ar at a WHSV of 240 L h^{-1} $g_{cat.}^{-1}$. The darker color corresponds to the first cycle and the lighter colors corresponds to the second and third cycle.

As observed over the alumina-based samples, the effect of O_2 dithering under temperature ramps on the Pd-based samples resulted in great improvements, but not as remarkable as on the Rh-sample alone. Figure 4.40 illustrates the temperature ramp conducted on Pd-Rh/CZ under the optimized O_2 dithering conditions: $\lambda = 1 \pm 0.25$ at a frequency of 0.1 Hz. The results were similar to the behaviour obtained with Pd-Rh/A (Figure 4.25), just shifted to higher temperatures. The light-off temperature for all cycles was 350 °C, where CH_4-SR seemed to be triggered a few degrees higher at 381, 437 and 433 °C for cycle 1, 2 and 3 respectively. Usually, the start of CH_4-SR seemed to improve throughout the cycles, but in this case the ramp up for cycle 1 seemed to give the best results. An interesting observation is the shape of the CH_4 conversion for cycle 1 was different than the others and resembled the shape observed over Pd/A under optimized conditions where a deactivation throughout the cycles was also observed (Figure 4.24). Additionally, a higher conversion of CH_4 by O_2 is apparent in the same cycle, as well as a lower NO conversion, indicating that Pd was the most active metal in cycle 1. The sharp increase in CH_4 conversion once CH_4-SR

had been triggered in cycle 2 indicated that metallic Rh had been activated, where the typical improvement for the next cycle (cycle 3) was similar as Pd-Rh/A.
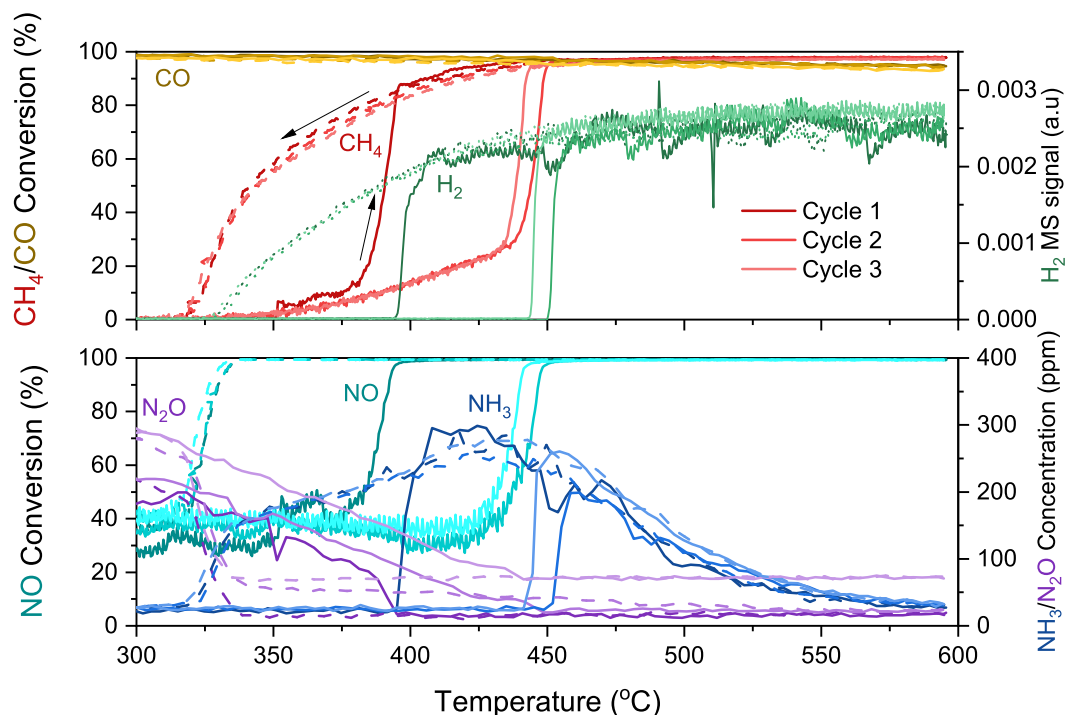
Figure 4.40: CO, CH_4 and NO conversion, H_2 MS signal and NH_3 and N_2O concentration during three temperature cycles of heating (——) and cooling (- - -) over **Pd-Rh/CZ** under optimized O_2 dithering conditions with $\lambda = 1 \pm 0.25$ at a frequency of 0.1 Hz corresponding to 5 vol% H_2O, 0.15 vol% CH_4, 0.16 vol% NO, 0.7 vol% CO and 0.57 ± 0.143 vol% O_2 in Ar at a WHSV of 240 L h^{-1} g_{cat}^{-1}. The darker color corresponds to the first cycle and the lighter colors corresponds to the second and third cycle.

Similar to Rh/A of the alumina-based samples, Rh/CZ clearly exhibited the best performance under the O_2 dithering conditions at higher frequencies. This was not under the frequency chosen from the optimization in Section 4.2.2.3 performed at 420 °C, but from the results of the temperature ramps over both CZ-based samples and alumina-based samples. It seems that higher frequencies promote conversion at lower temperatures [26]. It would therefore be worth a try to perform temperature ramps under O_2 dithering conditions at a 0.2 Hz frequency over Pd-Rh/CZ as well. Comparing the two Rh-samples, the superior performance of Rh/CZ was possible due to reduced ceria activating the H_2O for CH_4-SR [72], which also was observed in Section 4.2.2.2 where CZ promoted both CH_4-SR and WGS at richer conditions.

Chapter 5

Conclusion

This research investigated different catalytic materials under both static and dynamic conditions in order to trigger CH_4-SR at low temperatures over the three-way catalyst (TWC) to achieve full pollutant removal. During the project, Pd, Rh and bimetallic Pd-Rh supported on alumina and Rh and bimetallic Pd-Rh supported on CZ were prepared. The material in the catalysts were chosen based on their reported active sites for CH_4-SR.

The CZ support was synthesized through the coprecipitation method, where the active metals were deposited on the support by incipient wetness impregnation. The catalysts were characterized by XRD, N_2-physisorption, TEM, OSC, TPR, CO-DRIFT, XAS and ICP-OES. The catalytic activity was tested under stoichiometric temperature ramps after an oxidized pretreatment as well as reductive pretreatment and was further investigated through lambda sweeps as to study the impact of O_2 concentration present in the feed. Additionally, tests were carried out in order to find the optimal O_2 dithering condition for each catalyst which was then further investigated through activity temperature ramps.

Both preoxidized and prereduced Pd/A resulted in a negative hysteresis during the temperature ramps, whereas a positive hysteresis was observed on Pd-Rh/A. On Rh/A a positive hysteresis was observed after a reductive pretreatment which indicated that the positive hysteresis on Pd-Rh/A was due to the presence of Rh. This was further investigated using in situ XRD, where the Pd in Pd-Rh/A both oxidized and reduced more easily than Pd/A, indicating that Rh promotes the redox properties of Pd. Through IR experiments of CO adsorption together with a catalytic comparison with a Pd_Rh/A mechanical mixture, it is believed that in the bimetallic Pd-Rh sample, the Pd and Rh were alloyed. A deeper investigation by ex situ XAS during the hysteresis showed that reduced Pd was essential for high conversion due to the promotion of CH_4-SR. In contact with

reduced Rh, the Pd seemed to maintain the reduced state longer (c.f. lower temperature) which therefore led to a positive hysteresis.

The lambda sweeps showed that the CO-NO crossover point was shifted to richer conditions for all catalysts when the active materials were reduced. The catalysts were therefore exposed to a reductive pretreatment which improved the catalytic activity of the alumina-based samples, which, from XAS, was due to more reduced active metal being present at the start of the temperature ramps. The improvement was not observed over the CZ-based samples which was explained by O_2 back spillover from CZ to the metal, as observed in the TPR-profiles and the OSC measurements, which kept the metals in an oxidized state.

In general, Pd/A was the most active catalyst towards CH_4-SR under static stoichiometric conditions. However, changing to dynamic stoichiometric conditions seemed to be favorable for all catalysts, especially for Rh/CZ where CH_4-SR and full NO conversion were achieved already at 300 °C. In addition to the improved activity under dynamic conditions, the stability test revealed that catalysts exposed to dynamic conditions were less prone to sintering and deactivation.

The results revealed that Rh alone on a TWC is very active towards CH_4-SR when in its reduced form which was enhanced when it was supported on CZ as suggested by the lambda sweeps. While Rh seemed to suppress NH_3 production at high temperatures, NH_3 was formed at ca. 400 °C and must be taken into consideration in real life operation possibly by adding an oxidation catalyst downstream of the TWC for pollutant removal.

Chapter 6

Future Work

In this project the synthesized Pd:Rh ratio was 3:2, and as clearly induced a positive synergism between Pd and Rh. Since Rh is relatively expensive, it would be interesting to test different Pd:Rh ratios in order to evaluate the minimum amount of Rh needed to achieve a positive effect on CH_4 abatement. However, though a synergism was observed in the catalytic activity, in-situ XRD and CO-DRIFT results, together with the limitations accoutered by EDX mapping (overlap of the Pd and Rh emissions lines) it was difficult to the Pd and Rh particles were effectively alloyed. Therefore it would be of interest to perform EELS on the sample.

The ex situ XAS gave valuable information about the oxidation state on the alumina-based samples under static stoihciometric conditions. However, due to time restrictions, CZ-based samples were not analysed, where it would be interesting to see how reduced the active metals are after the reductive pretreatment and in the temperature ramps.

Furthermore, a Pd/CZ catalyst was missing from the CZ-based samples for comparison with both the alumina-based samples and Rh/CZ and Pd-Rh/CZ. As CZ promoted CH_4-SR and WGS under reduced conditions (same as Rh), it would be interesting to see if Pd/CZ would results in a positive hysteresis as Rh promoted over Pd-Rh/CZ.

After the stability tests, sintering was revealed on the sample exposed to static rich conditions, but deactivation was not detected while on stream. Under rich condition the catalyst showed stable conversion, similar to the catalyst under dynamic conditions (where no sintering was detected). To be able to distinguish a difference between the two, longer stability tests over a week or could be considered.

Based on the results obtained in this thesis, Rh/CZ exhibited the best pollutant removal under

O_2 dithering conditions. As mentioned, Rh is an expensive metal and it would therefore be of interest to synthesize Rh/CZ with different Rh loading to explore its effect on activity and on NH_3 production. A further optimization Could also be possible by testing different Ce/Zr ratios of the CZ-support. Finally an investigation by ex situ XAS at certain temperatures in the dynamic activity ramps would reveal the oxidation state of Rh and of Ce and Zr, deliver more insight to the high conversions during the O_2 dithering.

Bibliography

[1]   S. Siva Raju and K. Ahire, "Climate Change and Air Pollution in Mumbai," *Springer Climate*, no. 24, pp. 289–308, 2018, ISSN: 23520701. DOI: `10.1007/978-3-319-61346-8{\_}18`.

[2]   UNFCCC, "United Nations Framework Convention on Climate Change United Nations," *United Nations Frameork Convention on Climate Change*, pp. 1–33, 1992.

[3]   Climate Leaders, *What Is the UNFCCC and the COP?* 2009. [Online]. Available: `https://web.archive.org/web/20090327142028/http://www.climate-leaders.org/climate-change-resources/india-at-cop-15/unfccc-cop/[Accessed:02.09.2021]`.

[4]   R. Lindsey, *Cilimate Change: Atmospheric Carbon Dioxide*, 2020. [Online]. Available: `https://www.climate.gov/news-features/understanding-climate/climate-change-atmospheric-carbon-dioxide/[Accessed:02.09.2021]`.

[5]   O. Edenhofer, R. Pichs-Madruga, Y. Sokona, E. Farahani, S. Kadner, K. Seyboth, A. Adler, I. Baum, S. Brunner, P. Eickemeier, B. Kriemann, J. Savolainen, S. Schlömer, C. von Stechow, T. Zwickel, and J. Minx, "Contribution of Working Group III to the Fifth Assessment Report of the Intergovernmental Panel on Climate Change," Cambridge University Press, Cambridge, UK and New York, USA, Tech. Rep., 2014.

[6]   Natgas, *Natural Gas and the Environment*, 2013. [Online]. Available: `http://naturalgas.org/environment/naturalgas/[Accessed:04.04.2021]`.

[7]   A. Raj, "Methane emission control," *Johnson Matthey Technology Review*, vol. 60, no. 4, pp. 228–235, 2016.

[8]   D. Bounechada, G. Groppi, P. Forzatti, K. Kallinen, and T. Kinnunen, "Effect of periodic lean/rich switch on methane conversion over a Ce-Zr promoted Pd-Rh/Al 2O 3 catalyst in the exhausts of natural gas vehicles," *Applied Catalysis B: Environmental*, vol. 119-120, pp. 91–99, 2012.

[9]   J. G. Speight, "6 - Gasification processes for syngas and hydrogen production," in *Gasification for Synthetic Fuel Production*, ser. Woodhead Publishing Series in Energy, R. Luque and J. G. Speight, Eds., Woodhead Publishing, 2015, pp. 119–146.

[10] Advanced Motor Fuels Technology Collaboration Programme, *Methane (Natural Gas, Biomethane)*, 2021.

[11] OECD, *Promoting Clean Urban Public Transportation and Green Investment in Moldova*, ser. Green Finance and Investment. Paris: OECD Publishing, Sep. 2019.

[12] Etter Engineering, *Methane Abatement*, 2021.

[13] P. Lott and O. Deutschmann, "Lean-Burn Natural Gas Engines: Challenges and Concepts for an Efficient Exhaust Gas Aftertreatment System," *Emission Control Science and Technology*, no. x, pp. 1–6, 2020.

[14] J. Parks, "Emissions Control for Natural Gas Fueld Trucks," Tech. Rep., 2017. [Online]. Available: `https://cleancities.energy.gov/files/u/news_events/document/document_url/297/Emissions_Control_for_Natural_Gas_Fueled_Trucks.pdf/` `[Accessed:11.08.21]`.

[15] Walker, *Evolution Of Catalytic Converter*, 2021. [Online]. Available: `https://matthey.com/en/products-and-services/emission-control-technologies/mobile-emissions-control-1/three-way-catalysts/` `[Accessed:11.08.21]`.

[16] A. Trovarelli, *Catalysis by ceria and related materials*. 2005, vol. 2, p. 508.

[17] Y. Cao, R. Ran, X. Wu, X. Wu, J. Wan, and D. Weng, "Ageing resistance of rhodium supported on CeO2–ZrO2 and ZrO2: Rhodium nanoparticle structure and Rh–support interaction under diverse ageing atmosphere," *Catalysis Today*, vol. 281, pp. 490–499, 2017.

[18] R. M. Heck, R. J. Farrauto, and S. T. Gulati, *Catalytic Air Pollution Control*, 3rd. New York: Wiley-Interscience, 2009.

[19] C. Huang, W. Shan, Z. Lian, Y. Zhang, and H. He, "Recent advances in three-way catalysts of natural gas vehicles," *Catalysis Science and Technology*, vol. 10, no. 19, pp. 6407–6419, 2020.

[20] T. Franken, M. Roger, A. W. Petrov, A. H. Clark, M. Agote-ar, F. Krumeich, O. Kr, and D. Ferri, "Effect of Short Reducing Pulses on the Dynamic Structure, Activity, and Stability of Pd/Al 2 O 3 for Wet Lean Methane Oxidation," 2021.

[21] P. Lott, P. Dolcet, M. Casapu, J. D. Grunwaldt, and O. Deutschmann, "The effect of prereduction on the performance of pd/al2o3 and pd/ceo2 catalysts during methane oxidation," *Industrial and Engineering Chemistry Research*, vol. 58, no. 28, pp. 12 561–12 570, 2019.

[22] C. Bozo, N. Guilhaume, and J. M. Herrmann, "Role of the ceria-zirconia support in the reactivity of platinum and palladium catalysts for methane total oxidation under lean conditions," *Journal of Catalysis*, vol. 203, no. 2, pp. 393–406, 2001.

[23] M. Salaün, S. Capela, S. Da Costa, L. Gagnepain, and P. Da Costa, "Enhancement of 3-way CNG catalyst performance at high temperature due to the presence of water in the feed: On the role of steam reforming of methane and on the influence of ageing," *Topics in Catalysis*, vol. 52, no. 13-20, pp. 1972–1976, 2009.

[24] M. Wang, P. Dimopoulos Eggenschwiler, T. Franken, D. Ferri, and O. Kröcher, "Reaction pathways of methane abatement in Pd-Rh three-way catalyst in heavy duty applications: A combined approach based on exhaust analysis, model gas reactor and DRIFTS measurements," *Chemical Engineering Journal*, vol. 422, 2021.

[25] M. Salaün, A. Kouakou, S. Da Costa, and P. Da Costa, "Synthetic gas bench study of a natural gas vehicle commercial catalyst in monolithic form: On the effect of gas composition," *Applied Catalysis B: Environmental*, vol. 88, no. 3-4, pp. 386–397, 2009.

[26] J. Gong, J. Pihl, D. Wang, M. Y. Kim, W. P. Partridge, J. Li, M. Cunningham, K. Kamasamudram, N. Currier, and A. Yezerets, "O2 dosage as a descriptor of TWC performance under lean/rich dithering in stoichiometric natural gas engines," *Catalysis Today*, vol. 360, no. January 2020, pp. 294–304, 2021.

[27] D. Ferri, M. Elsener, and O. Kröcher, "Methane oxidation over a honeycomb Pd-only three-way catalyst under static and periodic operation," *Applied Catalysis B: Environmental*, vol. 220, pp. 67–77, 2018.

[28] Y. Renème, F. Dhainaut, and P. Granger, "Kinetics of the NO/H 2/O 2 reactions on natural gas vehicle catalysts-Influence of Rh addition to Pd," *Applied Catalysis B: Environmental*, vol. 111-112, no. x, pp. 424–432, 2012.

[29] P. Granger, C. Dujardin, J. F. Paul, and G. Leclercq, "An overview of kinetic and spectroscopic investigations on three-way catalysts: Mechanistic aspects of the CO + NO and CO + N2O reactions," *Journal of Molecular Catalysis A: Chemical*, vol. 228, pp. 241–253, 2005.

[30] F. Rodriguez and J. Dornoff, "Beyond NOx: Emission of unregulated pollutants from a modern gasoline car.," *International Council of Clean Transport*, no. X, 2019.

[31] P. Nevalainen, N. M. Kinnunen, A. Kirveslahti, K. Kallinen, T. Maunula, M. Keenan, and M. Suvanto, "Formation of NH3 and N2O in a modern natural gas three-way catalyst designed for heavy-duty vehicles: the effects of simulated exhaust gas composition and ageing," *Applied Catalysis A: General*, vol. 552, no. December 2017, pp. 30–37, 2018.

[32] H. S. Gandhi, G. W. Graham, and R. W. McCabe, "Automotive exhaust catalysis," *Journal of Catalysis*, vol. 216, no. 1-2, pp. 433–442, 2003.

[33] G. Beulertz, M. Votsmeier, and R. Moos, "Effect of propene, propane, and methane on conversion and oxidation state of three-way catalysts: A microwave cavity perturbation study," *Applied Catalysis B: Environmental*, vol. 165, pp. 369–377, 2015.

[34] H. Jääskeläinen, "Three Way Catalysts for Methane," *DieselNet*, 2017.

[35] X. Shi, R. Seiser, J. Y. Chen, R. Dibble, and R. Cattolica, "Fuel-Dithering Optimization of Efficiency of TWC on Natural Gas IC Engine," *SAE International Journal of Engines*, vol. 8, no. 3, pp. 1246–1252, 2015.

[36] T. Baldwin and R. Burch, "Catalytic Combustion of Methane over Supported Palladium Catalysts. I. Alumina Supported Catalysts," *Appl. Catal.*, vol. 66, pp. 337–358, 1990.

[37] K. I. Fujimoto, F. H. Ribeiro, M. Avalos-Borja, and E. Iglesia, "Structure and reactivity of PdOx/ZrO2 catalysts for methane oxidation at low temperatures," *Journal of Catalysis*, vol. 179, no. 2, pp. 431–442, 1998.

[38] W. Epling and G. Hoflund, "Catalytic Oxidation of Methane over ZrO2-Supported Pd Catalysts," *J.Catal.*, vol. 182, pp. 5–12, 1999.

[39] D. Ciuparu, M. R. Lyubovsky, E. Altman, L. D. Pfefferle, and A. Datye, "Catalytic combustion of methane over palladium-based catalysts," *Catalysis Reviews - Science and Engineering*, vol. 44, no. 4, pp. 593–649, 2002.

[40] R. W. Howarth, "A bridge to nowhere: Methane emissions and the greenhouse gas footprint of natural gas," *Energy Science and Engineering*, vol. 2, no. 2, pp. 47–60, 2014.

[41] Z. P. Liu and P. Hu, "General rules for predicting where a catalytic reaction should occur on metal surfaces: A density functional theory study of C-H and C-O bond breaking/making on flat, stepped, and kinked metal surfaces," *Journal of the American Chemical Society*, vol. 125, no. 7, pp. 1958–1967, 2003.

[42] Z. Zhu, G. Lu, Y. Guo, Y. Guo, Z. Zhang, and Y. Wang, "Influences of Pd precursors and preparation method on the catalytic performances of Pd-only close-coupled catalysts," *Journal of Industrial and Engineering Chemistry*, vol. 18, no. 6, pp. 2135–2140, 2012.

[43] S. Lin, L. Yang, X. Yang, and R. Zhou, "The effect of Pd precursor on Pd/Ce0.67Zr0.33O2 catalysts for automotive emission control," *Cuihua Xuebao/Chinese Journal of Catalysis*, vol. 36, no. 4, pp. 639–648, 2015.

[44] D. Roth, P. Gélin, M. Primet, and E. Tena, "Catalytic behaviour of Cl-free and Cl-containing Pd/Al2O3 catalysts in the total oxidation of methane at low temperature," *Applied Catalysis A: General*, vol. 203, no. 1, pp. 37–45, 2000.

[45] R. J. Farrauto, M. C. Hobson, T. Kennelly, and E. M. Waterman, "Catalytic chemistry of supported palladium for combustion of methane," *Applied Catalysis A, General*, vol. 81, no. 2, pp. 227–237, 1992.

[46] A. K. Datye, J. Bravo, T. R. Nelson, P. Atanasova, M. Lyubovsky, and L. Pfefferle, "Catalyst microstructure and methane oxidation reactivity during the PdPdO transformation on alumina supports," *Applied Catalysis A: General*, vol. 198, no. 1-2, pp. 179–196, 2000.

[47] F. Huang, J. Chen, W. Hu, G. Li, Y. Wu, S. Yuan, L. Zhong, and Y. Chen, "Pd or PdO: Catalytic active site of methane oxidation operated close to stoichiometric air-to-fuel for natural gas vehicles," *Applied Catalysis B: Environmental*, vol. 219, pp. 73–81, 2017.

[48] M. Monai, T. Montini, R. J. Gorte, and P. Fornasiero, "Catalytic Oxidation of Methane: Pd and Beyond," *European Journal of Inorganic Chemistry*, vol. 2018, no. 25, pp. 2884–2893, 2018.

[49] Y. H. C. Chin, M. García-Diéguez, and E. Iglesia, "Dynamics and thermodynamics of Pd-PdO phase transitions: Effects of pd cluster size and kinetic implications for catalytic methane combustion," *Journal of Physical Chemistry C*, vol. 120, no. 3, pp. 1446–1460, 2016.

[50] M. Machida, S. Minami, S. Hinokuma, H. Yoshida, Y. Nagao, T. Sato, and Y. Nakahara, "Unusual redox behavior of Rh/AlPO4 and its impact on three-way catalysis," *Journal of Physical Chemistry C*, vol. 119, no. 1, pp. 373–380, 2015.

[51] A. Srinivasan and C. Depcik, "Review of Chemical Reactions in the NO Reduction by CO on Rhodium / Alumina Catalysts Review of Chemical Reactions in the NO Reduction by CO on Rhodium / Alumina Catalysts," vol. 4940, 2010.

[52] J. Ohyama, T. Nishiyama, and A. Satsuma, "Formation of Rhodium Metal Ensembles that Facilitate Nitric Oxide Reduction over Rhodium/Ceria in a Stoichiometric Nitric Oxide–Carbon Monoxide–Propene–Oxygen Reaction," *ChemCatChem*, vol. 10, no. 7, pp. 1651–1656, 2018.

[53] T. Maillet, J. Barbier, D. Duprez, P. Gelin, and H. Praliaud, "Effects of pretreatments on the surface composition of alumina-supported Pd-Rh catalysts," *Journal of Catalysis*, vol. 202, no. 2, pp. 367–378, 2001.

[54] T. P. Kobylinski and B. W. Taylor, "The catalytic chemistry of nitric oxide. II. Reduction of nitric oxide over noble metal catalysts," *Journal of Catalysis*, vol. 33, no. 3, pp. 376–384, 1974.

[55] D. Na-Ranong, R. Yuangsawad, P. Kitchaiya, and T. Aida, "Application of periodic operation to kinetic study of NO-CO reaction over Rh/Al2O3," *Chemical Engineering Journal*, vol. 146, no. 2, pp. 275–286, 2009.

[56] D. A. Ligthart, R. A. Van Santen, and E. J. Hensen, "Influence of particle size on the activity and stability in steam methane reforming of supported Rh nanoparticles," *Journal of Catalysis*, vol. 280, no. 2, pp. 206–220, 2011.

[57] M. H. Halabi, M. H. De Croon, J. Van Der Schaaf, P. D. Cobden, and J. C. Schouten, "Low temperature catalytic methane steam reforming over ceria-zirconia supported rhodium," *Applied Catalysis A: General*, vol. 389, no. 1-2, pp. 68–79, 2010.

[58] Y. Renème, F. Dhainaut, M. Trentesaux, B. Ravanbakhsh, P. Granger, C. Dujardin, L. Gengembre, and P. L. De Cola, "XPS investigation of surface changes during thermal aging of natural gas vehicle catalysts: Influence of Rh addition to Pd," *Surface and Interface Analysis*, vol. 42, no. 6-7, pp. 530–535, 2010.

[59] Y. Renème, F. Dhainaut, Y. Schuurman, C. Mirodatos, and P. Granger, "Comparative surface analysis and TAP measurements to probe the NO adsorptive properties of natural gas vehicle Pd-Rh/Al2O3 catalyst," *Applied Catalysis B: Environmental*, vol. 160-161, no. 1, pp. 390–399, 2014.

[60] P. Granger, Y. Renème, F. Dhainaut, Y. Schuurman, and C. Mirodatos, "NO Adsorption and Reaction on Aged Pd–Rh Natural Gas Vehicle Catalysts: A Combined TAP and Steady-State Kinetic Approach," *Topics in Catalysis*, vol. 60, no. 3-5, pp. 289–294, 2017.

[61] A. A. Vedyagin, V. O. Stoyanovskii, P. E. Plyusnin, Y. V. Shubin, E. M. Slavinskaya, and I. V. Mishakov, "Effect of metal ratio in alumina-supported Pd-Rh nanoalloys on its performance in three way catalysis," *Journal of Alloys and Compounds*, vol. 749, pp. 155–162, 2018.

[62] A. A. Vedyagin, A. M. Volodin, R. M. Kenzhin, V. O. Stoyanovskii, Y. V. Shubin, P. E. Plyusnin, and I. V. Mishakov, "Effect of metal-metal and metal-support interaction on activity and stability of Pd-Rh/alumina in CO oxidation," *Catalysis Today*, vol. 293-294, pp. 73–81, 2017.

[63] M. Machida, Y. Uchida, Y. Ishikawa, S. Hinokuma, H. Yoshida, J. Ohyama, Y. Nagao, Y. Endo, K. Iwashina, and Y. Nakahara, "Thermostable Rh Metal Nanoparticles Formed on Al2O3 by High-Temperature H2 Reduction and Its Impact on Three-Way Catalysis," *Journal of Physical Chemistry C*, vol. 123, no. 40, pp. 24 584–24 591, 2019.

[64] Z. Hu, F. M. Allen, C. Z. Wan, R. M. Heck, J. J. Steger, R. E. Lakis, and C. E. Lyman, "Performance and structure of Pt-Rh three-way catalysts: Mechanism for Pt/Rh synergism," *Journal of Catalysis*, vol. 174, no. 1, pp. 13–21, 1998.

[65] Z. Weng-Sieh, R. Gronsky, and A. T. Bell, "Effects of support interaction on the phase stability of Rh oxides formed during the aging of α-alumina supported Rh in air," *Journal of Catalysis*, vol. 174, no. 1, pp. 22–33, 1998.

[66] C. P. Hwang, C. T. Yeh, and Q. Zhu, "Rhodium-oxide species formed on progressive oxidation of rhodium clusters dispersed on alumina," *Catalysis Today*, vol. 51, no. 1, pp. 93–101, 1999.

[67] H. Yao, S. Japar, and M. Shelef, "Surface Interactions in the System Rh/Al2O3," *Journal of Catalysis*, no. 50, pp. 407–418, 1977.

[68] R. Polvinen, M. Vippola, M. Valden, T. Lepistö, A. Suopanki, and M. Härkönen, "The effect of Pt-Rh synergism on the thermal stability of rhodium oxide on pure alumina and Ce-ZrO2-modified alumina-supported catalysts," *Journal of Catalysis*, vol. 226, no. 2, pp. 372–381, 2004.

[69] K. Dohmae, Y. Nagai, T. Tanabe, A. Suzuki, Y. Inada, and M. Nomura, "Real-time XAFS analysis of Rh/alumina catalyst," *Surface and Interface Analysis*, vol. 40, no. 13, pp. 1751–1754, 2008.

[70] I. Chorkendorff and J. Niemantsverdriet, *Concept of Modern Catalysis and Kinetics*, 2nd. Wiley-CHF, 2007.

[71] J. Kašpar, P. Fornasiero, and N. Hickey, "Automotive catalytic converters: Current status and some perspectives," *Catalysis Today*, vol. 77, no. 4, pp. 419–449, 2003.

[72] R. B. Duarte, O. V. Safonova, F. Krumeich, M. Makosch, and J. A. V. Bokhoven, "Oxidation State of Ce in CeO 2 - Promoted Rh / Al 2 O 3 Catalysts during Methane Steam Reforming : H 2 O Activation and Alumina Stabilization," 2013.

[73] P. P. Silva, F. A. Silva, L. S. Portela, L. V. Mattos, F. B. Noronha, and C. E. Hori, "Effect of Ce/Zr ratio on the performance of Pt/CeZrO2/Al 2O3 catalysts for methane partial oxidation," *Catalysis Today*, vol. 107-108, pp. 734–740, 2005.

[74] L. S. Feio, C. E. Hori, S. Damyanova, F. B. Noronha, W. H. Cassinelli, C. M. Marques, and J. M. Bueno, "The effect of ceria content on the properties of Pd/CeO2/Al2O3 catalysts for steam reforming of methane," *Applied Catalysis A: General*, vol. 316, no. 1, pp. 107–116, 2007.

[75] S. Colussi, A. Trovarelli, C. Cristiani, L. Lietti, and G. Groppi, "The influence of ceria and other rare earth promoters on palladium-based methane combustion catalysts," *Catalysis Today*, vol. 180, no. 1, pp. 124–130, 2012.

[76] I. V. Yentekakis, G. Goula, M. Hatzisymeon, I. Betsi-Argyropoulou, G. Botzolaki, K. Kousi, D. I. Kondarides, M. J. Taylor, C. M. Parlett, A. Osatiashtiani, G. Kyriakou, J. P. Holgado, and R. M. Lambert, "Effect of support oxygen storage capacity on the catalytic performance of Rh nanoparticles for CO2 reforming of methane," *Applied Catalysis B: Environmental*, vol. 243, no. October 2018, pp. 490–501, 2019.

[77] D. Terribile, A. Trovarelli, J. Llorca, C. De Leitenburg, and G. Dolcetti, "The synthesis and characterization of mesoporous high-surface area ceria prepared using a hybrid organic/inorganic route," *Journal of Catalysis*, vol. 178, no. 1, pp. 299–308, 1998.

[78] M. Fernández-García, A. Martínez-Arias, A. Iglesias-Juez, C. Belver, A. B. Hungría, J. C. Conesa, and J. Soria, "Structural characteristics and redox behavior of CeO2-ZrO2/Al2O3 supports," *Journal of Catalysis*, vol. 194, no. 2, pp. 385–392, 2000.

[79] P. P. Silva, F. A. Silva, H. P. Souza, A. G. Lobo, L. V. Mattos, F. B. Noronha, and C. E. Hori, "Partial oxidation of methane using Pt/CeZrO2/Al 2O3 catalysts - Effect of preparation methods," *Catalysis Today*, vol. 101, no. 1, pp. 31–37, 2005.

[80] T. Murota, T. Hasegawa, S. Aozasa, H. Matsui, and M. Motoyama, "Production method of cerium oxide with high storage capacity of oxygen and its mechanism," *J. Alloys and Comp.*, vol. 193, pp. 298–299, 1993.

[81] C. D. Leitenburg, D. Goi, A. Primavera, A. Trovarelli, and G. Dolcetti, "Wet oxidation of acetic acid catalyzed by doped ceria," *Appl. Catal. B: Env*, vol. 11, pp. 29–35, 1996.

[82] G. Balducci, J. Kašpar, P. Fornasiero, M. Graziani, M. S. Islam, and J. D. Gale, "Computer simulation studies of bulk reduction and oxygen migration in CeO2-ZrO2 solid solutions," *Journal of Physical Chemistry B*, vol. 101, no. 10, pp. 1750–1753, 1997.

[83] F. B. Noronha, E. C. Fendley, R. R. Soares, W. E. Alvarez, and D. E. Resasco, "Correlation between catalytic activity and support reducibility in the CO2 reforming of methane over Pt/CeχZr1-χO2 catalysts," *Chemical Engineering Journal*, vol. 82, no. 1-3, pp. 21–31, 2001.

[84] S. Letichevsky, C. A. Tellez, R. R. De Avillez, M. I. P. Da Silva, M. A. Fraga, and L. G. Appel, "Obtaining CeO2-ZrO2 mixed oxides by coprecipitation: Role of preparation conditions," *Applied Catalysis B: Environmental*, vol. 58, no. 3-4, pp. 203–210, 2005.

[85] E. Aneggi, C. De Leitenburg, and A. Trovarelli, "On the role of lattice/surface oxygen in ceria-zirconia catalysts for diesel soot combustion," *Catalysis Today*, vol. 181, no. 1, pp. 108–115, 2012.

[86] T. Tsoncheva, R. Ivanova, J. Henych, M. Dimitrov, M. Kormunda, D. Kovacheva, N. Scotti, V. D. Santo, and V. Štengl, "Effect of preparation procedure on the formation of nanostructured ceria-zirconia mixed oxide catalysts for ethyl acetate oxidation: Homogeneous precipitation with urea vs template-assisted hydrothermal synthesis," *Applied Catalysis A: General*, vol. 502, pp. 418–432, 2015.

[87] Y. Liu, C. Wen, Y. Guo, G. Lu, and Y. Wang, "Modulated CO oxidation activity of M-doped ceria (M = Cu, Ti, Zr, and Tb): Role of the pauling electronegativity of M," *Journal of Physical Chemistry C*, vol. 114, no. 21, pp. 9889–9897, 2010.

[88] M. Thammachart, V. Meeyoo, T. Risksomboon, and S. Osuwan, "Catalytic activity of CeO2-ZrO2 mixed oxide catalysts prepared via sol-gel technique: CO oxidation," English, *Catalysis Today*, vol. 68, no. 1-3, pp. 53–61, 2001.

[89] M. Alifanti, B. Baps, N. Blangenois, J. Naud, P. Grange, and B. Delmon, "Characterization of CeO2-ZrO2 mixed oxides. Comparison of the citrate and sol-gel preparation methods," *Chemistry of Materials*, vol. 15, no. 2, pp. 395–403, 2003.

[90] J. Li, X. Liu, W. Zhan, Y. Guo, Y. Guo, and G. Lu, "Preparation of high oxygen storage capacity and thermally stable ceria-zirconia solid solution," *Catalysis Science and Technology*, vol. 6, no. 3, pp. 897–907, 2016.

[91] R. Di Monte and J. Kašpar, "On the role of oxygen storage in three-way catalysis," *Topics in Catalysis*, vol. 28, no. 1-4, pp. 47–58, 2004.

[92] J. R. Sietsma, A. Jos van Dillen, P. E. de Jongh, and K. P. de Jong, "Application of ordered mesoporous materials as model supports to study catalyst preparation by impregnation and drying," *Studies in Surface Science and Catalysis*, vol. 162, pp. 95–102, 2006.

[93] U. Rashid, S. Soltani, S. I. Al-Resayes, and I. A. Nehdi, *Metal oxide catalysts for biodiesel production*. Elsevier Inc., 2018, pp. 303–319.

[94] E. Marceau, X. Carrier, and M. Che, "Impregnation and Drying," in *Synthesis of Solid Catalysts*, John Wiley & Sons, Ltd, 2009, pp. 59–82.

[95] C. H. Bartholomew and R. J. Farrauto, *Fundamentals of Industrial Catalytic Processes*, 2nd. John Wiley & Sons, Ltd, 2005.

[96] CSIR-NAL, *Co-Precipitaion*, 2020. [Online]. Available: `nal.res.in/en/techniques/co-precipitation/[Acsessed:04.06.21]`.

[97] M. Lok, "Coprecipitation," in *Synthesis of Solid Catalysts*, John Wiley & Sons, Ltd, 2009, pp. 135–151.

[98] M. Nawaz, Y. Sliman, I. Ercan, M. K. Lima-Tenório, E. T. Tenório-Neto, C. Kaewsaneha, and A. Elaissari, *Magnetic and pH-responsive magnetic nanocarriers.* Elsevier Ltd., 2018, pp. 37–85.

[99] A. Baiker and M. Kohler, "Characterization of Catalyst," in *Handbook of Heat and Mass Tranfer, vol. 3*, Houston: Gulf Publishing, 1989, ch. 1, pp. 3–62.

[100] S. L. Bergman, J. Granestrand, S. Xi, Y. Du, Y. Tang, C. Tang, and K. Eds, "Probing the Oxidation / Reduction dynamics of Fresh and P / Na / K-contaminated Pt / Pd / Al2O3 Diesel Oxidation Catalysts by STEM , TPR and in-situ XANES STEM micrograph of potassium contaminated catalyst , along with EDS images of catalyst in areas with," no. Area 1, pp. 1–3,

[101] Gas Adsorption Technology, *Adsorption Equilibrium*, 2016. [Online]. Available: `https://gasadsorptiontech.wordpress.com/tag/adsorption-isotherm-types/[Accessed:17.09.20]`.

[102] Micromeritics, *Gas Adsorption Theory*, 2011. [Online]. Available: `https://www.micromeritics.com/Repository/Files/Gas_Adsorption_Theory_poster.pdf/[Accessed:13.08.2021]`.

[103] J. Niemantsverdriet, *Spectroscopy in Catalysis*, 3rd. Weinheim: Wiley-VCH, 2007.

[104] A. Nanakoudis, *EDX Analysis with SEM: How does it work?* 2019. [Online]. Available: `https://www.thermofisher.com/blog/microscopy/edx-analysis-with-sem-how-does-it-work/[Accessed:04.12.20]`.

[105] Hiden Analytical, *Temperature Programmed Reduction (TPR) - A Guide*, 2019. [Online]. Available: `https://www.azom.com/article.aspx?ArticleID=15889/[Accessed:04.12.20]`.

[106] "Temperature programmed reduction and sulphiding," in *Studies in Surface Science and Catalysis*, C, J. Moulijn, P. van Leeuwen, and R. van Santen, Eds., vol. 79, Elsevier, Jan. 1993, pp. 401–417.

[107] Y. Sun, C. Li, I. Djerdj, O. Khalid, P. Cop, J. Sann, T. Weber, S. Werner, K. Turke, Y. Guo, B. M. Smarsly, and H. Over, "Catalysis Science & Technology Oxygen storage capacity versus catalytic activity of ceria – zirconia solid solutions in CO and HCl oxidation †," pp. 2163–2172, 2019.

[108] P. Li, X. Chen, Y. Li, and J. W. Schwank, "A review on oxygen storage capacity of CeO 2 -based materials : In fl uence factors , measurement techniques , and applications in reactions related to catalytic automotive emissions control," *Catalysis Today*, vol. 327, no. February 2018, pp. 90–115, 2019.

[109] H. J. Sedjame, C. Fontaine, G. Lafaye, and J. Barbier, "On the promoting effect of the addition of ceria to platinum based alumina catalysts for VOCs oxidation," *Applied Catalysis B: Environmental*, vol. 144, no. 1, pp. 233–242, 2014.

[110] M. Boaro, F. Giordano, S. Recchia, V. D. Santo, M. Giona, and A. Trovarelli, "On the mechanism of fast oxygen storage and release in ceria-zirconia model catalysts," *Applied Catalysis B: Environmental*, vol. 52, no. 3, pp. 225–237, 2004.

[111] P. Larkin, "Instrumentation and Sampling Methods," *Infrared and Raman Spectroscopy*, pp. 27–54, 2011.

[112] M. B. Mitchell, "Fundamentals and Applications of Diffuse Reflectance Infrared Fourier Transform (DRIFT) Spectroscopy," pp. 351–375, 1993.

[113] ThermoFisher, *FTIR Sample Techniques - Diffuse Reflectance (DRIFT)*, 2021. [Online]. Available: `https://www.thermofisher.com/ch/en/home/industrial/spectroscopy-elemental-isotope-analysis/spectroscopy-elemental-isotope-analysis-learning-center/molecular-spectroscopy-information/ftir-information/ftir-sample-handling-techniques/ftir-sample-handling-tec`.

[114] J. A. Lercher and A. Jentys, "Chapter 13 Infrared and raman spectroscopy for characterizing zeolites," *Studies in Surface Science and Catalysis*, vol. 168, pp. 435–476, 2007.

[115] C. Kuo, Y. Lu, X. Zhang, and A. Karim, *High CO Oxidation Activity on Pt Single Atoms and Clusters Supported on MgAl2O4*, 2017. [Online]. Available: `https://www.aiche.org/conferences/aiche-annual-meeting/2017/proceeding/paper/127d-high-co-oxidation-activity-on-pt-single-atoms-and-clusters-supported-on-mgal2o4%5C/` `[Accessed:02.09.21]`.

[116] X. Wang, H. Shi, J. H. Kwak, and J. Szanyi, "Mechanism of CO2 Hydrogenation on Pd/Al2O3 Catalysts: Kinetics and Transient DRIFTS-MS Studies," *ACS Catalysis*, vol. 5, no. 11, pp. 6337–6349, 2015.

[117] J. Niemantsverdriet, "Microscopy and Imaging," in *Spectroscopy in Catalysis*, John Wiley & Sons, Ltd, 2007, ch. 7, pp. 179–216.

[118] Chemistry LibreTexts, *XAS - Theory*, 2021. [Online]. Available: `https://chem.libretexts.org/@go/page/1871/[Accessed:01.09.2021]`.

[119] F. Pilger, "Advanced Nanopowder Synthesis : Characterization , Performance and Kinetics of CeO2-based Supports , Catalysts and Segregation Processes PAR," Ph.D. dissertation, Lausanne, EPFL, 2017.

[120] Agilent, *ICP-OES Frequently Asked Questions*, 2021. [Online]. Available: `https://www.agilent.com/en/support/atomic-spectroscopy/inductively-coupled-plasma-optical-emission-spectroscopy-icp-oes/icp-oes-instruments/icp-oes-faq/` `[Accessed:01.09.2021]`.

[121] W. Majewski, "Emission Control Catalysts," *DieselNet Technology Guide*, 2012.

[122] R. Sindhu, P. Binod, and A. Pandey, *Microbial Poly-3-Hydroxybutyrate and Related Copoly-mers.* Elsevier B.V., 2015, pp. 575–605.

[123] A. Barhoum, M. L. García-Betancourt, H. Rahier, and G. Van Assche, *Physicochemical characterization of nanomaterials: Polymorph, composition, wettability, and thermal stability.* Elsevier Inc., 2018, pp. 255–278.

[124] A. Dutta, *Fourier Transform Infrared Spectroscopy.* Elsevier Inc., 2017, vol. 2, pp. 73–93.

[125] Broad Institute, *What is Mass Spectrometry*, 2021. [Online]. Available: `https://www.broadinstitute.org/technology-areas/what-mass-spectrometry/[Accessed:21.09.21]`.

[126] H. Perreault and E. Lattová, *Mass Spectrometry*, Second Edi. Elsevier B.V., 2011, vol. 1, pp. 669–677.

[127] InProcess Instruments, "Gas Analyse System GAM 400," InProcess Instruments, Tech. Rep., 2011.

[128] Pfeiffer Vacuum, *Quadrupole Mass Filter*, 2021. [Online]. Available: `https://www.pfeiffer-vacuum.com/en/know-how/mass-spectrometers-and-residual-gas-analysis/quadrupole-mass-spectrometers-qms/quadrupole-mass-filter/[Accsessed:21.09.2021]`.

[129] E. d. Hoffmann and V. Stroobant, *Mass spectrometry : principles and applications.* English. Chichester; New York: Wiley, 2001.

[130] F. A. Lima, M. E. Saleta, R. J. Pagliuca, M. A. Eleotério, R. D. Reis, J. F. Júnior, B. Meyer, E. M. Bittar, N. M. Souza-Neto, and E. Granado, "XDS: A flexible beamline for X-ray diffraction and spectroscopy at the Brazilian synchrotron," *Journal of Synchrotron Radiation*, vol. 23, no. 6, pp. 1538–1549, 2016.

[131] P. Serna, D. Yardimci, J. D. Kistler, and B. C. Gates, "Formation of supported rhodium clusters from mononuclear rhodium complexes controlled by the support and ligands on rhodium," *Physical Chemistry Chemical Physics*, vol. 16, no. 3, pp. 1262–1270, 2014.

[132] A. H. Clark, J. Imbao, R. Frahm, and M. Nachtegaal, "ProQEXAFS: A highly optimized parallelized rapid processing software for QEXAFS data," *Journal of Synchrotron Radiation*, vol. 27, pp. 551–557, 2020.

[133] B. Ravel and M. Newville, "ATHENA, ARTEMIS, HEPHAESTUS: data analysis for X-ray absorption spectroscopy using IFEFFIT.," eng, *Journal of synchrotron radiation*, vol. 12, no. Pt 4, pp. 537–541, Jul. 2005.

[134] J. Waser, H. A. Levy, and S. W. Peterson, "The structure of PdO," *Acta Crystallographica*, vol. 6, no. 7, pp. 661–663, 1953.

[135] M. Yashima and S. Kobayashi, "Positional disorder of oxygen ions in ceria at high temperatures," *Applied Physics Letters*, vol. 84, no. 4, pp. 526–528, 2004.

[136] H. Li, Q. Zhu, Y. Li, M. Gong, Y. Chen, J. Wang, and Y. Chen, "Effects of ceria/zirconia ratio on properties of mixed CeO2-ZrO2-Al2O3 compound," *Journal of Rare Earths*, vol. 28, no. 1, pp. 79–83, 2010.

[137] G. Li, Q. Wang, B. Zhao, M. Shen, and R. Zhou, "Effect of iron doping into CeO2-ZrO2 on the properties and catalytic behaviour of Pd-only three-way catalyst for automotive emission control," *Journal of Hazardous Materials*, vol. 186, no. 1, pp. 911–920, 2011.

[138] H. Liu, B. Zhao, Y. Chen, C. Ren, and Y. Chen, "Rare earths (Ce, Y, Pr) modified Pd/La2O3-ZrO2-]Al2O3 catalysts used in lean-burn natural gas fueled vehicles," *Journal of Rare Earths*, vol. 35, no. 11, pp. 1077–1082, 2017.

[139] W. Hu, G. Li, J. Chen, F. Huang, M. Gong, L. Zhong, and Y. Chen, "Enhancement of activity and hydrothermal stability of Pd/ZrO2-Al2O3 doped by Mg for methane combustion under lean conditions," *Fuel*, vol. 194, pp. 368–374, 2017.

[140] Q. Zheng, R. Farrauto, M. Deeba, and I. Valsamakis, "Part I: A comparative thermal aging study on the regenerability of Rh/Al2O3 and Rh/CexOy-ZrO2 as model catalysts for automotive three way catalysts," *Catalysts*, vol. 5, no. 4, pp. 1770–1796, 2015.

[141] G. Goula, G. Botzolaki, A. Osatiashtiani, C. M. Parlett, G. Kyriakou, R. M. Lambert, and I. V. Yentekakis, "Oxidative thermal sintering and redispersion of Rh nanoparticles on supports with high oxygen ion lability," *Catalysts*, vol. 9, no. 6, pp. 11–15, 2019.

[142] M. Haneda, Y. Tomida, T. Takahashi, Y. Azuma, and T. Fujimoto, "Three-way catalytic performance and change in the valence state of Rh in Y- and Pr-doped Rh/ZrO2 under lean/rich perturbation conditions," *Catalysis Communications*, vol. 90, pp. 1–4, 2017.

[143] S. Meiqing, M. Yang, J. Wang, J. Wen, M. Zhao, and W. Wang, "Pd/Support interface-promoted Pd-Ce0.7Zr0.3O 2-Al2O3 automobile three-way catalysts: Studying the dynamic oxygen storage capacity and CO, C3H8, and NO conversion," *Journal of Physical Chemistry C*, vol. 113, no. 8, pp. 3212–3221, 2009.

[144] S. Chen, Y. Yao, L. Lan, Y. Cao, C. Yan, M. Gong, and Y. Chen, "Effect of zirconium precursor on performance of Pd/Ce0.45Zr0.45La0.1O1.95 three-way catalyst," *Cuihua Xuebao/Chinese Journal of Catalysis*, vol. 33, no. 11, pp. 1762–1771, 2012.

[145] K. Khivantsev, C. G. Vargas, J. Tian, L. Kovarik, N. R. Jaegers, J. Szanyi, and Y. Wang, "Economizing on Precious Metals in Three-Way Catalysts: Thermally Stable and Highly Active Single-Atom Rhodium on Ceria for NO Abatement under Dry and Industrially Relevant Conditions**," *Angewandte Chemie*, vol. 133, no. 1, pp. 395–402, 2021.

[146] P. Da, J. Dutkiewicz, V. Choque, N. Homs, P. Kornelak, M. Najbar, A. Pietraszek, P. R. d. la Piscina, and J. Sobczak, "Alloying Effect in Low Loaded Rh Catalysts Supported on High Surface Area Alumina on Their Activity in CH4 and NO Decomposition," *Noble Metals*, no. February, 2012.

[147]   M. Manzoli, "Boosting the characterization of heterogeneous catalysts for H2O2 direct synthesis by infrared spectroscopy," *Catalysts*, vol. 9, no. 1, 2019.

[148]   J. B. Giorgi, T. Schroeder, M. Bäumer, and H. J. Freund, "Study of CO adsorption on crystalline-silica-supported palladium particles," *Surface Science*, vol. 498, no. 1-2, 2002.

[149]   F. Menegazzo, M. Signoretto, M. Manzoli, F. Boccuzzi, G. Cruciani, F. Pinna, and G. Strukul, "Influence of the preparation method on the morphological and composition properties of Pd-Au/ZrO2 catalysts and their effect on the direct synthesis of hydrogen peroxide from hydrogen and oxygen," *Journal of Catalysis*, vol. 268, no. 1, pp. 122–130, 2009.

[150]   J. G. McCarty, "Kinetics of PdO combustion catalysis," *Catalysis Today*, vol. 26, no. 3-4, pp. 283–293, 1995.

[151]   M. V. Twigg, "Rôles of catalytic oxidation in control of vehicle exhaust emissions," *Catalysis Today*, vol. 117, no. 4, pp. 407–418, 2006.

[152]   Y. Tomida and M. Haneda, "A study of ageing effect: Migration of rhodium under air atmosphere," *Catalysis Today*, vol. 376, no. August 2020, pp. 81–86, 2021.

[153]   F. Klingstedt, H. Karhu, A. Kalantar Neyestanaki, L. E. Lindfors, T. Salmi, and J. Väyrynen, "Barium promoted palladium catalysts for the emission control of natural gas driven vehicles and biofuel combustion systems," *Journal of Catalysis*, vol. 206, no. 2, pp. 248–262, 2002.

[154]   S. Tagliaferri, R. A. Köppel, and A. Baiker, "Influence of rhodium- and ceria-promotion of automotive palladium catalyst on its catalytic behaviour under steady-state and dynamic operation," *Applied Catalysis B: Environmental*, vol. 15, no. 3-4, pp. 159–177, 1998.

[155]   D. Wang, J. Gong, J. Luo, J. Li, K. Kamasamudram, N. Currier, and A. Yezerets, "Distinct reaction pathways of methane oxidation on different oxidation states over Pd-based three-way catalyst (TWC)," *Applied Catalysis A: General*, vol. 572, no. December 2018, pp. 44–50, 2019.

[156]   H. Xiong, M. H. Wiebenga, C. Carrillo, J. R. Gaudet, H. N. Pham, D. Kunwar, S. H. Oh, G. Qi, C. H. Kim, and A. K. Datye, "Design considerations for low-temperature hydrocarbon oxidation reactions on Pd based catalysts," *Applied Catalysis B: Environmental*, vol. 236, no. March, pp. 436–444, 2018.

[157]   D. Gao, C. Zhang, S. Wang, Z. Yuan, and S. Wang, "Catalytic activity of Pd/Al2O3 toward the combustion of methane," *Catalysis Communications*, vol. 9, no. 15, pp. 2583–2587, 2008.

[158]   S. Eriksson, S. Rojas, M. Boutonnet, and J. L. Fierro, "Effect of Ce-doping on Rh/ZrO2 catalysts for partial oxidation of methane," *Applied Catalysis A: General*, vol. 326, no. 1, pp. 8–16, 2007.

[159]   P. Velin, M. Ek, M. Skoglundh, A. Schaefer, A. Raj, D. Thompsett, G. Smedler, and P. A. Carlsson, "Water Inhibition in Methane Oxidation over Alumina Supported Palladium Catalysts," *Journal of Physical Chemistry C*, vol. 123, no. 42, pp. 25 724–25 737, 2019.

[160] M. Lyubovsky and L. Pfefferle, "Complete methane oxidation over Pd catalyst supported on -alumina. Influence of temperature and oxygen pressure on the catalyst activity," *Catalysis Today*, vol. 47, no. 1-4, pp. 29–44, 1999.

[161] A. A. Vedyagin, A. M. Volodin, V. O. Stoyanovskii, R. M. Kenzhin, E. M. Slavinskaya, I. V. Mishakov, P. E. Plyusnin, and Y. V. Shubin, "Stabilization of active sites in alloyed Pd-Rh catalysts onγ -Al2O3 support," *Catalysis Today*, vol. 238, pp. 80–86, 2014.

[162] EPFL, *EELS*, 2021. [Online]. Available: `https://www.epfl.ch/research/facilities/cime/electron-microscopy/introduction-to-em/page-26780-en-html/page-26788-en-html/[Accessesd:13.09.21]`.

[163] F. Klingstedt, A. K. Neyestanaki, L. E. Lindfors, M. Lundén, M. Petersson, P. Tengström, T. Ollonqvist, and J. Väyrynen, "Palladium based catalysts for exhaust aftertreatment of natural gas powered vehicles and biofuel combustion," *Applied Catalysis A: General*, vol. 209, no. 1-2, pp. 301–316, 2001.

[164] D. Bounechada, G. Groppi, P. Forzatti, K. Kallinen, and T. Kinnunen, "Enhanced methane conversion under periodic operation over a Pd/Rh based TWC in the exhausts from NGVs," *Topics in Catalysis*, vol. 56, no. 1-8, pp. 372–377, 2013.

[165] H. Muraki, K. Yokota, and Y. Fujitani, "Nitric Oxide Reduction Performance of Automotive Palladium Catalysts," vol. 48, pp. 93–105, 1989.

[166] C. F. Cullis, T. G. Nevell, and D. L. Trimm, "Role of the catalyst support in the oxidation of methane over palladium," *Journal of the Chemical Society, Faraday Transactions 1: Physical Chemistry in Condensed Phases*, vol. 68, pp. 1406–1412, 1972.

[167] M. Haneda, O. Houshito, H. Takagi, K. Shinoda, Y. Nakahara, K. Hiroe, T. Fujitani, and H. Hamada, "Catalytic performance of aged Rh/CeO2-ZrO2 for NO-C3H6-O2 reaction under a stoichiometric condition," *Topics in Catalysis*, vol. 52, no. 13-20, pp. 1868–1872, 2009.

[168] E. A. Alikin and A. A. Vedyagin, "High Temperature Interaction of Rhodium with Oxygen Storage Component in Three-Way Catalysts," *Topics in Catalysis*, vol. 59, no. 10-12, pp. 1033–1038, 2016.

[169] L. Kundakovic, D. R. Mullins, and S. H. Overbury, "Adsorption and reaction of H2O and CO on oxidized and reduced Rh/CeOx(111) surfaces," *Surface Science*, vol. 457, no. 1, pp. 51–62, 2000.

[170] National Institute of Standards and Technology, *Carbon monoxide*, 2021. [Online]. Available: `https://webbook.nist.gov/cgi/cbook.cgi?ID=C630080&Type=IR-SPEC&Index=1/[Accessed:12.05.2021]`.

[171] National Institute of Standards and Technology, *Nitrous oxide*, 2021. [Online]. Available: `https://webbook.nist.gov/cgi/cbook.cgi?ID=C10024972&Type=IR-SPEC&Index=1/[Accessed:12.05.2021]`.

[172] National Institute of Standards and Technology, *Ammonia*, 2021. [Online]. Available: `https://webbook.nist.gov/cgi/cbook.cgi?ID=C7664417&Type=IR-SPEC&Index=1/[Accessed:12.05.2021]`.

Appendix A

Calculations

A.1 Synthesis calculations

A.1.1 Dilution of Rh precursor

The precursor for the Rh-based catalyst was a aqueous solution of $Rh(NO_3)_3$ with a 32 % Rh assay that and was diluted to a 5 wt% Rh metal aqueous solution through these calculations:

$$\frac{m_{5wt\%Rh(aq)} \cdot 5}{100} = m_{Rh} \tag{A.1}$$

where $m_{5wt\%Rh(aq)}$ is the mass of the desired 5 wt% Rh metal aqueous solution and m_{Rh} is the mass pure Rh in the solution. Furthermore $m_{5wt\%Rh(aq)}$ can be written as:

$$m_{5wt\%Rh(aq)} = m_{H_2O} + m_{32\%Rhassay} \tag{A.2}$$

where m_{H_2O} is the amount of water need to dilute the 32 % Rh assay solution, $m_{32\%Rhassay}$, which can be written as:

$$m_{32\%Rhassay} = \frac{m_{Rh \cdot 100}}{32} \tag{A.3}$$

Combining Equation

Letting $m_{H_2O} = 10$ g, the mass of Rh in the 5 wt% Rh metal aqueous solution would be:

$$\frac{10 + \frac{m_{Rh \cdot 100}}{32} \cdot 5}{100} = m_{Rh} \tag{A.4}$$

$$m_{Rh} = \frac{10}{100/5 - 100/32} \tag{A.5}$$

$$= 0.59g \tag{A.6}$$

and the amount of $m_{32\%Rhassay}$ needed for a 5wt% Rh solution from Equation A.3 and would be:

$$m_{32\%Rhassay} = \frac{0.59 \cdot 100}{32} \tag{A.7}$$

$$= 1.84g \tag{A.8}$$

A.1.2   Amount of precursor

The amount of precursors were calculated based on the following equations, where the amount of $Pd(NO_3)_2 \cdot 6H_2O$ to synthesize 2wt% Pd/Al_2O_3, when the mass of Al_2O_3 was 3g, is used as an example calculation.

$$m_{cat} = \frac{m_{Al_2O_3} \cdot 100}{100 - wt\%Pd} \tag{A.9}$$

$$= \frac{3g \cdot 100}{100 - 2} \tag{A.10}$$

$$= 3.061g \tag{A.11}$$

where m_{cat} is the mass of total catalyst, $m_{Al_2O_3}$ is the mass of Al_2O_3 and $wt\%Pd$ is the desired weight percent of Pd. Further on the mass of Pd, m_{Pd} was calculated through Equation A.12:

$$m_{Pd} = mcat - mAl_2O_3 = 3.061g - 3g = 0.61g \tag{A.12}$$

$$m_{Pd(NO_3)_2 \cdot 6H_2O} = \frac{m_{Pd} \cdot 100}{4.5} \tag{A.13}$$

$$= \frac{0.61g \cdot 100}{4.5} \tag{A.14}$$

$$= 2.11g \tag{A.15}$$

Appendix B

Calibration of FTIR

The calibration of CO, N_2O and NH_3 was executed by flowing a known concentrations of the gas in Ar through an empty reactor which was plotted against the intensity of a chosen peak corresponding to the specific molecule in the IR-spectra. Figure B.1 shows the curve obtain under CO calibration and the linear regression curve with the corresponding equation used to estimate the CO concentrations. The intensity that is used is obtained at 2126 cm^{-1} in the IR-spectra which is specific for CO [170].

y = 455392x+94.762
R^2 = 0.9974
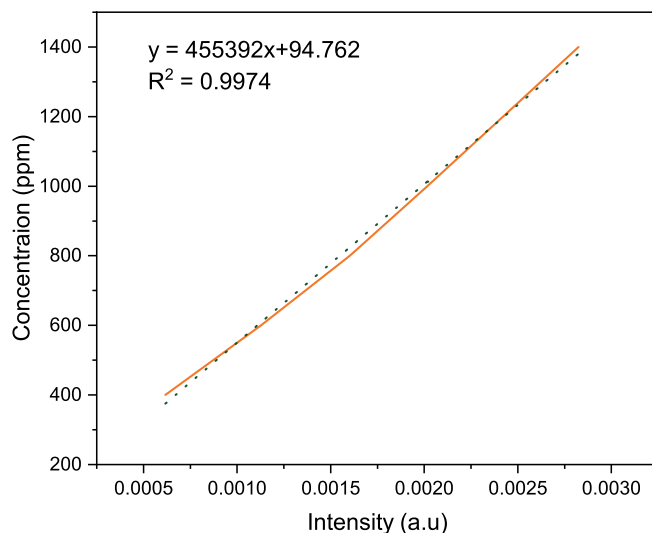
Figure B.1: The CO calibration curve obtained by plotting known concentrations of CO and against its intensity at 2126 cm^{-1} in the IR-spectra.

Figure B.2 shows the curve obtain underN$_2$O calibration and the linear regression curve with the corresponding equation used to estimate the N$_2$O concentrations. The intensity that is used is obtained at 2237 cm^{-1} in the IR-spectra which is specific for N$_2$O [171].
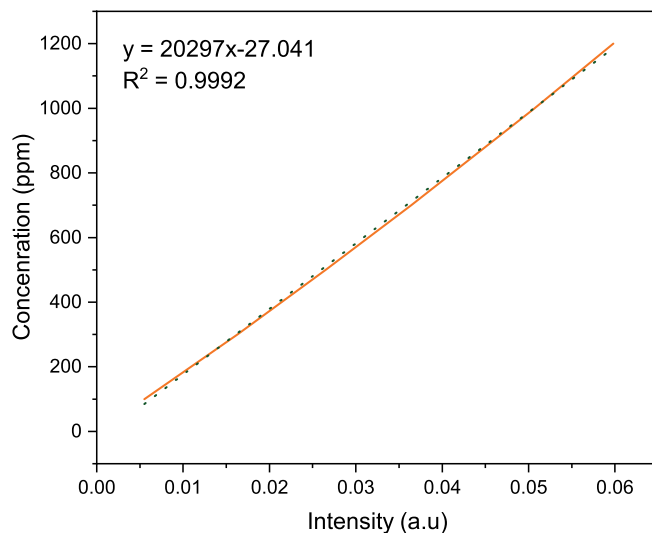
Figure B.2: The N$_2$O calibration curve obtained by plotting known concentrations of N$_2$O and against its intensity at 2237 cm^{-1} in the IR-spectra.

Figure B.1 shows the curve obtain under NH$_3$ calibration and the linear regression curve with the corresponding equation used to estimate the NH$_3$concentrations. The intensity that is used is obtained at 965 cm^{-1} in the IR-spectra which is specific for NH$_3$ [172].
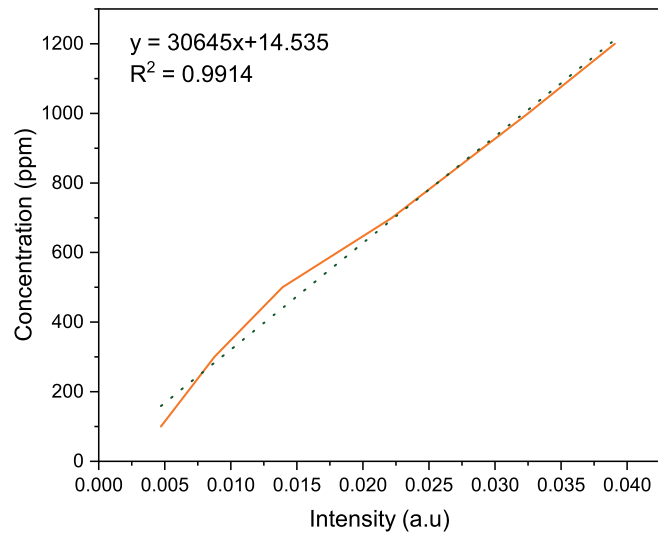
Figure B.3: The NH$_3$ calibration curve obtained by plotting known concentrations of NH$_3$ and against its intensity at 965 cm^{-1} in the IR-spectra.

Appendix C

Particle Size Distribution

The particle size distribution of all catalysts are shown in Figure C.1 which were obtain from counting TEM images.
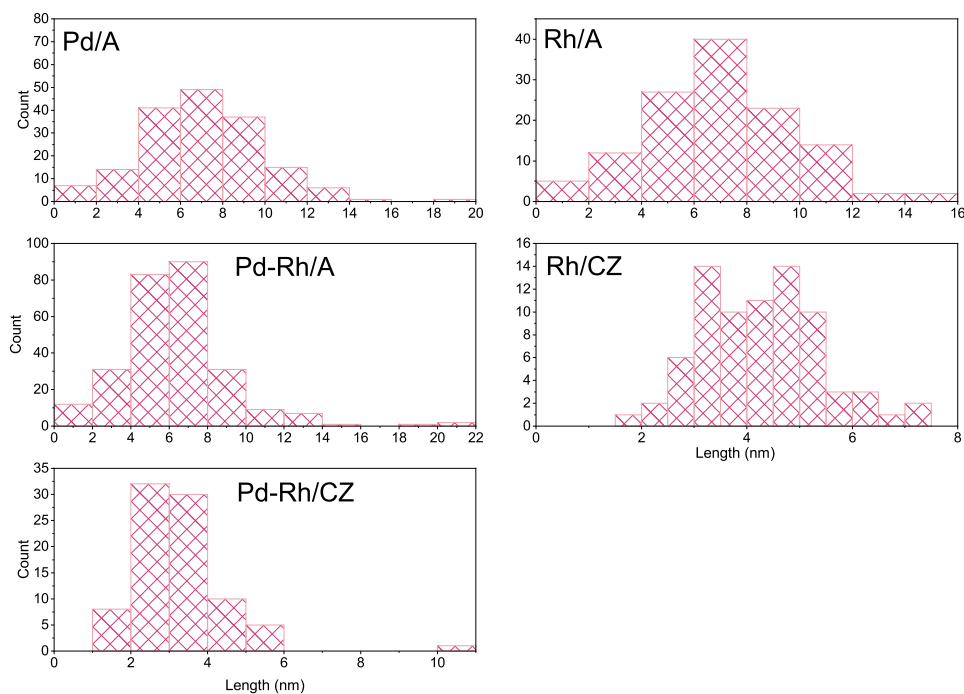
Figure C.1: Particle size distribution of all the samples obtained from TEM images.

Appendix D

Pore Size Distribution

The pore size distribution was obtained by the desorption branch of the isotherms from N_2-physisorption by applying the BJH method.Figure D.1 represents the pore size distribution for the alumina-based samples, and Figure D.2 for the CZ-based samples.
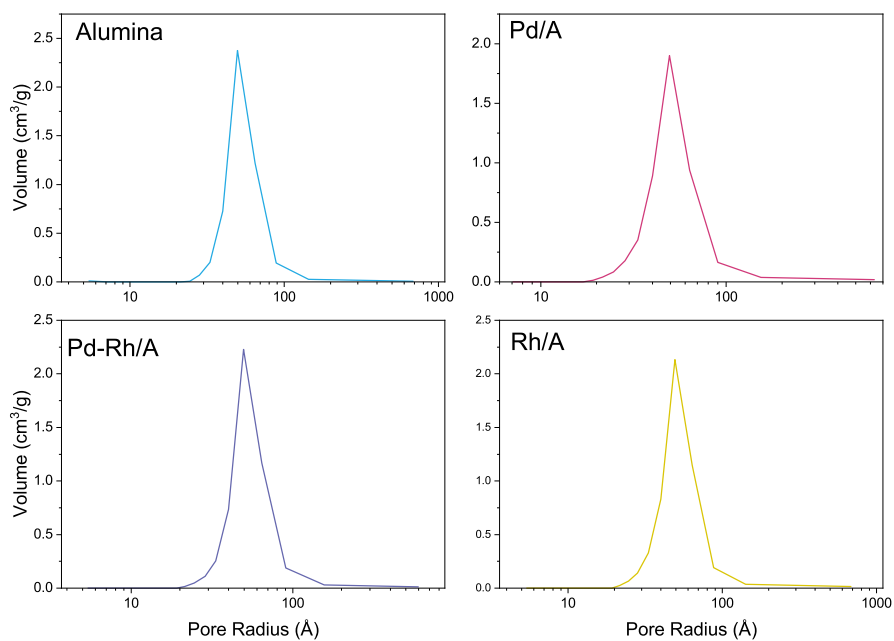
Figure D.1: Pore size distribution for the alumina-based samples obtained by applying the BJH method on the desorption branch of the isotherm from N_2-physisorption.
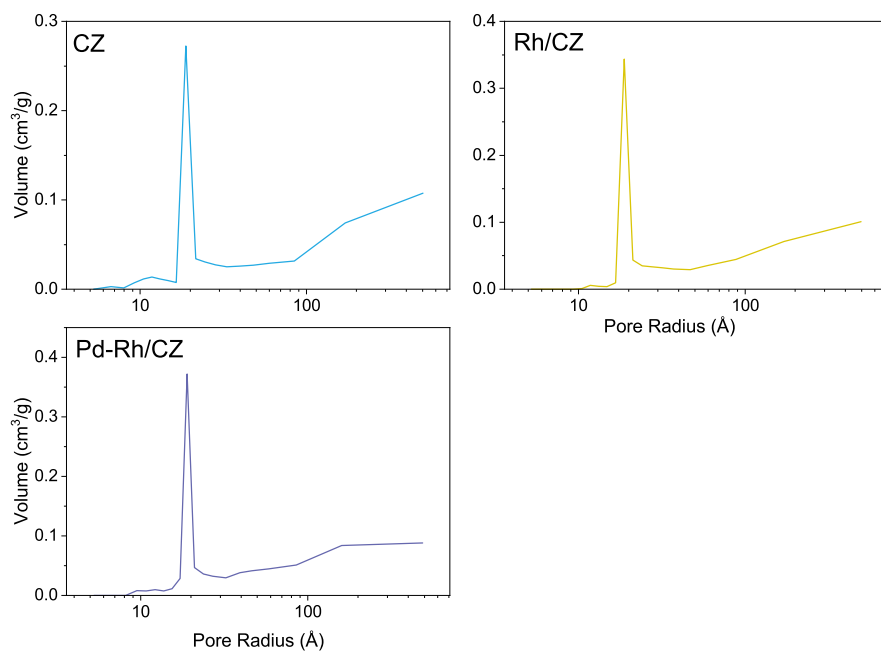
Figure D.2: Pore size distribution for the CZ-based samples obtained by applying the BJH method on the desorption branch of the isotherm from N$_2$-physisorption.

Appendix E

MS signal of H_2O, O_2 and CO_2

The figures below illustrates the MS signal of O_2, H_2O and CO_2 under stoichiometric temperature ramps. Figure E.1, E.2, E.3, E.4 and E.5 corresponds to Pd/A, Rh/A, Pd-Rh/A, Rh/CZ and Pd-Rh/CZ respectively.
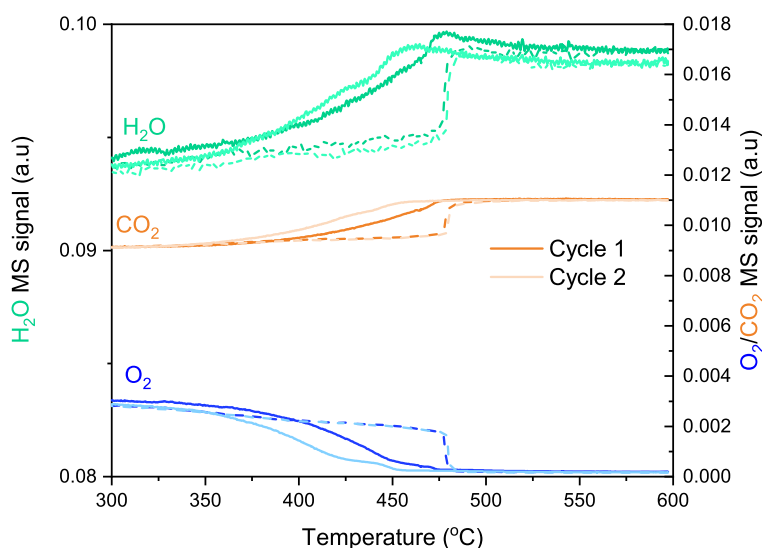
Figure E.1: O_2, H_2O and CO_2 MS signal after two temperature cycles of heating and cooling over **Pd/A** under stoichiometric conditions corresponding to 5 vol % H_2O, 0.15 vol% CH_4, 0.16 vol% NO, 0.7 vol% CO and 0.57 vol% O_2 in Ar at a WHSV of 240 L h^{-1} g_{cat}^{-1}. The darker color corresponds to the first cycle and the lighter color corresponds to the second cycle.
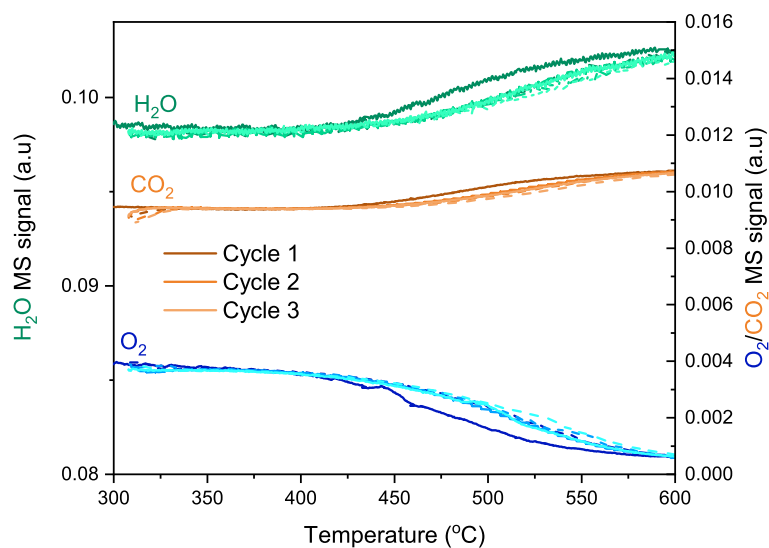
Figure E.2: O_2, H_2O and CO_2 MS signal after three temperature cycles of heating and cooling over **Rh/A** under stoichiometric conditions corresponding to 5 vol % H_2O, 0.15 vol% CH_4, 0.16 vol% NO, 0.7 vol% CO and 0.57 vol% O_2 in Ar at a WHSV of 240 L h^{-1} g$_{cat}^{-1}$. The darker color corresponds to the first cycle and the lighter colors corresponds to the second and third cycle.
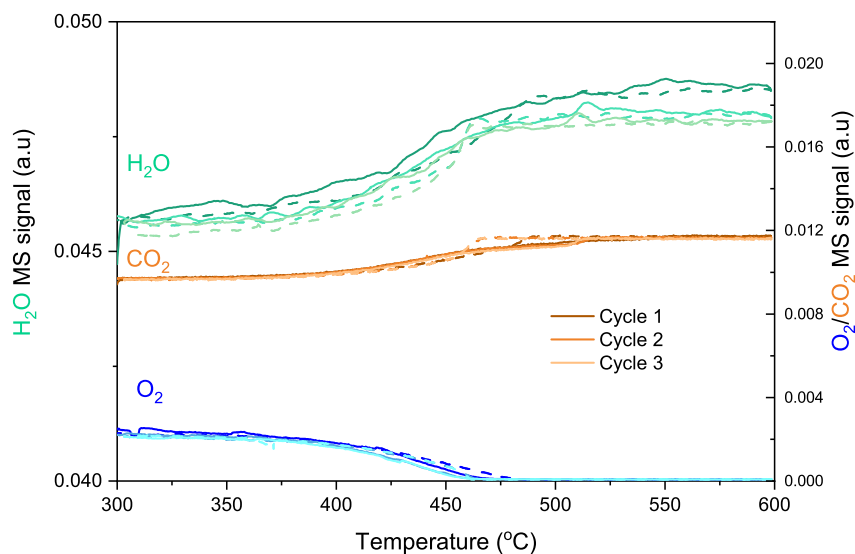
Figure E.3: O_2, H_2O and CO_2 MS signal after two temperature cycles of heating and cooling over **Pd-Rh/A** under stoichiometric conditions corresponding to 5 vol % H_2O, 0.15 vol% CH_4, 0.16 vol% NO, 0.7 vol% CO and 0.57 vol% O_2 in Ar at a WHSV of 240 L h^{-1} g$_{cat}^{-1}$. The darker color corresponds to the first cycle and the lighter colors corresponds to the second and third cycle.
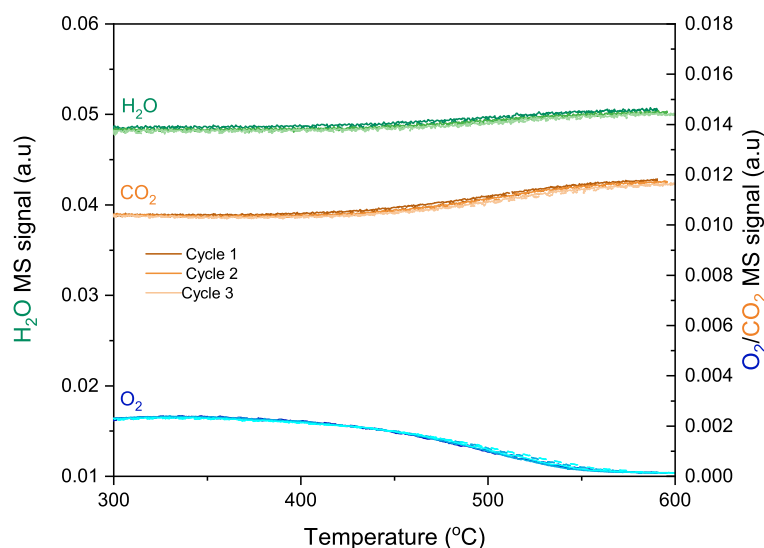
Figure E.4: O_2, H_2O and CO_2 MS signal after three temperature cycles of heating and cooling over **Rh/CZ** under stoichiometric conditions corresponding to 5 vol % H_2O, 0.15 vol% CH_4, 0.16 vol% NO, 0.7 vol% CO and 0.57 vol% O_2 in Ar at a WHSV of 240 L h^{-1} g_{cat}^{-1}. The darker color corresponds to the first cycle and the lighter colors corresponds to the second and third cycle.
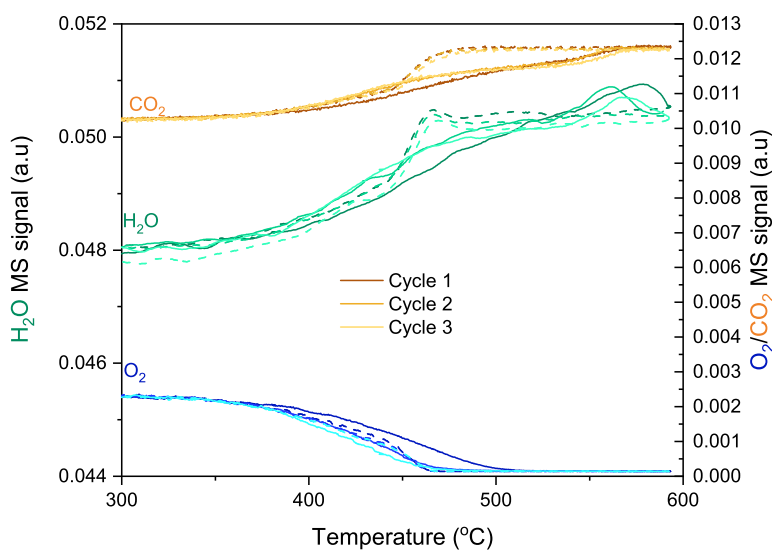
Figure E.5: O_2, H_2O and CO_2 MS signal after three temperature cycles of heating and cooling over **Pd-Rh/CZ** under stoichiometric conditions corresponding to 5 vol % H_2O, 0.15 vol% CH_4, 0.16 vol% NO, 0.7 vol% CO and 0.57 vol% O_2 in Ar at a WHSV of 240 L h^{-1} g_{cat}^{-1}. The darker color corresponds to the first cycle and the lighter colors corresponds to the second and third cycle.

Appendix F

Temperature Ramps at $\lambda = 1$

The figures below illustrates the stoichiometric temperature ramps that was conducted on all the samples after a reductive pretreatment. Figure F.1, F.2, F.3, F.4 and F.5 corresponds to Pd/A, Rh/A, Pd-Rh/A, Rh/CZ and Pd-Rh/CZ respectively.
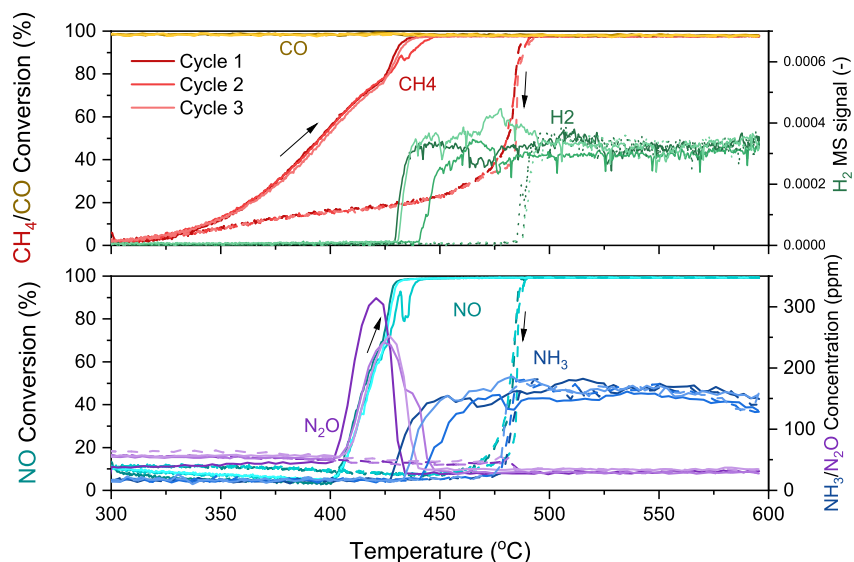
Figure F.1: CO, CH$_4$ and NO conversion, H$_2$ MS signal and NH$_3$ and N$_2$O concentration over during three temperature cycles of heating and cooling over **Pd/A** under stoichiometric conditions after a **reductive pretreatment** corresponding to 5 vol % H$_2$O, 0.15 vol% CH$_4$, 0.16 vol% NO, 0.7 vol% CO and 0.57 vol% O$_2$ in Ar at a WHSV of 240 L h^{-1} g$_{\text{cat}}^{-1}$. The darker colors corresponds to the first cycle and the lighter colors corresponds to the second and third cycle.
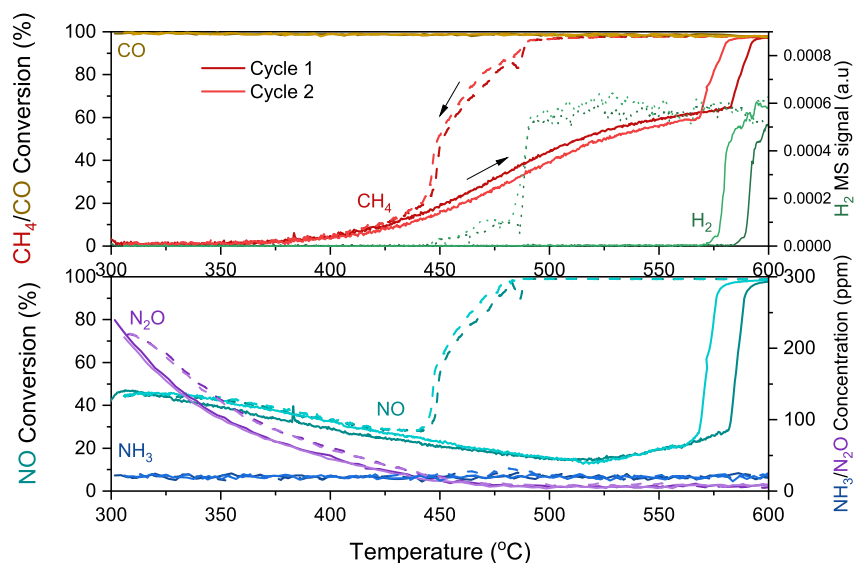
Figure F.2: CO, CH$_4$ and NO conversion, H$_2$ MS signal and NH$_3$ and N$_2$O concentration over during two temperature cycles of heating and cooling over **Rh/A** under stoichiometric conditions after a **reductive pretreatment** corresponding to 5 vol % H$_2$O, 0.15 vol% CH$_4$, 0.16 vol% NO, 0.7 vol% CO and 0.57 vol% O$_2$ in Ar at a WHSV of 240 L h^{-1} g$_{cat}^{-1}$. The darker colors corresponds to the first cycle and the lighter colors corresponds to the second cycle.
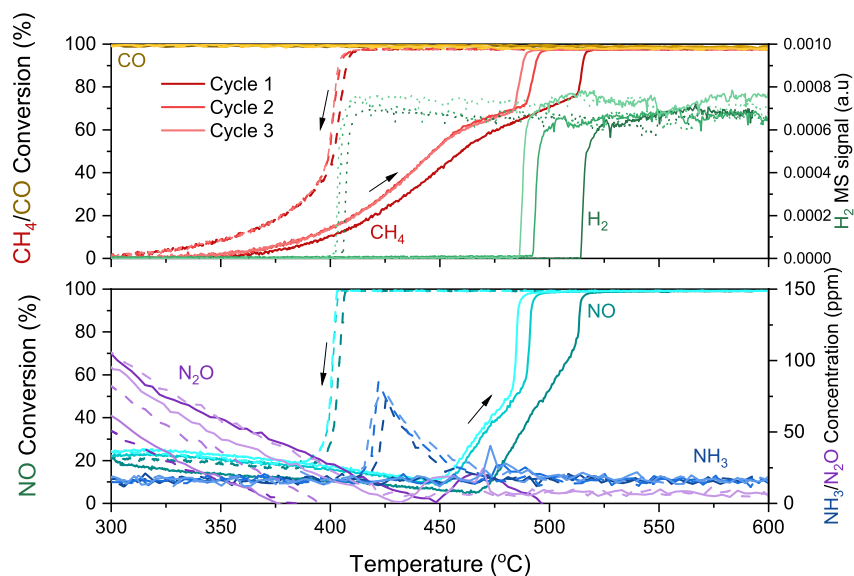
Figure F.3: CO, CH$_4$ and NO conversion, H$_2$ MS signal and NH$_3$ and N$_2$O concentration over during three temperature cycles of heating and cooling over **Pd-Rh/A** under stoichiometric conditions after a **reductive pretreatment** corresponding to 5 vol % H$_2$O, 0.15 vol% CH$_4$, 0.16 vol% NO, 0.7 vol% CO and 0.57 vol% O$_2$ in Ar at a WHSV of 240 L h^{-1} g$_{cat}^{-1}$. The darker colors corresponds to the first cycle and the lighter colors corresponds to the second and third cycle.
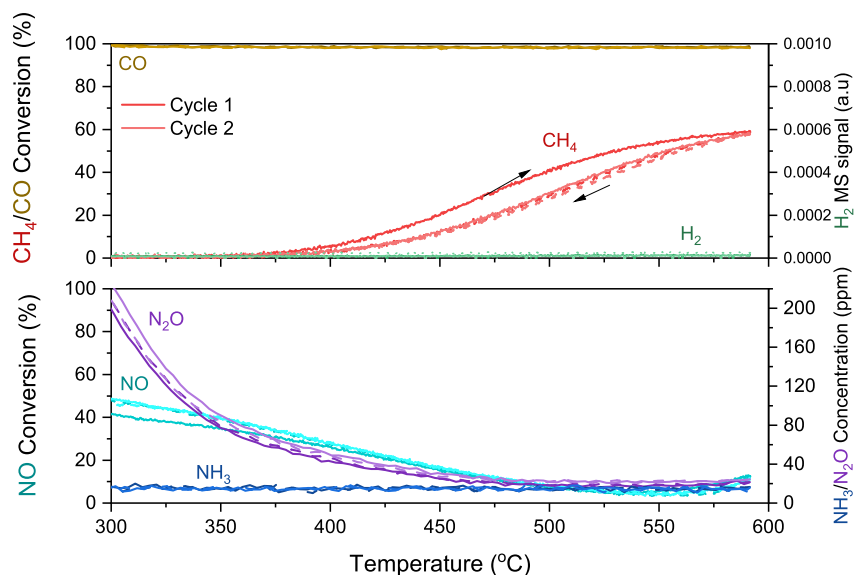
Figure F.4: CO, CH$_4$ and NO conversion, H$_2$ MS signal and NH$_3$ and N$_2$O concentration over during two temperature cycles of heating and cooling over **Rh/CZ** under stoichiometric conditions after a **reductive pretreatment** corresponding to 5 vol % H$_2$O, 0.15 vol% CH$_4$, 0.16 vol% NO, 0.7 vol% CO and 0.57 vol% O$_2$ in Ar at a WHSV of 240 L h^{-1} g$_{cat}^{-1}$. The darker colors corresponds to the first cycle and the lighter colors corresponds to the second cycle.
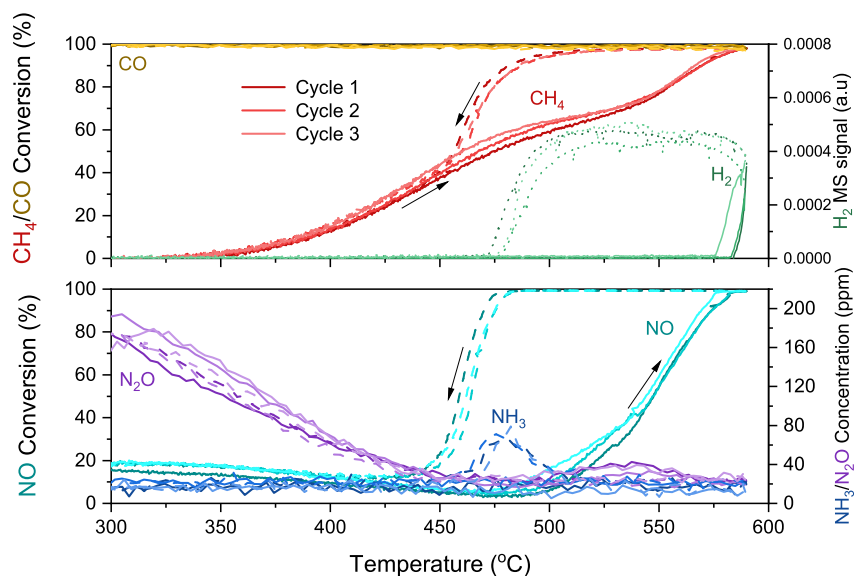
Figure F.5: CO, CH$_4$ and NO conversion, H$_2$ MS signal and NH$_3$ and N$_2$O concentration over during threee temperature cycles of heating and cooling over **Pd-Rh/CZ** under stoichiometric conditions after a **reductive pretreatment** corresponding to 5 vol % H$_2$O, 0.15 vol% CH$_4$, 0.16 vol% NO, 0.7 vol% CO and 0.57 vol% O$_2$ in Ar at a WHSV of 240 L h^{-1} g$_{cat}^{-1}$. The darker colors corresponds to the first cycle and the lighter colors corresponds to the second and third cycle.

Figure F.6 represents the stoichiometric temperature ramps over a 11 wt%Pd/CZ sample.
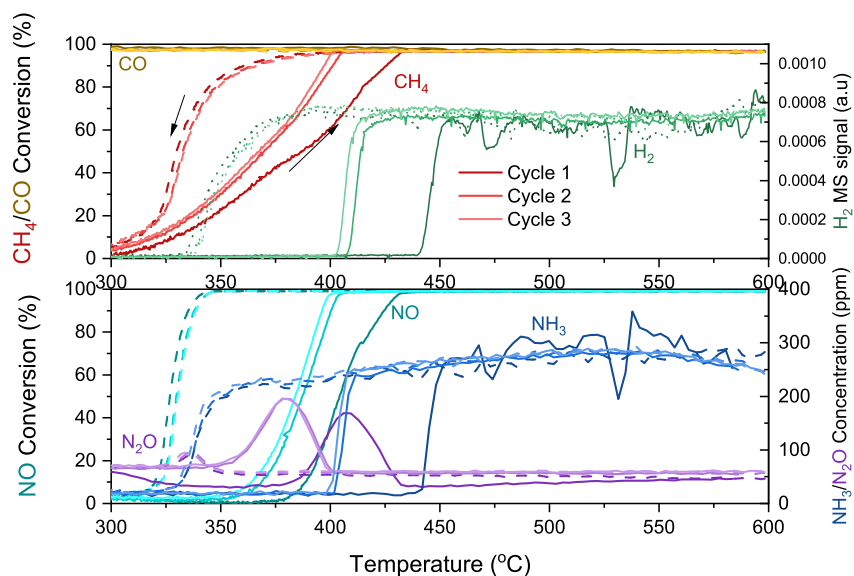
Figure F.6: CO, CH$_4$ and NO conversion, H$_2$ MS signal and NH$_3$ and N$_2$O concentration over during two temperature cycles of heating and cooling over **Pd/CZ** under stoichiometric conditions corresponding to 5 vol % H$_2$O, 0.15 vol% CH$_4$, 0.16 vol% NO, 0.7 vol% CO and 0.57 vol% O$_2$ in Ar at a WHSV of 240 L h^{-1} g$_{cat}^{-1}$. The darker colors corresponds to the first cycle and the lighter colors corresponds to the second and third cycle.

F.1   Frozen Temperature Ramps for XAS Measurements

Figure F.7 and F.8 represents the temperature ramps that was frozen at approximately 425 C for ex situ XAS measurements on prereduced and preoxidized Pd-Rh/A respectively.
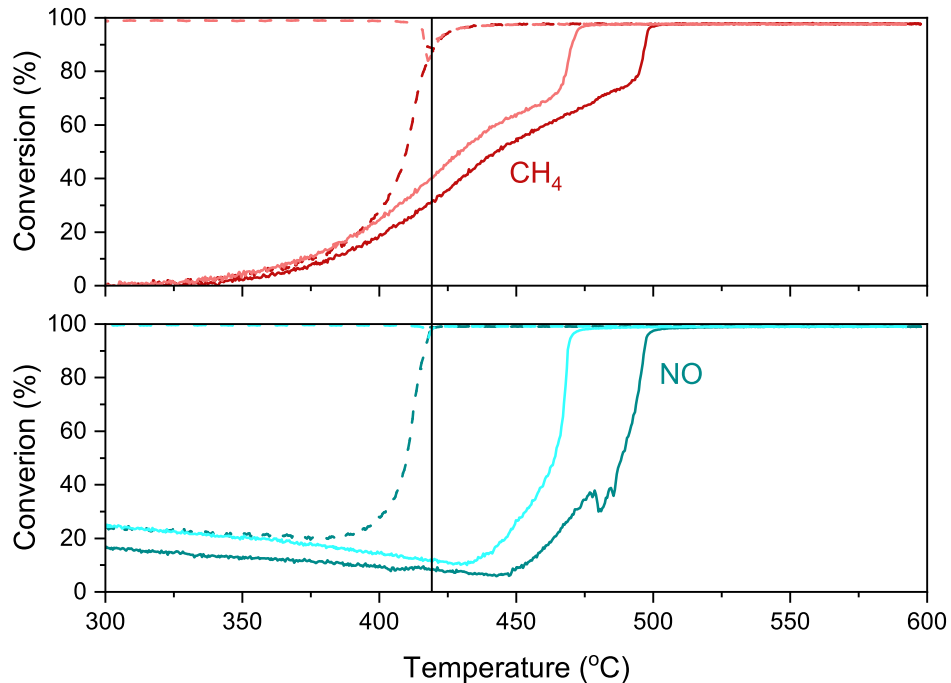
Figure F.7: Prereduced Pd-Rh/A which was frozen at 425 °C for XAS measurements.
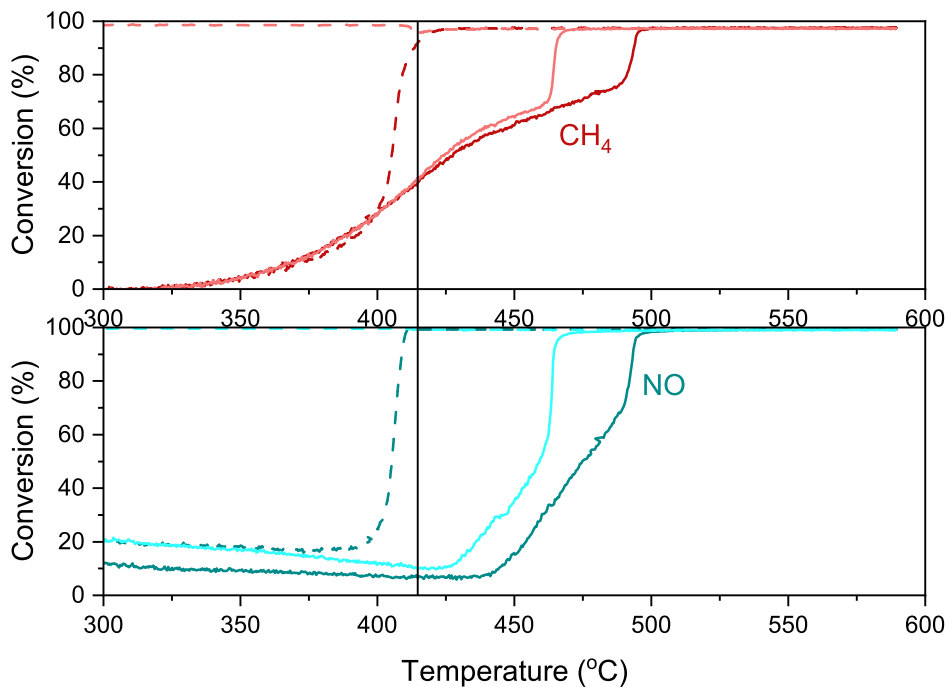
Figure F.8: Preoxidized Pd-Rh/A which was frozen at 425 °C for XAS measurements.

Appendix G

O₂ Dithering Optimization

G.1   Pulsing optimization

Figure G.1 represents part of the O₂ dithering optimization over Pd-Rh/A with an amplitude of 0.25 at different frequencies.
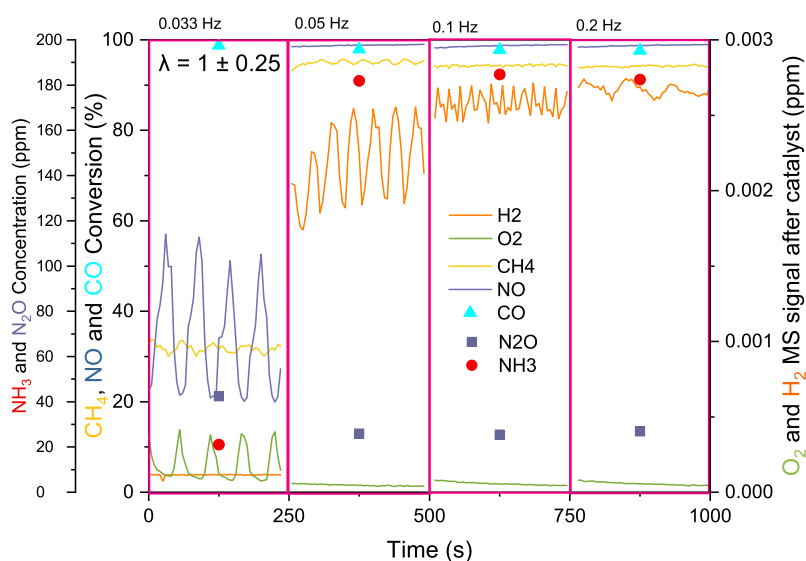
Figure G.1: O₂ dithering optimization over Pd-Rh/A with an amplitude of 0.25 at different frequencies.

G.2   Insert on pulses during temperature Ramps

Figure G.2 and G.3 are inserts from the first cycle in the heating ramps under the optimized O₂ dithering for Pd/A and Rh/A respectively.
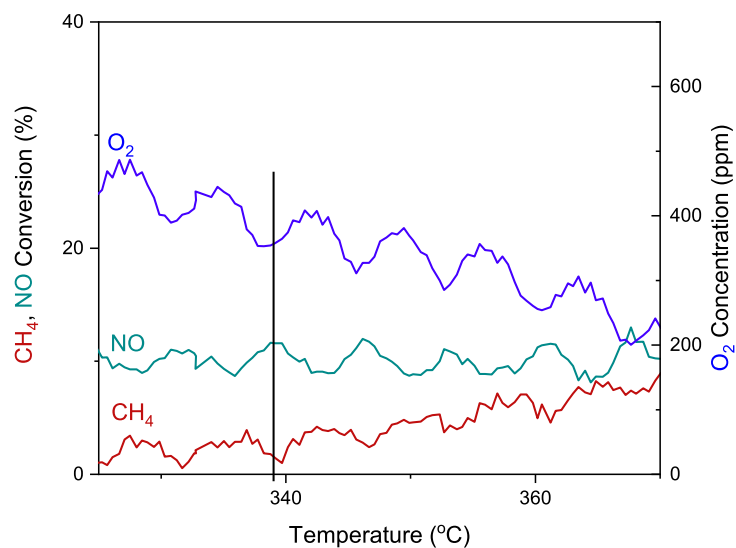
Figure G.2: An insert of temperature ramps under optimized O_2 dithering conditions over **Pd/A**. The black line shows that a rich pulse corresponds to higher NO conversion.
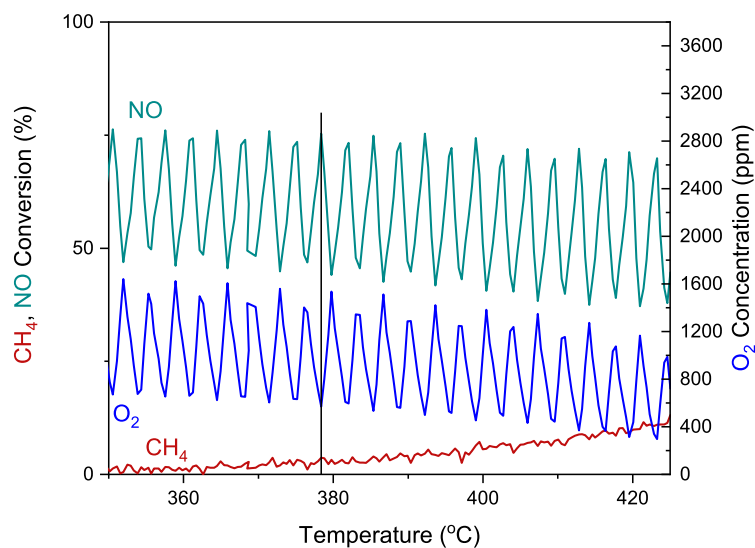
Figure G.3: An insert of temperature ramps under optimized O_2 dithering conditions over **Rh/A**. The black line shows that a rich pulse corresponds to higher NO conversion.

Appendix H

Risk Assessment

A risk and safety assessment was conducted for the experiments through NTNU Risk Assessment protocol and can be reviewed below.

ID	42332		**Status**	**Date**
Risk Area	Risikovurdering: Helse, miljø og sikkerhet (HMS)		Created	28.05.2021
Created by	Vilde Vinnes Jacobsen		Assessment started	28.05.2021
Responsible	Vilde Vinnes Jacobsen		Measures decided	
			Closed	

Risk Assessment:

CAT masterstudent_ 2021 Vilde Vinnes Jacobsen

Valid from-to date:

4/12/2021 - 5/28/2024

Location:

OLGA, 4th floor, Paul Scherrer Institute, Switzerland

Goal / purpose

Promote steam reforming of methane in the TWC in a natural gas exhaust system by developing and testing different catalysts.

Background

Synthesis of Pd/Al2O3, Rh/Al2O3, Pd-Rh/Al2O3, CeZrO2, Pd/CeZrO2, Rh/CeZrO2 and Pd-Rh/CeZrO2
Chemicals:
- Palladium (II) nitrate solution (precursor)
- Rhodium(III) nitrate dihydrate (precursor)
- Cerium (III) nitrate hexahydrate (precursor)
- Zirconium (IV) oxynitrate hydrate
-Citric Acid monohydrate
- Ammonium hydroxide (25 vol%)
·Alumina Sasol Puralox SCFa-140

Instruments:
- Oven
- Calcination furnace

Method:
Synthesis of Pd/Al2O3, Rh/Al2O3, Pd/CeZrO2 and Rh/CeZrO2:
Pd(NO3)2 or a aqueous solution of Rh(NO3)3·2H2O is dropwise added to the support (Al2O3 or CeZrO2). The solution is dried
overnight at 120 oC before calcination (RT-550 oC) of the solid for 3h (5 oC/min).

Synthesis of Pd-Rh/Al2O3 and Pd-Rh/CeZrO2:
Pd(NO3)2 and a aqueous solution of Rh(NO3)3 is mixed and stirred for 2 h before being dropwise added to the support (Al2O3 or
CeZrO2). The solution is dried overnight at 120 oC before calcination (RT-550 oC) of the solid for 3h (5 oC/min).

Synthesis of CeZrO2:
Ce(NO3)3·6H2O and ZrO(NO3)2·xH2O is dissolved in distilled water under stirring. Citric acid monohydrate is added to the solution
before ammonium hydroxide is added dropwise until pH ~3. The solution is stirred for 3 h before being filtered and washed with
distilled water until the pH value is constant. The precipitate is dried at 110 oC for 2 h.

Activity Testing
Chemicals:
-Methane/Ar
-Oxygen
-NO/Ar
-CO/Ar
-Hydrogen
-Argon

Instrument
-Quartz glass reactor.
-Oven (Temperature <600ºC)
- Mass spectrometer
- IR spectrometer

Characterization
-N2 adsorption-desorption
-XRD
-OSC
-TPR
-TEM
-XAS
-CO-DRIFT
-ICP-OES

Description and limitations

always follow HSE rules
always read msds
recieve Proper training
follow all Safety measures
Be aware of physical risks such as pressure and temperature

Prerequesites, assumptions and simplifications

The work assumes that proper training is given prior to the use of laboratories and equipment/instruments to minimize the probability
of user-caused mistakes, and protect the user

Attachments

Ammonium Hydroxide 25% SDS.pdf
Hydrogen SDS.pdf
Liquid nitrogen SDS.pdf
Alumina SDS.pdf
NO SDS.pdf
Oxygen SDS.pdf
Palladium nitrate solution SDS.pdf
Argon SDS.pdf
Citric Acid SDS.pdf
Cerium nitrate hexahydrate SDS.pdf
CO SDS.pdf
Methane SDS.pdf
Rhodium nitrate dihydrate SDS.pdf
Set up OLGA 417.pdf
Zirconium oxynitrate SDS.pdf
2-propanol.pdf

References

[Ingen registreringer]

Summary, result and final evaluation

The summary presents an overview of hazards and incidents, in addtition to risk result for each consequence area.

Hazard:	**Handling chemicals: Pd(NO3)2, Rh(NO3)3*2H2O, Ce(NO3)3*6H2O, ZrO(NO3)2*xH2O, Al2O3, citric acid, ammonium hydroxide**

Incident:	**Spilling palladium (II) nitrate solution**

Consequence area:	Helse	Risk before measures:	🟡 Risiko after measures:	⚪
	Materielle verdier	Risk before measures:	🟡 Risiko after measures:	⚪

Incident:	**Spilling rhodium(III) nitrate dihydrate**

Consequence area:	Helse	Risk before measures:	🟡 Risiko after measures:	⚪
	Ytre miljø	Risk before measures:	🟡 Risiko after measures:	⚪

Incident:	**Spilling cerium (III) nitrate hexahydrate**

Consequence area:	Helse	Risk before measures:	🟡 Risiko after measures:	⚪
	Ytre miljø	Risk before measures:	🟡 Risiko after measures:	⚪

Incident:	**Spilling zirconium (IV) oxynitrate hydrate**

Consequence area:	Helse	Risk before measures:	🟡 Risiko after measures:	⚪
	Ytre miljø	Risk before measures:	🟡 Risiko after measures:	⚪

Incident:	**Spilling citric acid**

Consequence area:	Helse	Risk before measures:	🟢 Risiko after measures:	⚪

Incident:	**Spilling ammonium hydroxide**

Consequence area:	Helse	Risk before measures:	🟡 Risiko after measures:	⚪
	Ytre miljø	Risk before measures:	🟡 Risiko after measures:	⚪

Hazard:	Handling chemicals: Pd(NO3)2, Rh(NO3)3*2H2O, Ce(NO3)3*6H2O, ZrO(NO3)2*xH2O, Al2O3, citric acid, ammonium hydroxide

Incident:	Spilling 2-propanol

Consequence area:	Helse	Risk before measures:	🟢	Risiko after measures:	⚪
	Ytre miljø	Risk before measures:	🟡	Risiko after measures:	⚪
	Materielle verdier	Risk before measures:	🟡	Risiko after measures:	⚪

Hazard:	Calcination in high temperature furnace

Incident:	Burning injuries

Consequence area:	Helse	Risk before measures:	🟢	Risiko after measures:	⚪

Hazard:	Use of flammable and/or toxic gases: H2, O2, NO, CO

Incident:	Leakage of O2

Consequence area:	Helse	Risk before measures:	🟡	Risiko after measures:	⚪
	Ytre miljø	Risk before measures:	🟡	Risiko after measures:	⚪
	Materielle verdier	Risk before measures:	🟡	Risiko after measures:	⚪

Incident:	Leakage of H2

Consequence area:	Helse	Risk before measures:	🟡	Risiko after measures:	⚪
	Ytre miljø	Risk before measures:	🟡	Risiko after measures:	⚪
	Materielle verdier	Risk before measures:	🟡	Risiko after measures:	⚪

Incident:	Leakage of NO

Consequence area:	Helse	Risk before measures:	🟡	Risiko after measures:	⚪
	Ytre miljø	Risk before measures:	🟡	Risiko after measures:	⚪
	Materielle verdier	Risk before measures:	🟡	Risiko after measures:	⚪

Hazard:	**Use of flammable and/or toxic gases: H2, O2, NO, CO**				
Incident:	**Leakage of CO**				
Consequence area:	Helse	Risk before measures:	🟡	Risiko after measures:	⚪
	Ytre miljø	Risk before measures:	🟡	Risiko after measures:	⚪
	Materielle verdier	Risk before measures:	🟡	Risiko after measures:	⚪

Hazard:	**Use of nontoxic gases and/or inert gases: CH4, Ar**				
Incident:	**Leakage of CH4**				
Consequence area:	Helse	Risk before measures:	🟡	Risiko after measures:	⚪
	Ytre miljø	Risk before measures:	🟡	Risiko after measures:	⚪
	Materielle verdier	Risk before measures:	🟡	Risiko after measures:	⚪
Incident:	**Leakage of Argon**				
Consequence area:	Helse	Risk before measures:	🟡	Risiko after measures:	⚪
	Ytre miljø	Risk before measures:	🟡	Risiko after measures:	⚪
	Materielle verdier	Risk before measures:	🟡	Risiko after measures:	⚪

Hazard:	**Heating the reactor furnace**				
Incident:	**Burning injuries**				
Consequence area:	Helse	Risk before measures:	🟢	Risiko after measures:	⚪

Hazard:	**Electricity failure**				
Incident:	**Fire**				
Consequence area:	Helse	Risk before measures:	🟡	Risiko after measures:	⚪
	Ytre miljø	Risk before measures:	🟡	Risiko after measures:	⚪
	Materielle verdier	Risk before measures:	🟡	Risiko after measures:	⚪

Hazard:	**N2-physisorption, TPR**
Incident:	**Handling liquid nitrogen**

Consequence area: Helse   Risk before measures: ⬤   Risiko after measures: ⬤

Final evaluation

Organizational units and people involved

A risk assessment may apply to one or more organizational units, and involve several people. These are lsited below.

Organizational units which this risk assessment applies to

- Prorektor for utdanning
- Avdeling for utdanningskvalitet
- Seksjon for etter- og videreutdanning
- Avdeling for studieadministrasjon
- Avdeling for studieadministrasjon - Ålesund
- Avdeling for studieadministrasjon - Gjøvik
- Avdeling for studenttjenester
- Universitetsbiblioteket
- Biblioteksjef stab
- Bibliotekseksjon for samlinger og digitale tjenester
- Bibliotekseksjon for kultur- og vitenskapshistorie
- Bibliotekseksjon for medisin og helsevitenskap
- Bibliotekseksjon for arkitektur, naturvitenskap, teknologi og økonomi
- Bibliotekseksjon for humaniora, samfunns- og utdanningsvitenskap
- Bibliotekseksjon i Ålesund
- Bibliotekseksjon i Gjøvik
- Prorektor for forskning
- Prorektor for nyskaping
- Viserektor Gjøvik
- Bygningsdrift Gjøvik
- Viserektor Ålesund
- Bygningsdrift Ålesund
- Direktør for økonomi og eiendom
- Avdeling for virksomhetsstyring
- Økonomiavdelingen
- Seksjon for økonomirådgivning
- Seksjon for økonomitjenester
- Servicesenter for økonomi
- Avdeling for campusservice
- Seksjon for bygningsdrift
- Seksjon for teknisk drift
- Servicesenter for eiendom
- Stab Campusservice
- Eiendomsavdelingen
- Seksjon for prosjektgjennomføring
- Direktør for organisasjon
- HR og HMS avdelingen
- Kommunikasjonsavdelingen
- Avdeling for dokumentasjonsforvaltning

Norges teknisk-naturvitenskapelige universitet (NTNU)

Unntatt offentlighet jf. Offentlighetsloven § 14

Print date:
27.09.2021

Printed by:
Vilde Vinnes Jacobsen

Page:
8/34

- IT-avdelingen
- Rektors stab
- Fakultet for arkitektur og design (AD)
- Kunstakademiet i Trondheim
- Institutt for design
- Institutt for arkitektur og teknologi
- Institutt for arkitektur og planlegging
- AD Fakultetsadministrasjonen
- Det humanistiske fakultet (HF)
- Institutt for filosofi og religionsvitenskap
- Institutt for historiske og klassiske studier
- Institutt for kunst- og medievitenskap
- Institutt for musikk
- Institutt for språk og litteratur
- Institutt for tverrfaglige kulturstudier
- HF Fakultetsadministrasjonen
- Institutt for moderne samfunnshistorie
- Fakultet for informasjonsteknologi og elektronikk (IE)
- Institutt for allmennfag
- Institutt for datateknologi og informatikk
- Institutt for elektroniske systemer
- Institutt for elkraftteknikk
- Institutt for IKT og realfag
- Institutt for informasjonssikkerhet og kommunikasjonsteknologi
- Institutt for matematiske fag
- Institutt for teknisk kybernetikk
- IE Fakultetsadministrasjonen
- Institutt for energi- og prosessteknikk
- Institutt for marin teknikk
- Institutt for geovitenskap og petroleum
- Institutt for bygg- og miljøteknikk
- Institutt for maskinteknikk og produksjon
- Institutt for havromsoperasjoner og byggteknikk
- Institutt for vareproduksjon og byggteknikk
- IV Fakultetsadministrasjonen
- Fakultet for medisin og helsevitenskap (MH)
- Institutt for helsevitenskap i Gjøvik
- Institutt for helsevitenskap i Ålesund
- Kavliinstitutt for nevrovitenskap
- Institutt for klinisk og molekylærmedisin
- Institutt for laboratoriemedisin, barne- og kvinnesykdommer
- Institutt for nevromedisin og bevegelsesvitenskap
- Institutt for psykisk helse
- Institutt for samfunnsmedisin og sykepleie
- Institutt for sirkulasjon og bildediagnostikk
- Avdeling for komparativ medisin
- MH Fakultetsadministrasjonen

- Fakultet for naturvitenskap (NV)
- Institutt for biologi
- Institutt for biologiske fag Ålesund
- Institutt for bioteknologi og matvitenskap
- Institutt for bioingeniørfag
- Institutt for fysikk
- Institutt for kjemi
- Institutt for kjemisk prosessteknologi
- Institutt for materialteknologi
- NV Fakultetsadministrasjonen og verksteder
- Nanolab
- Gunnerus
- Fakultet for økonomi (ØK)
- NTNU Handelshøyskolen
- Institutt for internasjonal forretningsdrift
- Institutt for industriell økonomi og teknologiledelse
- Institutt for samfunnsøkonomi
- ØK Fakultetsadministrasjonen
- Fakultet for samfunns- og utdanningsvitenskap (SU)
- Institutt for geografi
- Institutt for lærerutdanning
- Institutt for pedagogikk og livslang læring
- Institutt for sosialt arbeid
- Institutt for sosiologi og statsvitenskap
- Institutt for psykologi
- Institutt for sosialantropologi
- SU Fakultetsadministrasjonen
- NTNU Vitenskapsmuseet (VM)
- Institutt for naturhistorie
- Institutt for arkeologi og kulturhistorie
- Vitenskapsmuseet administrasjon
- BIBSYS

Participants

Readers

[Ingen registreringer]

Others involved/stakeholders

[Ingen registreringer]

The following accept criteria have been decided for the risk area Risikovurdering: Helse, miljø og sikkerhet (HMS):

Helse	Materielle verdier	Omdømme	Ytre miljø

Norges teknisk-naturvitenskapelige universitet (NTNU)

Unntatt offentlighet jf. Offentlighetsloven § 14

Print date:

27.09.2021

Printed by:

Vilde Vinnes Jacobsen

Page:

11/34

Overview of existing relevant measures which have been taken into account

The table below presents existing measures which have been take into account when assessing the likelihood and consequence of relevant incidents.

Hazard	Incident	Measures taken into account
Handling chemicals: Pd(NO3)2, Rh (NO3)3*2H2O, Ce(NO3)3*6H2O, ZrO (NO3)2*xH2O, Al2O3, citric acid, ammonium hydroxide	Spilling palladium (II) nitrate solution	Instrument and method training
	Spilling palladium (II) nitrate solution	Security Data Sheet
	Spilling palladium (II) nitrate solution	Gas Detector
	Spilling palladium (II) nitrate solution	Exhaust hood
	Spilling palladium (II) nitrate solution	Safety Equipment
	Spilling palladium (II) nitrate solution	Safety Equipment
	Spilling palladium (II) nitrate solution	Safe waste handeling
	Spilling palladium (II) nitrate solution	Safe waste handeling
	Spilling rhodium(III) nitrate dihydrate	Instrument and method training
	Spilling rhodium(III) nitrate dihydrate	Security Data Sheet
	Spilling rhodium(III) nitrate dihydrate	Exhaust hood
	Spilling rhodium(III) nitrate dihydrate	Safety Equipment
	Spilling rhodium(III) nitrate dihydrate	Safe waste handeling
	Spilling cerium (III) nitrate hexahydrate	Instrument and method training
	Spilling cerium (III) nitrate hexahydrate	Security Data Sheet
	Spilling cerium (III) nitrate hexahydrate	Safety Equipment
	Spilling cerium (III) nitrate hexahydrate	Safe waste handeling
	Spilling zirconium (IV) oxynitrate hydrate	Instrument and method training
	Spilling zirconium (IV) oxynitrate hydrate	Security Data Sheet
	Spilling zirconium (IV) oxynitrate hydrate	Safety Equipment
	Spilling zirconium (IV) oxynitrate hydrate	Safe waste handeling
	Spilling citric acid	Instrument and method training
	Spilling citric acid	Security Data Sheet
	Spilling citric acid	Safe waste handeling
	Spilling ammonium hydroxide	Instrument and method training
	Spilling ammonium hydroxide	Security Data Sheet
	Spilling ammonium hydroxide	Safety Equipment
	Spilling ammonium hydroxide	Safe waste handeling
	Spilling 2-propanol	Instrument and method training
	Spilling 2-propanol	Security Data Sheet
	Spilling 2-propanol	Safety Equipment
	Spilling 2-propanol	Safe waste handeling

Handling chemicals: Pd(NO3)2, Rh (NO3)3*2H2O, Ce(NO3)3*6H2O, ZrO (NO3)2*xH2O, Al2O3, citric acid, ammonium hydroxide	Spilling 2-propanol	Thermal protective wear
Calcination in high temperature furnace	Burning injuries	Instrument and method training
	Burning injuries	The set up
	Burning injuries	Thermal protective wear
Use of flammable and/or toxic gases: H2, O2, NO, CO	Leakage of O2	Instrument and method training
	Leakage of O2	Security Data Sheet
	Leakage of O2	Exhaust hood
	Leakage of O2	The set up
	Leakage of O2	Leakage Tests
	Leakage of H2	Instrument and method training
	Leakage of H2	Security Data Sheet
	Leakage of H2	Gas Detector
	Leakage of H2	Exhaust hood
	Leakage of H2	The set up
	Leakage of H2	Leakage Tests
	Leakage of NO	Instrument and method training
	Leakage of NO	Security Data Sheet
	Leakage of NO	Gas Detector
	Leakage of NO	Exhaust hood
	Leakage of NO	The set up
	Leakage of NO	Safety Equipment
	Leakage of NO	Leakage Tests
	Leakage of CO	Instrument and method training
	Leakage of CO	Security Data Sheet
	Leakage of CO	Gas Detector
	Leakage of CO	Exhaust hood
	Leakage of CO	The set up
	Leakage of CO	Safety Equipment
	Leakage of CO	Leakage Tests
Use of nontoxic gases and/or inert gases: CH4, Ar	Leakage of CH4	Instrument and method training
	Leakage of CH4	Security Data Sheet
	Leakage of CH4	Exhaust hood
	Leakage of CH4	The set up
	Leakage of CH4	Safety Equipment
	Leakage of CH4	Leakage Tests
	Leakage of Argon	Security Data Sheet
	Leakage of Argon	Exhaust hood

Norges teknisk-naturvitenskapelige universitet (NTNU)

Unntatt offentlighet jf. Offentlighetsloven § 14

Print date:

27.09.2021

Printed by:

Vilde Vinnes Jacobsen

Page:

13/34

Use of nontoxic gases and/or inert gases: CH4, Ar	Leakage of Argon	The set up
	Leakage of Argon	Safe waste handeling
	Leakage of Argon	Leakage Tests
Heating the reactor furnace	Burning injuries	Instrument and method training
	Burning injuries	The set up
	Burning injuries	Safety Equipment
	Burning injuries	Thermal protective wear
Electricity failure	Fire	Instrument and method training
	Fire	The set up
	Fire	Safety Equipment
N2-physisorption, TPR	Handling liquid nitrogen	Instrument and method training
	Handling liquid nitrogen	Security Data Sheet
	Handling liquid nitrogen	Safety Equipment

Existing relevant measures with descriptions:

Instrument and method training

Understand the procedure of techniques and equipment in the training.
Ask about any possible troubles and risks and doubts about the procedure.
Read and familiarize with the procedure before experiments.

Security Data Sheet

Read and understand the precautions and actions that are required for the risks of each chemical.

Gas Detector

Check if the gas detector works before each experiment. Understand the different alarms associated to each gas and how to act for each one.

Exhaust hood

Check that the local exhaust hood works for each experiment.
Acts as an local exhaust system enabling us to handle toxic, hazardous chemicals with minimal exposure.

The set up

Learn and understand the risks associated with the installation of the set up, the gasses used, the operation temperature and how to act in case of emergency.

Safety Equipment

Safety goggles mandatory in all laboratories
Lab coat
Gloves (read sds in order to choose the correct gloves)
Gas mask(read sds in order to choose the correct filters)
Filter mask (read sds in order to choose the correct type)

Safe waste handeling

All wastes must go to their respective handling sites.

Leakage Tests

Verify the isolation of the installation before running experiments.

Thermal protective wear

Gloves and apron

Risk analysis with evaluation of likelihood and consequence

This part of the report presents detailed documentation of hazards, incidents and causes which have been evaluated. A summary of hazards and associated incidents is listed at the beginning.

The following hazards and incidents has been evaluated in this risk assessment:

- **Handling chemicals: Pd(NO3)2, Rh(NO3)3*2H2O, Ce(NO3)3*6H2O, ZrO(NO3)2*xH2O, Al2O3, citric acid, ammonium hydroxide**
    - Spilling palladium (II) nitrate solution
    - Spilling rhodium(III) nitrate dihydrate
    - Spilling cerium (III) nitrate hexahydrate
    - Spilling zirconium (IV) oxynitrate hydrate
    - Spilling citric acid
    - Spilling ammonium hydroxide
    - Spilling 2-propanol
- **Calcination in high temperature furnace**
    - Burning injuries
- **Use of flammable and/or toxic gases: H2, O2, NO, CO**
    - Leakage of O2
    - Leakage of H2
    - Leakage of NO
    - Leakage of CO
- **Use of nontoxic gases and/or inert gases: CH4, Ar**
    - Leakage of CH4
    - Leakage of Argon
- **Heating the reactor furnace**
    - Burning injuries
- **Electricity failure**
    - Fire
- **N2-physisorption, TPR**
    - Handling liquid nitrogen

Detailed view of hazards and incidents:

Hazard: Handling chemicals: Pd(NO3)2, Rh(NO3)3*2H2O, Ce(NO3)3*6H2O, ZrO(NO3)2*xH2O, Al2O3, citric acid, ammonium hydroxide

Incident: Spilling palladium (II) nitrate solution

- -

Likelihood of the incident (common to all consequence areas):   **Less likely (2)**

  Kommentar:

  P260 Do not breathe dust/fume/gas/mist/vapors/spray
  P264 Wash face, hands and any exposed skin thoroughly after handling
  P280 Wear protective gloves/protective clothing/eye protection/face protection
  p271 Use only outdoors or in a well-ventilated area
  P234 Keep only in original container
  P284 Wear respiratory protection

  P304 + P340 + P310 IF INHALED: Remove victim to fresh air and keep at rest in a position comfortable for breathing
  Immediately call a POISON CENTER or doctor/physician

  P303 + P361 + P353 IF ON SKIN (or hair): Take off immediately all contaminated clothing. Rinse skin with water/shower

  P363 Wash contaminated clothing before reuse

  P305 + P351 + P338 + P310 IF IN EYES: Rinse cautiously with water for several minutes. Remove contact lenses, if present and easy to do. Continue rinsing. Immediately call a POISON CENTER or doctor/physician

   P301 + P330 + P331 IF SWALLOWED: Rinse mouth. DO NOT induce vomiting

Consequence area: Helse   *Risk:*

  Assessed consequence: **Large (3)**

           Comment: H314 Causes severe skin burns and eye damage
                       H333 Harmful if inhaled

Consequence area: Materielle verdier   *Risk:*

  Assessed consequence: **Large (3)**

           Comment: H290 May be corrosive to metals.

Norges teknisk-naturvitenskapelige universitet (NTNU)   **Print date:**   **Printed by:**   **Page:**

Unntatt offentlighet jf. Offentlighetsloven § 14   27.09.2021   Vilde Vinnes Jacobsen   16/34

Incident: Spilling rhodium(III) nitrate dihydrate

Likelihood of the incident (common to all consequence areas):   **Less likely (2)**

> *Kommentar:*
>
> P220: Keep/Store away from clothing/.../combustible materials.
> P280: Wear protective gloves/protective clothing/eye protection/face protection.
> P309: IF exposed or if you feel unwell:
> P310: Immediately call a POISON CENTER or doctor/physician.
> P305 + P351 + P338: IF IN EYES: Rinse cautiously with water for several minutes. Remove contact lenses, if present and easy to do. Continue rinsing.

Consequence area: Helse

Risk:

Assessed consequence: **Large (3)**

> *Comment:* H314 Causes severe skin burns and eye damage.

Consequence area: Ytre miljø

Risk:

Assessed consequence: **Large (3)**

> *Comment:* H272 May intensify fires; oxidiser
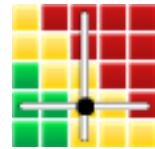
Incident: Spilling cerium (III) nitrate hexahydrate

Likelihood of the incident (common to all consequence areas):   **Less likely (2)**

Kommentar:

P210 Keep away from heat, hot surfaces,
sparks, open flames and other ignition
sources. No smoking.
P273 Avoid release to the environment.
P280 Wear protective gloves/ eye protection/
face protection.
P305 + P351 + P338 IF IN EYES: Rinse cautiously with water
for several minutes. Remove contact
lenses, if present and easy to do.
Continue rinsing.
P308 + P313 IF exposed or concerned: Get medical
advice/ attention.

Consequence area: Helse   *Risk:*

Assessed consequence: **Large (3)**

Comment:

H318 Causes serious eye damage

Consequence area: Ytre miljø   *Risk:*

Assessed consequence: **Very large (4)**

Comment: H272 May intensify fire; oxidizer.
H410 Very toxic to aquatic life with long lasting
effects.

**Norges teknisk-naturvitenskapelige
universitet (NTNU)**

Unntatt offentlighet jf. Offentlighetsloven § 14

Print date:

27.09.2021

Printed by:

Vilde Vinnes Jacobsen

Page:

18/34

Incident: Spilling zirconium (IV) oxynitrate hydrate

Likelihood of the incident (common to all consequence areas):   **Less likely (2)**

Kommentar:

P210 Keep away from heat, hot surfaces, sparks, open flames and
other ignition sources. No smoking.
P220 Keep away from clothing and other combustible materials.
P260 Do not breathe dusts or mists.
P264 Wash skin thoroughly after handling.
P280 Wear protective gloves/ protective clothing/ eye protection/ face
protection.
P301 + P330 + P331 IF SWALLOWED: Rinse mouth. Do NOT induce vomiting.
P303 + P361 + P353 IF ON SKIN (or hair): Take off immediately all contaminated
clothing. Rinse skin with water.
P304 + P340 + P310 IF INHALED: Remove person to fresh air and keep comfortable
for breathing. Immediately call a POISON CENTER/ doctor.
P305 + P351 + P338 +
P310
IF IN EYES: Rinse cautiously with water for several minutes.
Remove contact lenses, if present and easy to do. Continue
rinsing. Immediately call a POISON CENTER/ doctor.
P363 Wash contaminated clothing before reuse.
P370 + P378 In case of fire: Use dry sand, dry chemical or alcohol-resistant
foam to extinguish.
P405 Store locked up.
P501 Dispose of contents/ container to an approved waste disposal
plant.

Consequence area: Helse   *Risk:*

Assessed consequence: **Large (3)**

Comment: H314 Causes severe skin burns and eye damage

Consequence area: Ytre miljø   *Risk:*

Assessed consequence: **Large (3)**

Comment: H272 May intensify fire; oxidizer

Norges teknisk-naturvitenskapelige universitet (NTNU)   **Print date:**   **Printed by:**   **Page:**

Unntatt offentlighet jf. Offentlighetsloven § 14   27.09.2021   Vilde Vinnes Jacobsen   19/34

Incident: Spilling citric acid

Likelihood of the incident (common to all consequence areas):   **Less likely (2)**

Kommentar:

P337+313 If eye irritation persists: Get medical advice/attention.

P280 Wear protective gloves/protective clothing/eye protection/face protection.
P264 Wash contaminated skin thoroughly after handling.

P305+351+338 IF IN EYES: Rinse cautiously with water for several minutes. Remove contact
lenses, if present and easy to do. Continue rinsing

Consequence area: Helse   *Risk:*

Assessed consequence: **Medium (2)**

Comment: H319 Causes serious eye irritation

Incident: Spilling ammonium hydroxide

Likelihood of the incident (common to all consequence areas):   **Less likely (2)**

Kommentar:

P264 Wash hands thoroughly after handling.
P273 Avoid release to the environment.
P280 Wear protective gloves/protective clothing/eye protection/face protection.Revised on 04/26/2016 Page 2
of 6
P302+P352 IF ON SKIN: Wash with plenty of water.
P305+P351+P338 IF IN EYES: Rinse cautiously with water for several minutes. Remove contact
lenses, if present and easy to do. Continue rinsing.
P310 Immediately call a POISON CENTER/doctor/physician.
P332+P313 If skin irritation occurs: Get medical advice/attention.
P362+P364 Take off contaminated clothing and wash it before reuse.
P391 Collect spillage.
P501 Dispose of contents/container in accordance with local regulations.

Consequence area: Helse   *Risk:*

Assessed consequence: **Large (3)**

Comment: H315 Causes skin irritation.
H318 Causes serious eye damage

**Norges teknisk-naturvitenskapelige
universitet (NTNU)**   **Print date:**   **Printed by:**   **Page:**

Unntatt offentlighet jf. Offentlighetsloven § 14   27.09.2021   Vilde Vinnes Jacobsen   20/34

Consequence area: Ytre miljø

Risk:

Assessed consequence: **Large (3)**

Comment: H400 Very toxic to aquatic life.

Incident: Spilling 2-propanol

- -

Likelihood of the incident (common to all consequence areas):   **Less likely (2)**

Kommentar:

P210 Keep away from heat/sparks/open flames/hot surfaces. - No smoking.

P260 Do not breathe vapours.

P280 Wear protective gloves.

P305+351+338 IF IN EYES: Rinse cautiously with water for several minutes. Remove contact lenses, if present and easy to do. Continue rinsing.

P370 In case of fire: Use alcohol resistant foam or dry powder for extinction.

P501D Empty containers may contain residual product and vapours. Do not cut or weld on or near empty containers. Disposal should only be by means of a licensed waste disposal contractor.

P264 Wash skin thoroughly after handling.

P303+361+353 IF ON SKIN (or hair): Remove/Take off immediately all contaminated clothing. Rinse skin with water/shower.

P304+340 IF INHALED: Remove victim to fresh air and keep at rest in a position comfortable for breathing.

P403+233+235 Store in a well-ventilated place, in original container. Keep container tightly closed, Keep cool.

Consequence area: Helse

Risk:

Assessed consequence: **Medium (2)**

Comment: H319 Causes serious eye irritation
H336 May cause drowsiness or dizziness.

Consequence area: Ytre miljø

Risk:

Assessed consequence: **Large (3)**

Comment: H225 Highly flammable liquid and vapour

Consequence area: Materielle verdier

Risk:

Assessed consequence: **Large (3)**

Comment: H225 Highly flammable liquid and vapour

Hazard: Calcination in high temperature furnace

Incident: Burning injuries

- -

Likelihood of the incident (common to all consequence areas):   **Unlikely (1)**

Kommentar:

Use protective equipment.
Wait for cool down to remove the sample.
Use thermal gloves

Consequence area: Helse   *Risk:*

Assessed consequence: **Small (1)**

Comment: [Ingen registreringer]

Norges teknisk-naturvitenskapelige universitet (NTNU)

Unntatt offentlighet jf. Offentlighetsloven § 14

Print date:
27.09.2021

Printed by:
Vilde Vinnes Jacobsen

Page:
23/34

Hazard: Use of flammable and/or toxic gases: H2, O2, NO, CO

Incident: Leakage of O2

Likelihood of the incident (common to all consequence areas):　　**Less likely (2)**

Kommentar:

Leakage test before experiments, work under local exhaust.
The oxygen is obtained pure from the house distribution system
P220: Keep away from clothing and other combustible materials.
P244: Keep valves and fittings free from oil and grease.
P370+P376: In case of fire: Stop leak if safe to do so.
P403: Store in a well-ventilated place.

Consequence area: Helse　　　　　　　　　　　　　　　　　　　　*Risk:*

Assessed consequence: **Large (3)**

　　　　Comment: H270: May cause or intensify fire; oxidizer.
　　　　　　　　　H280: Contains gas under pressure; may explode if heated.

Consequence area: Ytre miljø　　　　　　　　　　　　　　　　　*Risk:*

Assessed consequence: **Large (3)**

　　　　Comment: Can affect the people around you too
　　　　　　　　　H270: May cause or intensify fire; oxidizer.
　　　　　　　　　H280: Contains gas under pressure; may explode if heated.

Consequence area: Materielle verdier　　　　　　　　　　　　　*Risk:*

Assessed consequence: **Large (3)**

　　　　Comment: H270: May cause or intensify fire; oxidizer.
　　　　　　　　　H280: Contains gas under pressure; may explode if heated.

Norges teknisk-naturvitenskapelige universitet (NTNU)　　**Print date:**　　**Printed by:**　　　　　　　　**Page:**

Unntatt offentlighet jf. Offentlighetsloven § 14　　27.09.2021　　Vilde Vinnes Jacobsen　　　24/34

Incident: Leakage of H2

- -

Likelihood of the incident (common to all consequence areas):   **Less likely (2)**

> *Kommentar:*
>
> Use a fume hood and check for leakage
> The hydrogen is obtained pure from the house distribution system
> P210: Keep away from heat, hot surfaces, sparks, open flames and other ignition sources. No smoking.
> P377: Leaking gas fire: Do not extinguish, unless leak can be stopped safely.
> P381: eliminate all ignition sources.
> P410 + P403: Protect from sunlight. Store in a well-ventilated place

Consequence area: Helse   *Risk:*

> *Assessed consequence:* **Very large (4)**
>
> > *Comment:* H221: Extremely flammable gas.
> > H280: Contains gas under pressure; may explode if heated.
> > H380: May displace oxygen and cause rapid suffocation.
> > Burns with invisible flame.
> > May form explosive mixtures with air.

Consequence area: Ytre miljø   *Risk:*

> *Assessed consequence:* **Large (3)**
>
> > *Comment:* Can affect the people around you too
> > H221: Extremely flammable gas.
> > H280: Contains gas under pressure; may explode if heated.
> > H380: May displace oxygen and cause rapid suffocation.
> > Burns with invisible flame.
> > May form explosive mixtures with air.

Consequence area: Materielle verdier   *Risk:*

> *Assessed consequence:* **Large (3)**
>
> > *Comment:* H221: Extremely flammable gas.
> > H280: Contains gas under pressure; may explode if heated.
> > H380: May displace oxygen and cause rapid suffocation.
> > Burns with invisible flame.
> > May form explosive mixtures with air.

Incident: Leakage of NO

Likelihood of the incident (common to all consequence areas): **Less likely (2)**

> *Kommentar:*
>
> Use fume hood and leak test before experiement
> P202 - Do not handle until all safety precautions have been read and understood.
> P220 - Keep/Store away from clothing, combustible materials
> P244 - Keep reduction valves/valves and fittings free from oil and grease
> P260 - Do not breathe gas
> P262 - Do not get in eyes, on skin, or on clothing.
> P271+P403 - Use and store only outdoors or in a well-ventilated place.
> P280+P284 - Wear protective gloves, protective clothing, eye protection, respiratory protection, and/or face protection.
> P303+P361+P353 - IF ON SKIN OR (HAIR): Take off immediately all contaminated clothing. Rinse skin with water/shower.
> P304, P340, P310 - IF INHALED: Remove person to fresh air and keep comfortable for breathing. Immediately call a poison center or doctor/physician.
> P332+P313 - IF SKIN IRRITATION OCCURS: Get medical advice/attention.
> P-305-351-338-313 - IF IN EYES: Rinse cautiously with water for several minutes. Remove contact lenses, if present and easy to do. Continue rinsing. Get medical advice/attention.
> P370+P376 - In case of fire: Stop leak if safe to do so
> P405 - Store locked up.
> P501 - Dispose of contents/container in accordance with local/regional/national/international regulations. Contact supplier for any special requirements.
> CGA-PG05 - Use a back flow preventive device in the piping.
> CGA-PG20+CGA-PG10 - Use only with equipment of compatible materials of construction and rated for cylinder pressure.
> CGA-PG22 - Use only with equipment cleaned for oxygen service.
> CGA-PG12 - Do not open valve until connected to equipment prepared for use.
> CGA-PG18 - When returning cylinder, install leak tight valve outlet cap or plug.
> CGA-PG21 - Open valve slowly.
> CGA-PG06 - Close valve after each use and when empty.
> CGA-PG02 - Protect from sunlight when ambient temperature exceeds 52°C (125°F).
> NO is a diluted gas (2 vol% in Ar)

Consequence area: Helse   *Risk:*

Assessed consequence: **Very large (4)**

> Comment: H270 - MAY CAUSE OR INTENSIFY FIRE; OXIDIZER
> H280 - CONTAINS GAS UNDER PRESSURE; MAY EXPLODE IF HEATED
> H314 - CAUSES SEVERE SKIN BURNS AND EYE DAMAGE
> H330 - FATAL IF INHALED
> CGA-HG22 - CORROSIVE TO THE RESPIRATORY TRACT
> CGA-HG11 - SYMPTOMS MAY BE DELAYED

Consequence area: Ytre miljø   *Risk:*

Assessed consequence: **Large (3)**

> Comment: Can affect the people around you too
> H270 - MAY CAUSE OR INTENSIFY FIRE; OXIDIZER
> H280 - CONTAINS GAS UNDER PRESSURE; MAY EXPLODE IF HEATED

Consequence area: Materielle verdier

Risk:

Assessed consequence: **Large (3)**

Comment: H270 - MAY CAUSE OR INTENSIFY FIRE; OXIDIZER
H280 - CONTAINS GAS UNDER PRESSURE; MAY EXPLODE IF HEATED

Incident: Leakage of CO

Likelihood of the incident (common to all consequence areas): **Less likely (2)**

Kommentar:

Use fume hood and leak test before experiments.
P202: Do not handle until all safety precautions have been read and understood.
P210: Keep away from heat, hot surfaces, sparks, open flames and other ignition sources. No smoking.
P260: Do not breathe gas/vapours.
P304+P340+P315: IF INHALED: Remove person to fresh air and keep comfortable for breathing. Get immediate medical advice/attention.
P308+P313: IF exposed or concerned: Get medical advice/attention.
P377: Leaking gas fire: Do not extinguish, unless leak can be stopped safely.
P381: Eliminate all ignition sources if safe to do so.
P403: Store in a well-ventilated place.
P405: Store locked up.
CO is a diluted gas (10 vol% in Ar)

Consequence area: Helse

Risk:

Assessed consequence: **Very large (4)**

Comment: H220: Extremely flammable gas.
H280: Contains gas under pressure; may explode if heated.
H331: Toxic if inhaled.
H360D: May damage the unborn child.
H372: Causes damage to organs through prolonged or repeated exposure

Consequence area: Ytre miljø

Risk:

Assessed consequence: **Very large (4)**

Comment: Can affect the people around you too
H220: Extremely flammable gas.
H280: Contains gas under pressure; may explode if heated.

Consequence area: Materielle verdier

Risk:

Assessed consequence: **Large (3)**

Comment: H220: Extremely flammable gas.
H280: Contains gas under pressure; may explode if heated.

Hazard: Use of nontoxic gases and/or inert gases: CH4, Ar

Incident: Leakage of CH4
- -

Likelihood of the incident (common to all consequence areas):   **Less likely (2)**

      Kommentar:

Work under fume hood and perform leak testing.
P202 - Do not handle until all safety precautions have been read and understood
P210 - Keep away from Heat, Open flames, Sparks, Hot surfaces. - No smoking
P271+P403 - Use and store only outdoors or in a well-ventilated place
P377 - Leaking gas fire: Do not extinguish, unless leak can be stopped safely
P381 - Eliminate all ignition sources if safe to do so
CGA-PG05 - Use a back flow preventive device in the piping
CGA-PG10 - Use only with equipment rated for cylinder pressure
CGA-PG06 - Close valve after each use and when empty
CGA-PG11 - Never put cylinders into unventilated areas of passenger vehicles
CGA-PG02 - Protect from sunlight when ambient temperature exceeds 52°C (125°F)
Methane is a diluted gas (2 vol% in Ar)

Consequence area: Helse   *Risk:*

    Assessed consequence: **Large (3)**

      Comment:
        H220 - EXTREMELY FLAMMABLE GAS
        H280 - CONTAINS GAS UNDER PRESSURE; MAY EXPLODE IF HEATED
        OSHA-H01 - MAY DISPLACE OXYGEN AND CAUSE RAPID SUFFOCATION
        CGA-HG04 - MAY FORM EXPLOSIVE MIXTURES WITH AIR

Consequence area: Ytre miljø   *Risk:*

    Assessed consequence: **Large (3)**

    Comment: H220 - EXTREMELY FLAMMABLE GAS
        H280 - CONTAINS GAS UNDER PRESSURE; MAY EXPLODE IF HEATED
        OSHA-H01 - MAY DISPLACE OXYGEN AND CAUSE RAPID SUFFOCATION
        CGA-HG04 - MAY FORM EXPLOSIVE MIXTURES WITH AIR

Consequence area: Materielle verdier   *Risk:*

    Assessed consequence: **Large (3)**

    Comment: H220 - EXTREMELY FLAMMABLE GAS
        H280 - CONTAINS GAS UNDER PRESSURE; MAY EXPLODE IF HEATED
        OSHA-H01 - MAY DISPLACE OXYGEN AND CAUSE RAPID SUFFOCATION
        CGA-HG04 - MAY FORM EXPLOSIVE MIXTURES WITH AIR

Incident: Leakage of Argon

Likelihood of the incident (common to all consequence areas):   **Unlikely (1)**

Kommentar:

The Argon is obtained as pure gas from the house distribution system and it is not stored in the lab.

Consequence area: Helse   _Risk:_

Assessed consequence: **Large (3)**

Comment: Contains gas under pressure; may explode if heated.
May displace oxygen and cause rapid suffocation.

Consequence area: Ytre miljø   _Risk:_

Assessed consequence: **Large (3)**

Comment: May affect the people around you
Contains gas under pressure; may explode if heated.
May displace oxygen and cause rapid suffocation.

Consequence area: Materielle verdier   _Risk:_

Assessed consequence: **Large (3)**

Comment: Contains gas under pressure; may explode if heated.

Hazard: Heating the reactor furnace

Incident: Burning injuries

- -

Likelihood of the incident (common to all consequence areas):   **Unlikely (1)**

        Kommentar:

        Use protective equipment.
        Wait for cool down to remove sample/reactor
        Use thermal gloves

Consequence area: Helse   *Risk:*

      Assessed consequence: **Small (1)**

              Comment: Small burning injuries by touching the reactor.

Norges teknisk-naturvitenskapelige universitet (NTNU)

Unntatt offentlighet jf. Offentlighetsloven § 14   27.09.2021

Print date: **Printed by:**   Vilde Vinnes Jacobsen

Page:

30/34

Hazard: Electricity failure

Incident: Fire
- -

Likelihood of the incident (common to all consequence areas): **Unlikely (1)**

       Kommentar:

Earthing, covers, barriers, safe separation:
No live parts are directly accessible or can be touched without removing enclosures or insulation. All conductive parts that can be directly accessed and touched, such as instrument housings, gas pipes, reactor support, etc. are earthed.
Grounding is achieved either directly via the earth connection of the power cables (instrument housings) or indirectly like e.g. the stainless steel lines via the earthing of the mass flow controllers.
Working when switched off:
The equipment is switched off when the multi sockets to which electrical parts are connected are off.
Repairs on equipment connected to voltage are forbidden.

Consequence area: Helse   *Risk:*
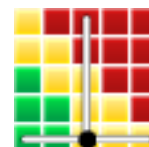
    Assessed consequence: **Large (3)**

        Comment: [Ingen registreringer]

Consequence area: Ytre miljø   *Risk:*
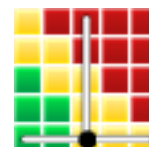
    Assessed consequence: **Large (3)**

        Comment: [Ingen registreringer]

Consequence area: Materielle verdier   *Risk:*

    Assessed consequence: **Large (3)**

        Comment: [Ingen registreringer]

Hazard: N2-physisorption, TPR

Incident: Handling liquid nitrogen

- -

Likelihood of the incident (common to all consequence areas):   **Less likely (2)**

> *Kommentar:*
> Use safety equipment

Consequence area: Helse   *Risk:*

> *Assessed consequence:* **Large (3)**

> > *Comment:* Liquid nitrogen at 77K will burn when contact with skin.

Norges teknisk-naturvitenskapelige universitet (NTNU)

	Print date:	**Printed by:**	**Page:**
Unntatt offentlighet jf. Offentlighetsloven § 14	27.09.2021	Vilde Vinnes Jacobsen	32/34

Overview of risk mitiating measures which have been decided:

Below is an overview of risk mitigating measures, which are intended to contribute towards minimizing the likelihood and/or consequence of incidents:

Overview of risk mitigating measures which have been decided, with description:

Detailed view of assessed risk for each hazard/incident before and after mitigating measures

Norges teknisk-naturvitenskapelige universitet (NTNU)

Unntatt offentlighet jf. Offentlighetsloven § 14

Print date:

27.09.2021

Printed by:

Vilde Vinnes Jacobsen

Page:

34/34